Hard Spheres, Soap Bubbles, and Hydrogels in Research and Education

---

Ali Irannezhad

School of Physics
Trinity College Dublin

A thesis submitted for the degree of

Doctor of Philosophy
June 30, 2023

Declaration

I declare that this thesis has not been submitted as an exercise for a degree at this or any other university and it is entirely my own work and the work has been carried out jointly, have addressed in the text wherever included.

I agree to deposit this thesis in the University's open access institutional repository or allow the Library to do so on my behalf, subject to Irish Copyright Legislation and Trinity College Library conditions of use and acknowledgement.

I consent to the examiner retaining a copy of the thesis beyond the examining period, should they so wish (EU GDPR May 2018).

Ali Irannezhad...

Summary

This thesis concerns various experiments using hard spheres, soap bubbles, hydrogel spheres, and soap films in which we will show these are suitable candidates for research and can be easily performed in universities, classrooms, or even at home to express physical concepts such as instability, symmetry breaking, buckling, dense packing, and failure.

Initially, we briefly present examples of using hard spheres and soap film that are used to demonstrate science. For example, we describe how soap films can be used to help with minimization problems such as *the Motorway Problem*.

We then discuss the buckling behavior of a linear chain of hard spheres confined in a transverse harmonic potential that displays instability and buckling under compression and tilt. We will discuss different arrangements of such chains under low and high compressions and under tilt. At low compression, a modulated zig-zag arrangement is observed which is followed by a localized buckling at higher compression and will end with a doublet structure at higher compressions. In addition, we will demonstrate there is a critical tilt for the buckling of the system.

Friction plays a critical role in our buckling experiments using hard spheres. To eliminate friction, we will discuss an alternative for buckling experiments using soap bubbles. So, a linear chain of soap bubbles is investigated under compression. Due to the deformability of soap bubbles, we show the onset of buckling occurs at a critical value of compression. Also, our findings are in good agreement with the simulation. In addition, we present how the transverse bubble width changes as a function of compression.

Packing experiments using hydrogel spheres will be introduced. First, we will demonstrate how a line of hydrogel spheres lying at the bottom of a cylindrical tube can show a zigzag pattern as observed using a chain of hard spheres and soap bubbles. Then I will show various types of packing problems using hydrogel spheres. The experiments are easy to set up and thus suitable for use in the classroom or in the undergraduate teaching laboratory.

As bubbles are a relatively easy system to experiment with, we will introduce another field of research where soap films/bubbles can be used to obtain experimental data related to studies of failure/mortality. We introduce controlled experiments using individual soap films confined in the middle of Perspex tubes as a simple physical system to model the failure and mortality. Our examination of soap film lifetime statistics has yielded valuable insights and showed that individual soap films displayed a common pattern of mortality/failure called the bath-tub curve. Our findings show a linear relationship between film lifetime and tube length and introduce a relationship between defects in the system and soap film lifetime.

Finally, we conclude our results and introduce suggestions for further research. First, we suggest another buckling experiment using slanted stoppers instead of flat stoppers to investigate the effect of changing the boundary conditions in buckled structures. We show that instead of using flat stoppers if one uses slanted stoppers that leads to a double-peak structure, and rather than a localized buckling at high compression, a modulated zigzag can be observed.

In addition, we suggest further exploration of soap film lifetime to investigate the effect of external factors on the ageing and failure of soap films that can be used as a simple system to see how mortality curves look like for people that always lived under poor conditions.

Acknowledgements

It is with great pleasure that I express my sincere appreciation to all those who have contributed to my journey as a Ph.D. student. I owe a deep debt of gratitude to my supervisor, Professor Stefan Hutzler for his unwavering support, guidance, and patience throughout the last four and a half years. His expertise and constructive criticism have been invaluable in shaping my research project, and I could not have completed this work without his guidance. He has always been more than a supervisor to me; he has been a source of inspiration, and precision, and a role model for academic excellence.

I would also like to express my sincere gratitude to Prof. Emeritus Denis Weaire for his valuable ideas to my research project.

I am also grateful to Professors Peter Richmond and Bertrand M. Roehner (Sorbonne University, France) for their ideas and suggestions, which have enriched my research project and provided me with valuable insights and perspectives.

I am also deeply appreciative of Professor Dr. Adil Mughal (Aberystwyth University, Wales) for his beautiful simulations, which have helped to support our experiments. His expertise in this area has been invaluable, and I am grateful for his contribution to my research project.

I would also like to extend my gratitude to my former office and our group mates Ben, Fritz, Jens, and Steven for their great support during my Ph.D. studies. The office get much quieter when you left, then I decided to only stay in the lab downstairs.

Special thanks go to John and Jennifer for proofreading my thesis.

I would also like to thank Anthony, Aayush, Aisling, John, and Jennifer for their invaluable help in a number of experiments and graphs. Their contributions have been crucial in advancing my research project, and I am grateful for their assistance.

I am also deeply grateful to Ehsan, Adnan, Jennifer, and Arvind for their kindness, encouragement, and frequent chats during my Ph.D. journey. Their friendship and support have meant a great deal to me, and I am thankful for their presence in my life.

I would also like to acknowledge the unwavering support of my family. To my parents and sisters, thank you for your constant encouragement and belief in me, and for instilling in me the values of hard work, dedication, and perseverance.

A very special thank you goes to my wife, Fatima. Her support, encouragement, and love have been the driving force behind my Ph.D. journey. Her background in experimental physics has been invaluable in helping me to navigate some of the most challenging aspects of my research, and her unwavering belief in me has kept me going during the toughest times. Our little girl, who arrived during the Covid-19 pandemic, has brought immeasurable joy and happiness to our lives, and I am eager to welcome our upcoming baby in September 2023. I dedicate this thesis to my wife, my daughter, and our upcoming baby, with all my love and gratitude.

Finally, I would like to thank Trinity College Dublin Provost's Ph.D. Project Awards for supporting this work. Their generosity and commitment to academic excellence have been invaluable in enabling me to complete this research project, and I am grateful for their support.

List of Publications

1. D. Weaire et al., *A simple experimental system to illustrate the nonlinear properties of a linear chain under compression*, American Journal of Physics **88**, 347–352 (2020)
2. A. Bois et al., *Physical models of infant mortality: implications for defects in biological systems*, Journal of Biological Physics **46**, 371–394 (2020)
3. S. Hutzler et al., *Buckling of a linear chain of hard spheres in a harmonic confining potential: numerical and analytical results for low and high compression*, Physical Review E **102**, 022905 (2020)
4. P. Richmond et al., *Mortality: a physics perspective*, Physica A: Statistical Mechanics and its Applications **566**, 125660 (2021)
5. D. Weaire et al., "Physics in a small bedroom", in *Imagine math 8*, edited by M. Emmer and M. Abate (Springer, 2022), pp. 333–343
6. A. Irannezhad et al., *Buckling of a tilted line of confined hard spheres*, Philosophical Magazine **102**, 2506–2524 (2022)
7. A. Irannezhad et al., *Packing soft spheres: experimental demonstrations with hydrogels*, (Submitted) (2023)

Contents

List of Figures

List of Tables

Chapter 1

Introduction

> **”Everything should be made as simple as possible, but not simpler.**
>
> **— Albert Einstein**

1.1 Hands-on Physics Experiments in Research and Education

In 2019, with the spread of Covid-19, schools and universities faced new challenges [8].

At the inception of the pandemic, academic institutions such as schools and universities were forced to temporarily close their doors, resulting in the suspension of traditional pedagogical practices such as in-person classroom instruction and laboratory work. This closure also imposed restrictions on postgraduate students and researchers, effectively hindering access to critical scientific equipment and funding.

During this time, the global community's primary focus shifted to mitigating the spread of the virus and returning to a sense of normality.

In response to the closure, efforts were made to employ technology and transition to virtual learning environments. However, this shift was met with a number of challenges, as virtual instruction was deemed inferior in quality compared to traditional, in-person education, and hands-on laboratory experiments were either entirely eliminated or lacked the necessary resources to be effectively executed.

While the coronavirus sent universities and schools into prolonged hibernation, forced us to ask: how are we to adapt to our confinement? Available space for the study and research was restricted to a small bedroom. How were we to use it?

An obvious response has been to use remote teaching and learning, with online lectures and assignments. So far so good, and it will be very interesting to see what lasting effect this has on traditional research and teaching methods.

In Physics, we place a significant emphasis on hands-on experiments. This emphasis is also emphasized at Trinity College Dublin, where even theoretical physicists are required to engage in practical experimentation. Although simulated experiments on a screen can be beneficial, they cannot replace the value of real-life experimentation. In the context of remote confinement posed by the Covid-19 pandemic, it became challenging to carry out traditional work in research and education.

However, despite the successful control of the pandemic through universal vaccination and the removal of restrictions, there are still concerns about potential future challenges and epidemics, and how these might impact our ability to maintain the quality of research and education. The question of how to approach experiments and education in light of these challenges becomes imperative.

Furthermore, given that year 2022 has been named the *"International Year of Basic Sciences for Sustainable Development"* and to address this issue, we propose simple experiments using hard spheres, soap bubbles, hydrogels, and soap films in this thesis. These are suitable candidates for research and education from a flexible perspective, in a manner that allows for experimental activities to be carried out only with the help of available equipment without the need for expensive advanced equipment, and equipped laboratories. Also, they can be done in universities, classrooms, a small bedroom, or even in kitchens to express physical concepts such as instability, symmetry breaking, and statistical physics, regardless of unpredictable events and whether in normal or epidemic conditions.

Also, different methods can be used to demonstrate science. For example, physics and natural phenomena can be taught to students through scientific puzzles and stimulate their curiosity [9]. But our intention here is to introduce simple experiments that can be done in a classroom or even in a small bedroom [5] using the inexpensive and available facilities that can be found in the home. For instance, experiments using a linear chain of soap bubbles (will be explained in Chapter 3) is an example of such simple experiments that can be done at home, and we have recently published in the American Journal of Physics: it made it onto the cover of the May 2020 issue [1] (see Fig. 1.1).

In Sections 1.2 and 1.3, we will briefly describe some examples of the use of hard/soft spheres and soap bubbles/films to demonstrate science, before detailing our new contributions in the next Chapters.

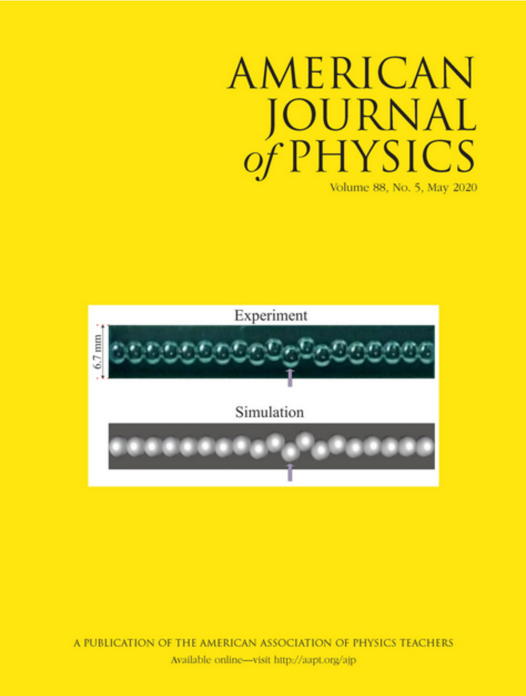

AMERICAN
JOURNAL
of PHYSICS
Volume 88, No. 5, May 2020

A PUBLICATION OF THE AMERICAN ASSOCIATION OF PHYSICS TEACHERS
Available online—visit http://aapt.org/aip

Fig 1.1: A photograph of a buckled linear chain of soap bubbles, together with the corresponding computer simulation, that we have recently published, features on the cover of the American Journal of Physics, Volume 88, Number 5, May 2022. Reprinted with the permission of AIP Publishing [3]. The article describes a simple experimental set-up for the exploration of the nonlinear properties of a chain of spheres under compression which will be discussed in Chapter 3.

1.2 Experiments with Hard Spheres

The study of hard spheres is an important topic in the field of condensed matter physics. Hands-on experiments can be used to investigate the properties of hard spheres, such as their phase behavior and crystallization. For example, a classic experiment involves the preparation of a colloidal crystal using hard spheres and visualization of the crystal structure using optical microscopy [10]. This experiment provides insight into the nature of packing and symmetry in a system of hard spheres.

One can obtain a suitable number of ball bearings or similar solid spheres for the experiment. It is noteworthy to consider the parity of the number of spheres as it affects the symmetry properties of the system. The spheres of diameter D are then placed inside a tube of diameter d ($\frac{d}{D} \simeq 3$) that is fitted with stoppers at both ends, and the tube is laid horizontally. To bring the system into equilibrium, a slight agitation is induced, and the immersion of the spheres in oil can aid this process.

Upon sufficient compression, as achieved by adjusting the stoppers, the chain of hard spheres buckles in a zigzag pattern, as illustrated in Fig. 1.2. This buckling mechanism is worthy of investigation, as it may be related to the concept of Euler buckling. However, it is apparent from Fig. 1.2 that the buckling is not uniform, and alternative sphere arrangements can be observed for higher levels of compression. The localized buckling phenomenon raises the question of "kinks" and "solitons" observed in various nonlinear systems, thereby evoking thoughts about non-linearity in general.

The great John von Neumann had previously noted that the advent of computing technology would extend the applicability of mathematics beyond the realm of linear problems. In light of this, it may be advantageous to replicate the results of an experiment through computer simulation.

There are numerous advanced laboratory systems that are comparable to

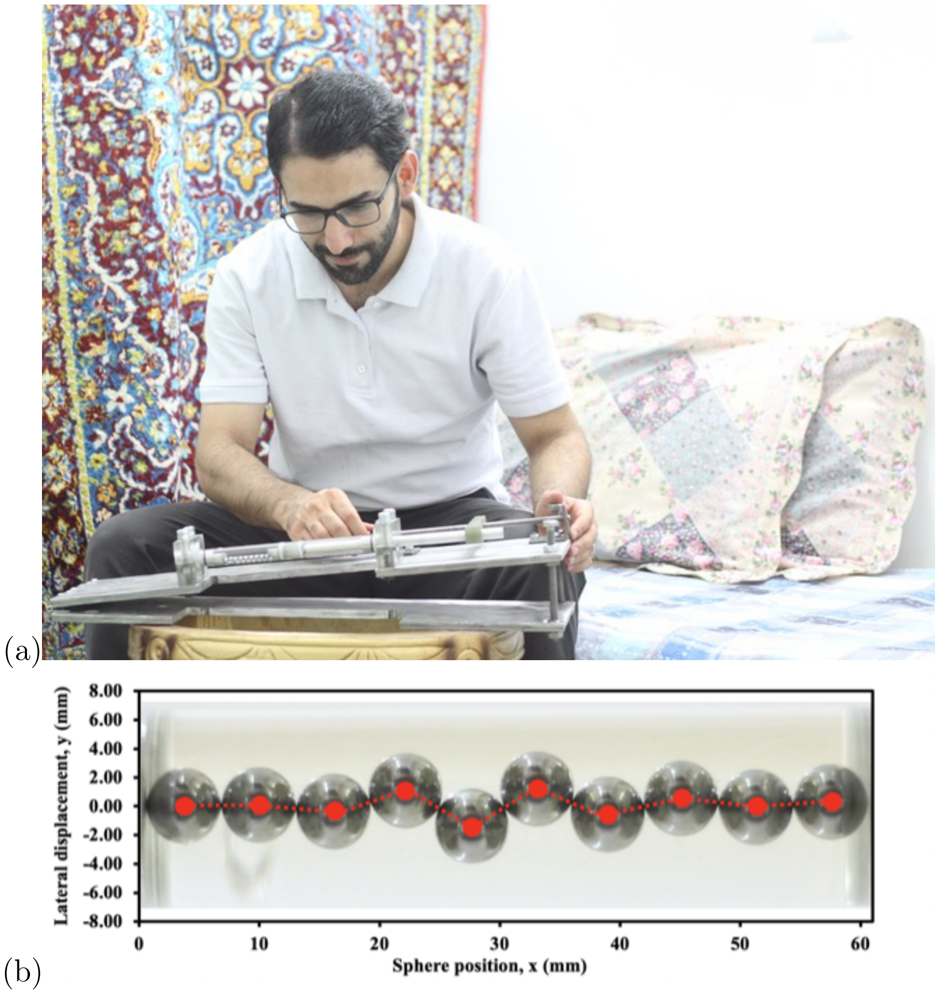

Fig 1.2: I am performing experiments in my bedroom in Tehran, Iran, during a Covid lock-down. My apparatus consists of a cylinder containing metal spheres. Pushing in the sides of the cylinder induces buckling of the initially linear chain. The effect becomes more and more localised as this compression is increased. In a variation of the experiment we study the position of the localisation peak as the cylinder is tilted, in order to determine the so-called Peierls-Nabarro potential [11]. This potential, originating in the theory of crystal dislocations, can tell us how the localized buckling moves when we tilt the apparatus. (This is difficult to investigate with hard spheres, easier with bubbles.)

the simple set-up previously described, but they often necessitate the utilization of costly apparatus, such as that utilized in ion trapping, which this experiment aimed to avoid. There exist numerous possibilities for variation of the experiment that can be achieved without excessive complexity, for example, using soft bubbles instead of hard spheres.

Another hard-sphere experiment is associated with Isaac Newton, some of whose greatest achievements were made in seclusion: "*All this was in the two plague years of 1665-1666. For in those days I was in the prime of my age for invention & minded Mathematicks & Philosophy more then than at any time since.*" (quoted in [12]).

Newton's Cradle (Fig. 1.3), which appears to have been discussed first in 1662 by the mathematicians/natural philosophers John Wallis, Christiaan Huygens and Christopher Wren (the latter being also the architect of St. Paul's Cathedral in London) is a popular executive desk ornament, illustrating the principles of classical Newtonian mechanics. It is not hard to understand its obvious properties, but physicists always like to look more closely. John Hinch (one of many leading mathematicians who have followed in Newton's footsteps at Trinity College Cambridge) did so [13]. So Hutzler *et al.* [14], looking ever more closely: the experiment and its theoretical counterpart continue to be fascinating, with a never-ending pursuit of variations and complications [15].

Fig 1.3: In the standard textbook description of Newton's Cradle there is always only one sphere in motion. However, careful observation of the experiment shows that already after the first impact of a displaced sphere on one side, the entire chain begins to break up, with all spheres in motion. Theory and computer simulations confirm this and attribute it to the finite elastic modulus of the spheres [14]. The photograph shows the stainless-steel sculpture For every action ... by Fiona Mulholland (2005), permanently sited at Beacon Court South Quarter, Sandyford, Co Dublin. (Photo reproduced with kind permission by the artist).

1.3 Playing with Soap Bubbles

Soap bubbles can provide another homely source of inspiration, as they have done for centuries, in art, for which the definitive review is that of Emmer [16], and science, whose elementary aspects were described by Isenberg [17].

Staring into a foam with the naked eye, or with the help of a magnifying glass, will reveal local order amongst the randomness. Three soap films always meet in a line under an angle of 120 degrees, and four such lines meet under the tetrahedral angle of 109.4 degrees. The lines are called Plateau borders in honour of the Belgian scientist Joseph Plateau who was the first to describe them. His experiments were undertaken after he became blind (rashly staring at the sun, in the interests of science), so some of them may well have been performed in a domestic environment, with the help of his wife [18].

Soap films and bubbles as the simplest example of soft condensed matter [19] are one of the most attractive phenomena for people in different disciplines, ranging from art to science. Artists used soap bubbles as a metaphor and to express the sense of fun and game. Physicists, chemists, and biologists focused on the macroscopic and molecular properties of soap films and mathematicians worked on minimization problems related to soap films and bubbles.

A number of mathematicians such as Maupertuis and Euler used soap films and bubbles to figure out and demonstrate their mathematical ideas related to minimization principles. The Belgian scientist Joseph Plateau and Josiah Willard Gibbs are associated with the first detailed analysis of the geometry and stability of soap films and bubbles. Charles Vernon Boys is famous for giving lecture demonstrations using soap films and bubbles. In public lecture demonstrations, the English physicist Cyril Isenberg showed soap film arrangements in wireframes (Fig. 1.4), including the interference patterns in such films. Furthermore, there are many examples and demonstrations of soap

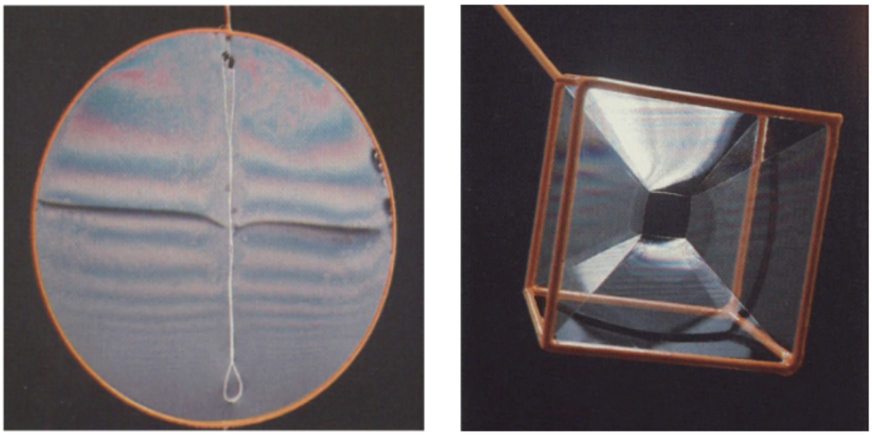

Fig 1.4: Soap film patterns produced by dipping two-dimensional and three-dimensional wire frames into a bath of soap solution. Left: Planar minimum area surface bounded by a circle for a disk of soap film. Right: Arrangement of films in a cubic wire frame [17].

films and bubbles with emphasis on the changes in film configuration which occur when the dimensions of the wireframes are altered.

Moreover, soap films and bubbles were used to demonstrate atomic models, first- and second-order phase transitions, catastrophe models based on catastrophe theory, the catenoidal surface by film within a wedge, minimization problems, to describe the geometric structure of proteins [20], to study the tropical cyclones [21], and as shown in Fig. 1.5 It can also assist architects in designing the Olympic swimming pool for the Olympic Games 2008 in Beijing, China [22].

Experiments with soap films and bubbles can help demonstrate physical principles from micro- to macro-scales. They can also highlight the role of geometry in biological cells.

In sections 1.3.1,1.3.2, and 1.3.3 we will briefly describe three examples for the use of soap films and bubbles to demonstrate science, before detailing our new contributions in chapters 2 and 3.

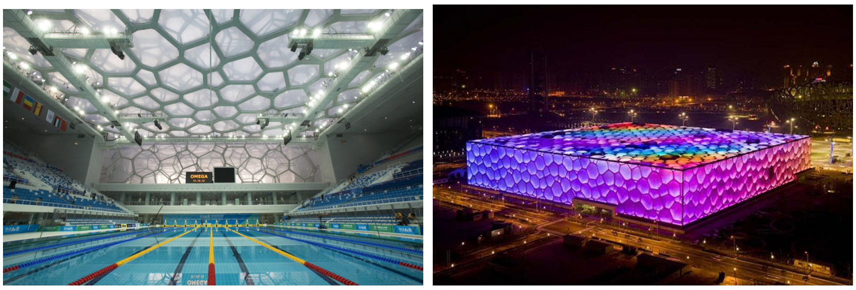

Fig 1.5: The "Water Cube" swimming center for the Olympic Games 2008 in Beijing, China (Source: *www.segd.org/interactive−architecture*). The giant block of foam is made of the Weaire-Phelan structure [23] (Source: *www.stadiumbase.com/listing/beijing − national − aquatics − center/*).

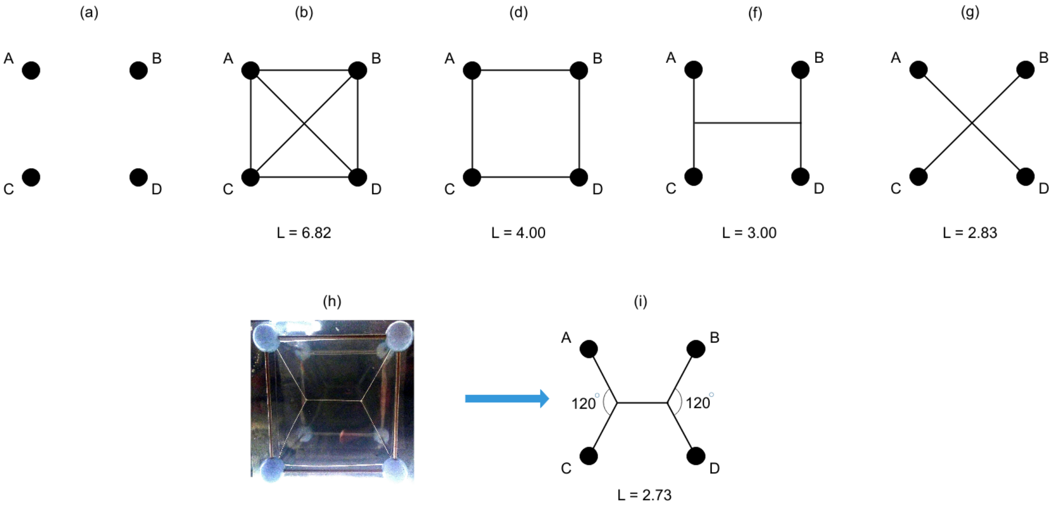

Fig 1.6: Different motorway configurations with corresponding total length: (a) Four towns A, B, C, and D at the corners of a square of unit length. (b) to (g), four possible motorway paths. (h) The minimum path linking the vertices of a square as realized in the equilibrium configuration of soap films (soap films appear as thin light bright lines shaped). (i) Corresponding to (h)

1.3.1 The Motorway Problem

An intriguing example of mathematical minimization problems is the motorway problem, i.e. the task of finding the shortest path linking n points. The shortest path linking two points is the straight line joining the two points as we all learn early in life. If one attempts to generalize this result by increasing the number of points the problem becomes increasingly more difficult and has not been solved analytically, it needs to be determined by numerical simulation.

As an example, consider the problem of linking four towns A, B, C, and D by a motorway, where the towns are located at the corners of a square of unit length (Fig. 1.6 (a)). Obviously, there are a number of ways to connect them, however, finding the optimal configuration is difficult. Four different examples of these networks are shown in Fig. 1.6 ((b) to (e)). The problem is how can one prove that there is no shorter path and how can we find the optimal path?

This problem will be solved using the minimization property of the line of a soap film. To obtain the minimum total length for the four towns using soap films (Fig. 1.6 (i)), one can use two parallel transparent plates joined with four pins. Immersing this arrangement in a bath of soap solution and withdrawing it from the bath the optimum path will be formed by the equilibrium soap film configurations (Fig. 1.6 (i)). Each intersection consists of three roads meeting at equal angles of 120 °. Physically this is the consequence of the equilibrium of forces at the three intersections. Therefore the minimum total length is 2.73. Similarly, using soap bubbles is an easy way to find the shortest path linking n points.

1.3.2 Shapes of Biological Cells

There are cells in biology called epithelium (skin) cells that form protective barriers and must remain firmly packed together to not permit gaps when the

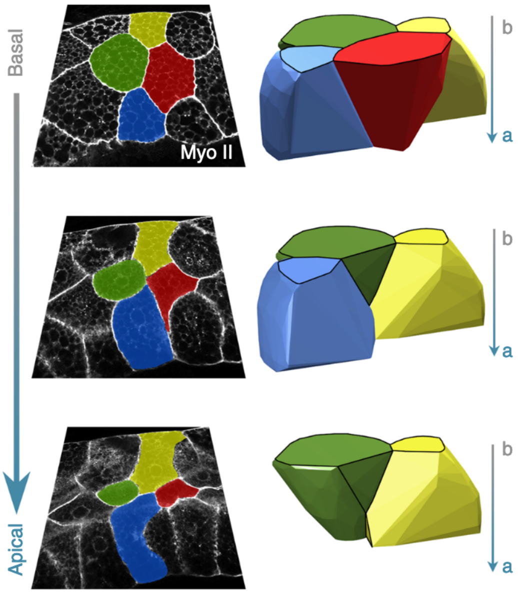

Fig 1.7: Confocal microscope images showing the apico-basal epithelial cells (left), and the 3D reproduction of the same cells (right) [24].

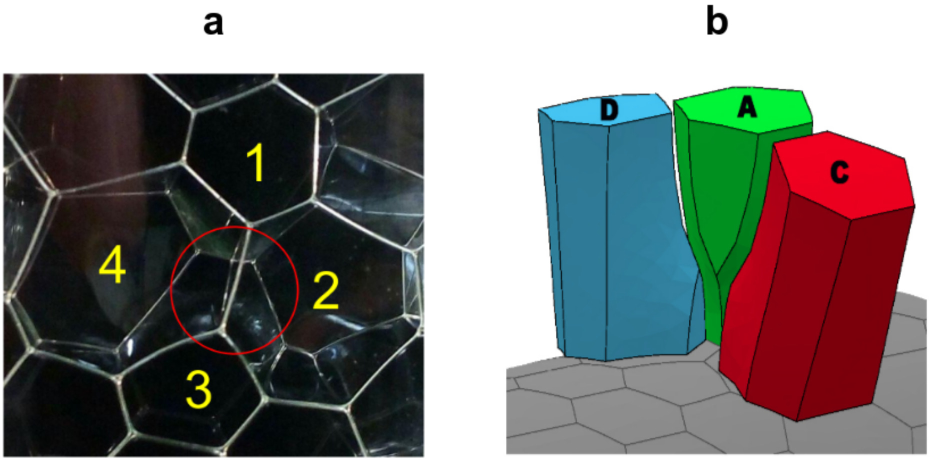

Fig 1.8: The scutoids in a soap froth. a) The bubble on the left (No. 4), has a heptagonal face at the top and a hexagonal face at the bottom, and a Y-shaped arrangement in is a scutoid. b) Computer simulation using the Surface Evolver software, the standard numerical tool for computing the structures of foams.

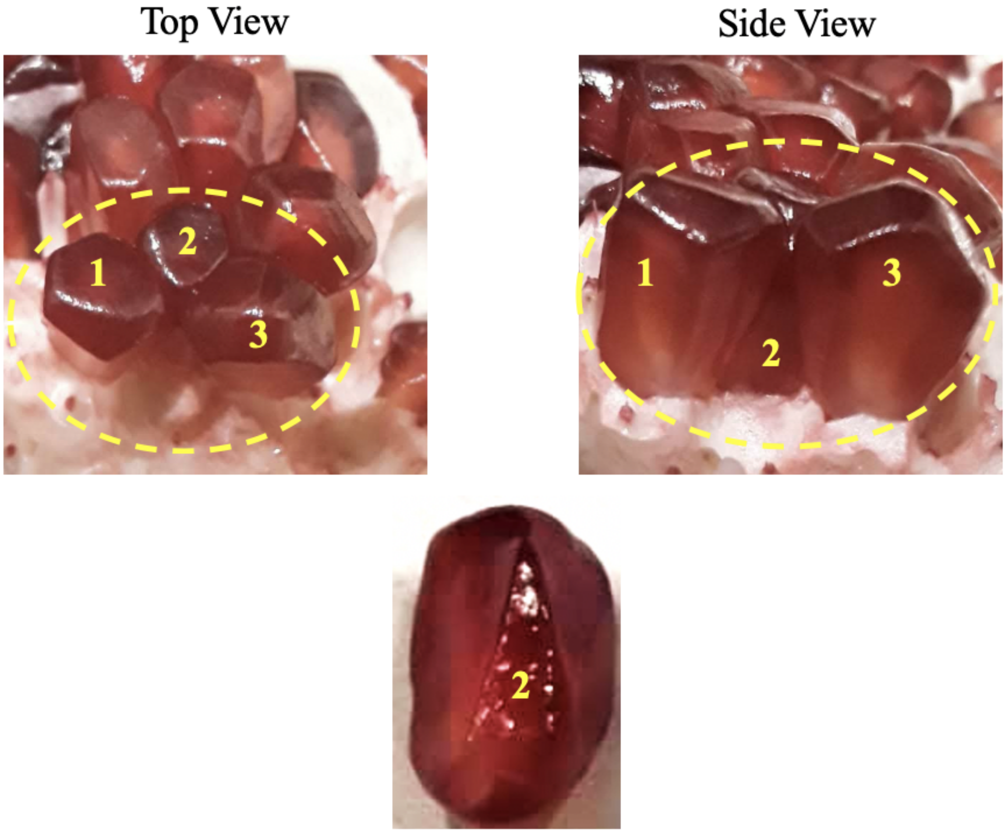

Fig 1.9: It is noteworthy that the recently discovered geometric shape known as scutoid can also be found within pomegranate seeds as I observed the Y-shaped arrangements.

surfaces are deformed.

Biologists recently showed that the usual representation of cells or the epithelium tissues, as prisms or truncated pyramids, did not match microscopical observations. The new type of columnar structures in epithelial cells as shown in Fig. 1.7, was called the *scutoid* by Gómez-Gálvez *et al.* [24]. Using an advanced model based on energy minimization this pillar-shaped structure could be computed.

By considering the similarity between bubbles in foams and cells in tissues both remaining tightly packed together to not allow any gaps when the surfaces are curved, Mughal *et al.* [25] carried out an experiment with soap bubbles, sandwiched between curved surfaces formed between two glass cylinders with different diameters. The bubbles were produced using a simple aquarium pump and commercial dish-washing solution and by changing the spacing between the two cylinders the scutoid has been observed. In Fig. 1.8 such a structure is shown. Furthermore, the scutoid has been observed in the pomegranate as well (see Fig. 1.9).

It was also possible to simulate its geometry using the standard software for the computation of structures with minimal surface area.

1.3.3 Visualization of Sound Waves

Blowing air carefully through a straw into some soapy water (or using an aquarium pump borrowed from your fish) results in the generation of bubbles of equal size. These crystallize spontaneously to form a hexagonal pattern (triangular lattice) on top of the soap solution, with some defects, such as dislocations, among them.

A standing sound wave in a tube can be visualized by the displacement of a light powder [1], whereas an alternative for the visualization of acoustic

---

[1] https://www.youtube.com/watch?v=wvJAgrUBF4w

waves is using soap films and bubbles [26].

Thickness variations in a soap film lead to interference effects where the light falls onto it. The (local) thickness varies in response to the interaction of the film with sound waves, which leads to a redistribution of the liquid making up the film. The soap films act as vibrating membranes with time-dependent thickness.

To visualize the sound wave, Elias *et al.* [26] placed soap films (equally spaced) inside a transparent cylindrical tube. A standing sound wave was generated in the tube by connecting a loudspeaker connected to a sound wave generator to one end of the tube while the other end was closed to air. The soap films which are located nearby the displacement antinodes vibrate leading to the redistribution of liquid, while those soap films close to the displacement nodes remain thin and static (see Fig. 1.6). This simple experiment to visualize the sound waves and the wavelength of standing waves in the tube is easy to perform in classroom demonstrations.

Having introduced these examples where soap films and bubbles can be used to demonstrate and solve problems in physics we will in chapter 2 describe our new contributions that should be seen in this spirit.

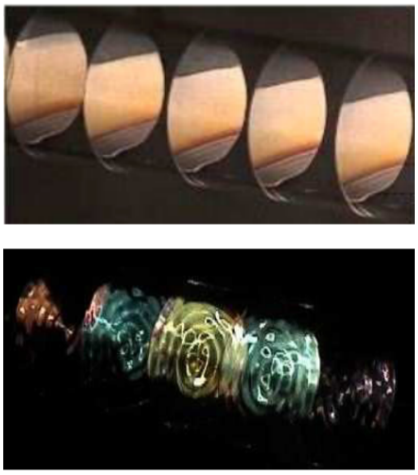

Fig 1.10: Visualization of sound waves using soap films. Top: Interference pattern in the absence of sound waves. The soap films are vertical and display a variation in colour (thickness) due to the gravitationally driven drainage Bottom: Fascinating patterns in the presence of sound waves. Measuring the distance between films with minimum interference patterns results in the wavelength of the sound wave.

1.4 Thesis Structure

In this thesis, we introduce simple but intriguing experiments that may be carried out safely and easily at home with widely available stuff. Most of them have to do with classical mechanics or basic material characteristics.

We begin in Chapter 2 with the buckling behavior of a linear chain of hard spheres confined in a cylindrical tube under compression and tilt. Our findings indicated that this system is characterized by instability and buckling behavior. We will discuss different arrangements of a such chain under compression and tilt and demonstrate there is critical tilt for buckling of the system.

In Chapter 3 we will present our extended study of the buckling of a linear chain of particles in which we hired soap bubbles instead of hard spheres. A simple experimental setup will be introduced that is well-suited for classroom or lecture hall environments to examine the buckling properties of chains of soap bubbles.

In Chapter 4, we describe a number of different experimental set-ups that use hydrogel spheres to demonstrate dense packings of deformable spheres in various geometries which grow by absorbing water. The arrangements are similar to those of bubbles in foams, drops in emulsions, biological cells, etc. The experiments are easy to perform in the classroom, with reference to the history of packing problems to which this convenient system, not yet explored, can add significant new findings.

Chapter 5 focuses on both empirical data and theoretical analysis regarding soap films to demonstrate the feasibility of utilizing survival and failure rate information from an ensemble of soap films to gain an understanding of the factors that govern infant mortality and the so-called bath-tub curve of mortality/failure.

Finally, in the last Chapter, we conclude our results, and we will discuss suggestions for future research in the areas of experiments with hard or soft spheres and future lifetime experiments with soap films.

At the end of each chapter, we present simple *"Do It Yourself"* experiments (in sections called **DIY Science: Hands-on Experiments**) which can be performed without the need for expensive advanced equipment and equipped laboratories. The experiments are suitable for use in the classroom, in undergraduate education, or even at home. Each experiment is categorized based on its accessibility, cost, and experimental time as follows:

Accessibility: the experiment has been categorized into three levels of accessibility based on the required materials:

★☆☆: Laboratory materials

★★☆: Materials that can either be purchased or produced at home.

★★★: Materials easily accessible in a kitchen or bedroom.

Cost: experiment is categorized into three levels of expense based on its cost:

💵: cheap (less than 5 €)

💵💵: moderate

💵💵💵: expensive (more than 30 €)

Duration: once the experiment has been set up, the experimental time refers to the actual time required, including analysis, to provide a complete description of the phenomenon.

⌛: short (less than 45 minutes)

⌛⌛: medium

⌛⌛⌛: long (more than 2 hours)

In Appendix A we present a simple heuristic model for buckling of hard spheres under tilt which is useful to understand the tilt experiment in Chapter 2. It follows by Appendix B the Morse–Witten model for deformable spheres as discussed in Chapter 3 will be introduced. Finally, Appendix C contains film lifetime data for all the different experimental set-ups that will be described in Chapter 5.

Chapter 2

Buckling Experiments Using Hard Spheres

> **The universe is expanding and we are compressing...**
>
> **— Denis Weaire**

2.1 Introduction

Fifteen years ago, I was fascinated by an animation called **Flatland** [1] which is based on a short novel written by Edwin A Abbott in 1884. The story describes a two-dimensional world occupied by geometric shapes. In this two-dimensional world, *women* are line segments, while *men* are polygons with various numbers of sides, with a **Circle** considered the *perfect* shape.

---

[1] https://www.imdb.com/title/tt0972374/

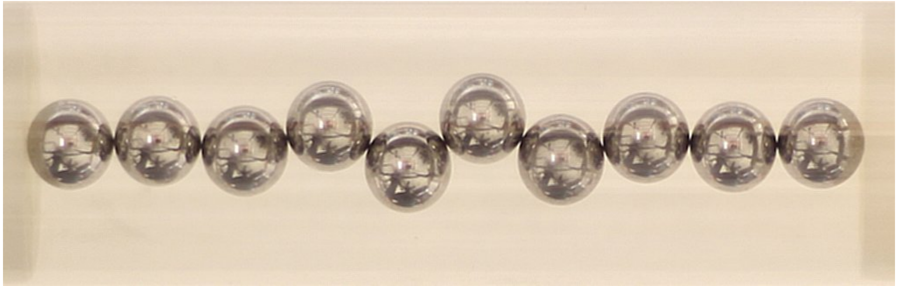

Fig 2.1: An example of a linear chain of 10 hard spheres (ball bearing) under compression which exhibits a zigzag pattern.

As a perfectionist (both psychologically and philosophically) circles and spheres are sacred and of special value to me. The main reason for the sanctity of these geometric shapes is their *symmetry*. While these shapes alone have symmetry, a chain of these particles, under certain conditions or forces, creates structures that will lead to symmetry breaking or instability.

In the current Chapter, we will discuss our experimental study of a linear chain of hard spheres confined in a transverse harmonic potential that displays instability and buckling behavior under compression and tilt. The spheres are confined in a tube by two opposing hard walls and are also subject to confinement in the transverse direction through the imposition of a cylindrical symmetric potential that vanishes along an axis perpendicular to the two hard walls. The linear chain exhibits a tendency to buckle and form various zigzag configurations under slight compression and tilt. For compression below a critical value, the structure remains planar, and it is within this regime that our investigation via experiments is focused. At greater levels of compression, more intricate three-dimensional structures emerge. Also, for a linear chain of hard spheres, we will show the buckling occurs at a finite critical tilt. Figure. 2.1 shows an example of a compressed chain of hard spheres confined in a cylindrical tube sealed at both ends which buckled like a zigzag pattern.

It is also important to mention that the simple experiments that will be introduced here will give us the key properties and concepts that people gain from expensive equipment used in ion trapping.

So, first, in Sections 2.1.1, 2.1.2, and 2.1.3, we will present some examples of such chain of particles as realized with both using soft or hard spherical or quasi-spherical particles and have led to structures that involve the concepts of instability and symmetry breaking in physics and express the buckling properties of the said systems. Then, in the entire Chapter, our study on buckling experiments using hard spheres will be discussed.

2.1.1 Self Assembly

Self-assembly is a native process and the fundamental principle which produces an organized structure at different scales, e.g. molecular, mesoscopic, and macroscopic scales such as galaxies in astronomical scales. It is the autonomous structural organization processes that occur naturally, without human involvement, to arrange individual components into patterns or ordered structures.

In a random self-assembly process, e.g., molecular, colloidal, interfacial self-assemblies, an ordered structure or pattern is generated as a result of specific, local interactions among the constituents individually and without any external direction. Other self-assembly processes are directional to some degree, e.g., atomic and biological self-assemblies.

Self-assembly is described as *"the non-covalent interaction of two or more molecular subunits to form an aggregate whose novel structure and properties are determined by the nature and positioning of the individual components"* [27].

Self-assembly is the innate capacity of a wide range of multimeric biological structures to assemble from their constituent components by random motions of molecules and the development of weak chemical bonds between surfaces with complimentary geometries. The phospholipid bilayer of human cell membranes [28], RNA [29], and DNA complexes [30] are a few examples of self-assembled structures that may be found in biological systems. Due to their amphiphilic characteristics, the detergent surfactant molecules show a process of self-assembly. Self-assembly is the basis of all molecular assembly processes that give rise to viral and bacteriophage particles.

Soto and Golestanian [31] studied the self-assembly of active colloidal molecules which has the exceptional feature of symmetry breaking. Furthermore, most of the structures of the self-assembled active molecules shown in Fig. 2.2 could be found in simple experiments using compressed chain of hard spheres confined in a cylindrical tube which will be described in the following chapters.

Colloidal particles show the non-equilibrium behaviour which may be driven up or down the gradient in a solution when the concentration of a solute is maintained as a gradient. Two independent parameters determine the non-equilibrium behavior of the catalytic colloids. The first parameter, surface activity α, describes the production or consumption of chemicals at the colloidal surfaces. The second parameter is the surface mobility μ, which defines how the colloid reacts to chemical gradients produced by that colloid or by other active colloids in the medium. Figure 2.2 shows three examples of such colloidal particles with different values of α, and μ results in self-propelled molecules, self-rotating molecules, and inert molecules. The surface chemistry of the colloids may be changed to regulate both parameters, which can independently be positive, negative, or zero. A single symmetrically coated, spherical colloid cannot move by itself, however two of these colloidal particles may be able to move together through phoretic contact.

2.1.2 Microswimmers

Another example that exhibits buckling in the form of a zigzag structure will be discussed here.

Microswimmers are microscopic objects (natural and artificial), that can

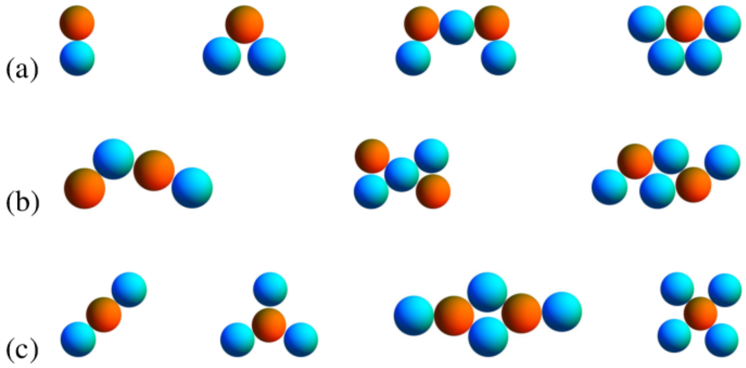

Fig 2.2: Self-assembly of catalytically active colloidal molecules [31].

move across a viscous medium by converting chemical energy into mechanical work [32].

Microswimmers can be biased and have a preferred swimming direction toward or away from a stimulus, such as light, or in response to certain chemicals in the environment [33, 34]. In essence, the mechanism is important for bacteria like E. coli (about 2 μm in length and 0.5 μm in diameter) to find food by swimming toward the highest food concentration. Furthermore, the mentioned mechanism plays a crucial role in the early development of multicellular organisms like sperm [35].

In addition, two decades have passed since the emergence of artificial microswimmers, and they have already shown promise for various industrial, biomedical, and environmental applications. For instance, in the future, spherical microswimmers robots could purify polluted water and make it drinkable in which each of the hemispheres of these swimming machines has a different material. One side is made of magnesium and the other side has an alloy of iron, gold, and silver. Magnesium reacts with water to produce hydrogen bubbles and propel the robot. Harmful microorganisms are also absorbed by the gold layer and destroyed by silver nanoparticles.

Lauga *et. al.* studied one-dimensional lines of microswimmers. They addressed a collection of microswimmers with a preferred swim direction that

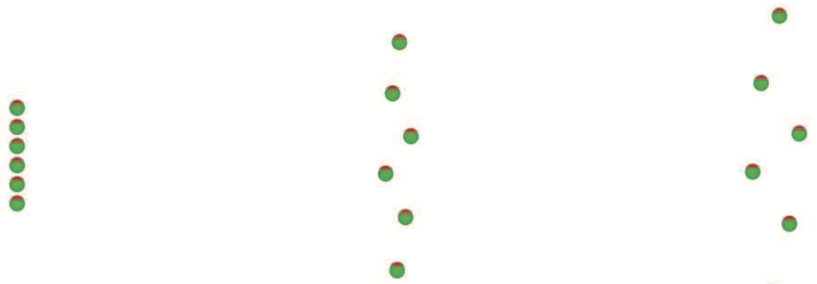

Fig 2.3: Zigzag instability of microswimmers. The initial arrangement of a group of microswimmers exhibits linearity, as depicted on the left. The location of the microswimmers that exhibit upward motion against gravity and move in a linear direction is unstable, leading to the formation of a zigzag pattern. The rate of growth of this instability is directly proportional to the magnitude of the stresslet. [36]

gravity is a stimulus for them, so they can swim upward [36].

Lines of such swimmers were then shown to be subject to clustering instability. Their study makes the assumption that microswimmers swim at very low Reynolds numbers[2], are neutrally buoyant and are non-Brownian. The swimmers were biased in their locomotion by making the swimmer's bottom heavy which adds a restoring gravitational torque (that aligns their direction opposite to gravity) to swim vertically upward [36].

Fig. 2.3 shows a zigzag instability of such microswimmers. The instability is manifested when the microswimmers display upward motion against gravity as described above and move in a linear manner, resulting in the creation of a zigzag pattern. The growth rate of this instability is directly related to the stresslet's magnitude.

---

[2] The Reynolds number is the ratio of inertial forces to viscous forces within a fluid which is subjected to relative internal movement due to different fluid velocities.

2.1.3 Ion Trapping

From microswimmers to ion chains!

The last example that shows the transition from a linear chain to a zigzag structure is described in the following.

Ion trapping is a technique used in physics, chemistry, and other related fields, in which ions are confined and isolated in a specific region of space using electromagnetic fields. This technique can be employed for a variety of purposes, such as studying the properties and behavior of individual ions, manipulating chemical reactions, and developing new technologies like quantum computers [37–39].

Quantum computers require qubits to store quantum information. The basic elements of the quantum computer (i.e., the qubits) are the ions themselves. A realistic physical system to create a quantum computer is provided by cold ions interacting with laser light and moving in a linear trap [37].

By applying various laser beams to each of the ions in this system, it is possible to manipulate each qubit independently. The ions have been previously laser cooled in all three dimensions such that they oscillate by small amounts around the equilibrium state [38]. Fig. 2.4 shows the spectrum of a chain of these trapped and laser-cooled ions from a linear to zigzag instability at finite temperatures [40, 41].

Following a comprehensive introductory overview of three examples from different areas that showed buckled structures such as zigzag patterns, the remainder of this chapter presents a discussion of our experimental findings obtained from a linear chain of rigid spherical particles. To establish a comparison between our experimental results and those obtained through computational methods, selected computational results have been included. It is worth noting that the entire experimental work described in this chapter was conducted by me, while the numerical, computational, and simulation

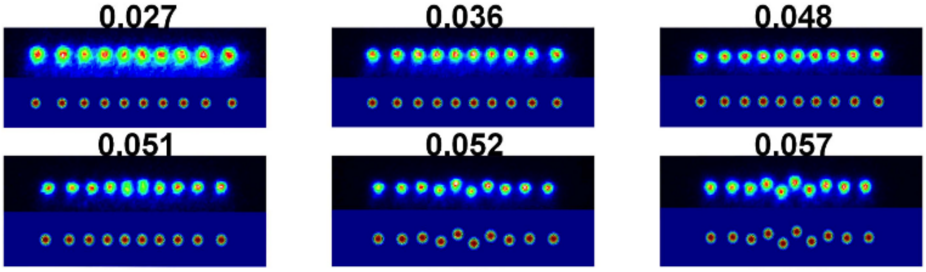

Fig 2.4: An illustration of a group of ten $^{40}\mathrm{Ca}^{+}$ ions with various values of trapping potentials which shown above each configuration, showing experimentally obtained pictures (top of each panel) and the outcomes of numerical simulations (the bottom of each panel). With an increase of the confinement, a transition occurred from the linear chain to a zigzag instability [41].

studies were carried out by Prof. Stefan Hutzler (my Ph.D. supervisor), Dr. Adil Mughal (Aberystwyth University, UK), and Mr. John Ryan Parcell (PhD student in our group).

2.2 Experiments with the Linear Chain of Hard Spheres under Low and High Compression

Prior studies primarily focused on identifying three-dimensional structures under high compression and employed the utilization of a lathe to generate a harmonic confinement potential [42, 43]. In our research, a more straightforward experimental setup, suitable for both low and high compression, is presented.

Fig 2.5: A chain of 30 hard spheres with a diameter of 6.32 *mm* confined in a perspex tube with an inner diameter of 1.6 *cm*) is buckled under high compression illustrating a localized buckling. This represents one of the stable configurations and the situation can be symmetrical about the x-axis.

Here, we examine the buckling of a linear chain of hard spheres which is confined in an approximately quadratic harmonic potential. This chapter delves into the buckling characteristics of such a chain when confined between hard walls and subjected to transverse harmonic confinement.

In the current Section, we present our experimental results for two distinct regimes of compression, namely low compression leading to buckling of the entire chain, and higher compression resulting in *localized buckling* which refers to a phenomenon where one or more spheres in the chain buckle under compression, while the other spheres in the chain remain unaffected and linear. This type of buckling is called "localized" because it occurs in a specific region of the chain, rather than propagating throughout the entire chain. An example of such localization is shown in Fig. 2.5.

Then, in Section 2.3, we will explain another experimental system in which we simply tilt the tube containing a line of hard spheres that becomes unstable and buckles upon tilting beyond a critical angle.

By utilizing hard spheres (such as ball bearings) placed within a cylindrical tube, all localization properties can be demonstrated. Provided that the diameter of the cylindrical container surpasses that of the spheres, the system can be considered approximately planar. The quadratic harmonic potential is generated through the effect of gravity. Fig. 2.6 shows our experimental system of this nature was depicted in for compression $\Delta = 1.04$ ($\Delta = N - \frac{L}{D}$). Here $N = 8$, ball bearings with diameter $D = 9.5\ mm$ and mass $m = 3.52\ g$, confined in a cylindrical perspex tube with diameter $D_T = 34\ mm$.

2.2.1 Experimental method and results

In these experiments that were performed during the *Covid-19* pandemic in a small bedroom in Dublin, eight steel spheres with a diameter of $D = 6.33$ mm were used and confined in a cylindrical tube with an inner diameter of 20.05 mm. The tube was sealed at both ends with stoppers, one of which was

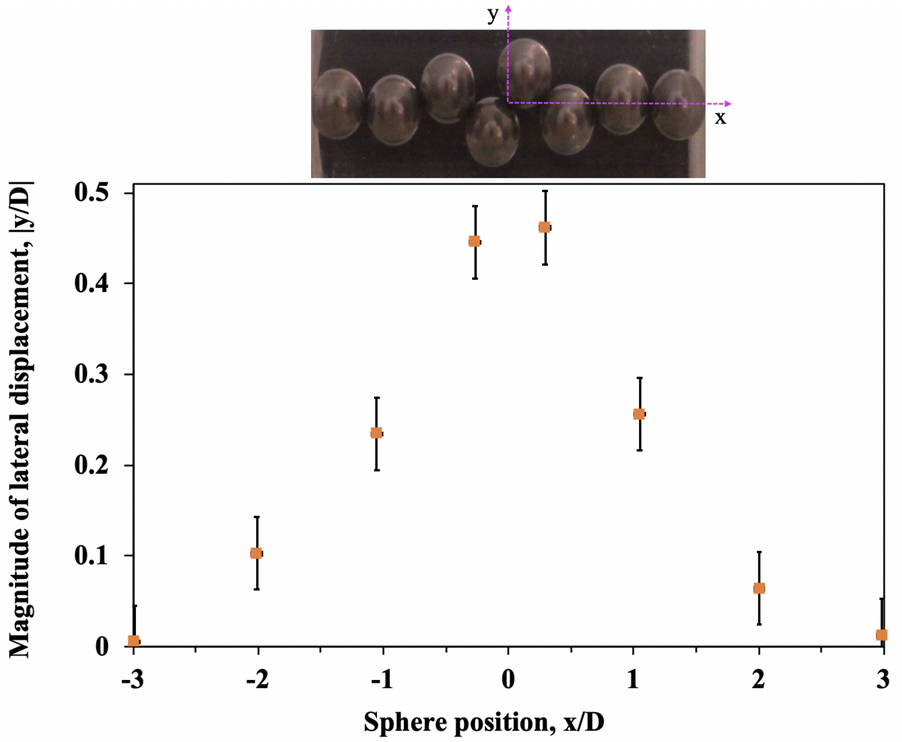

Fig 2.6: The accompanying photograph depicts an elemental experiment displaying a chain of $N = 8$ hard spheres subjected to compression. The magnitude of the transverse displacement of the sphere centers is also depicted. Both the position and displacement values are normalized in relation to the sphere diameter. It should be noted that the inclusion of oil in the plastic cylinder, which serves to mitigate friction, leads to an optical distortion in the photograph. The observed ratio of sphere extension to sphere diameter (where $D = 6.33mm$) in the x and y directions was approximately 0.98 and 1.11, respectively. The error bars in the figure indicate the measurement uncertainty of the sphere centers as determined using ImageJ, and have a magnitude of ±0.04 sphere diameters in both the x and y directions.

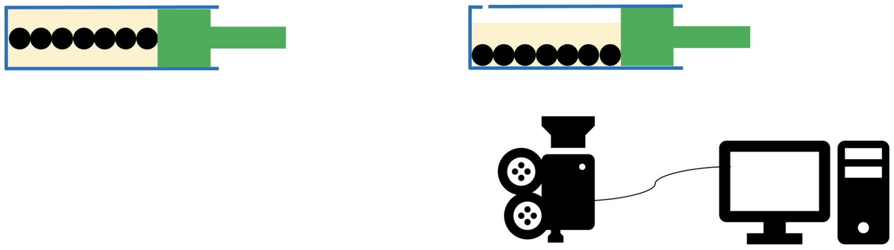

Fig 2.7: Sketch of the experimental setup. Left: the bottom view of a chain of hard spheres under zero compression. Right: a side view of the system. As the chain was compressed with a mobile stopper, the photos were captured using a digital camera underneath the tube which was connected to a PC.

adjustable to change the length of the tube during the experimental process. To reduce friction, the spheres were immersed in vegetable oil. An aperture was made in the upper half of the tube to allow air to escape as the stopper was moved inward. The tube was kept horizontal using a spirit level. Fig. 2.7 shows the sketch of the experimental setup and procedure. The degree of compression Δ was determined using Eq. 2.6, where L is the length of the chain and $N = 8$ spheres were used in all experiments.

In Figure 2.8(a), a series of images depicting the progression of compression on a chain of eight spheres are displayed. The images reveal that buckling occurs symmetrically around the center of the chain. In addition, localized buckling and doublet formation can occur at high compression values of $\Delta = 1.04$ and $\Delta = 1.32$ respectively. Using image analysis software (*ImageJ*), the positions of the spheres were determined, which enabled the measurement of the angles between them. The resulting angle profiles, presented in Figure 2.8(b), are found to align well with the theoretical simulations described in section 2.4.

One further experiment we intend to discuss here is the buckling behavior of a chain of hard spheres under tilt which will be discussed in the following section.

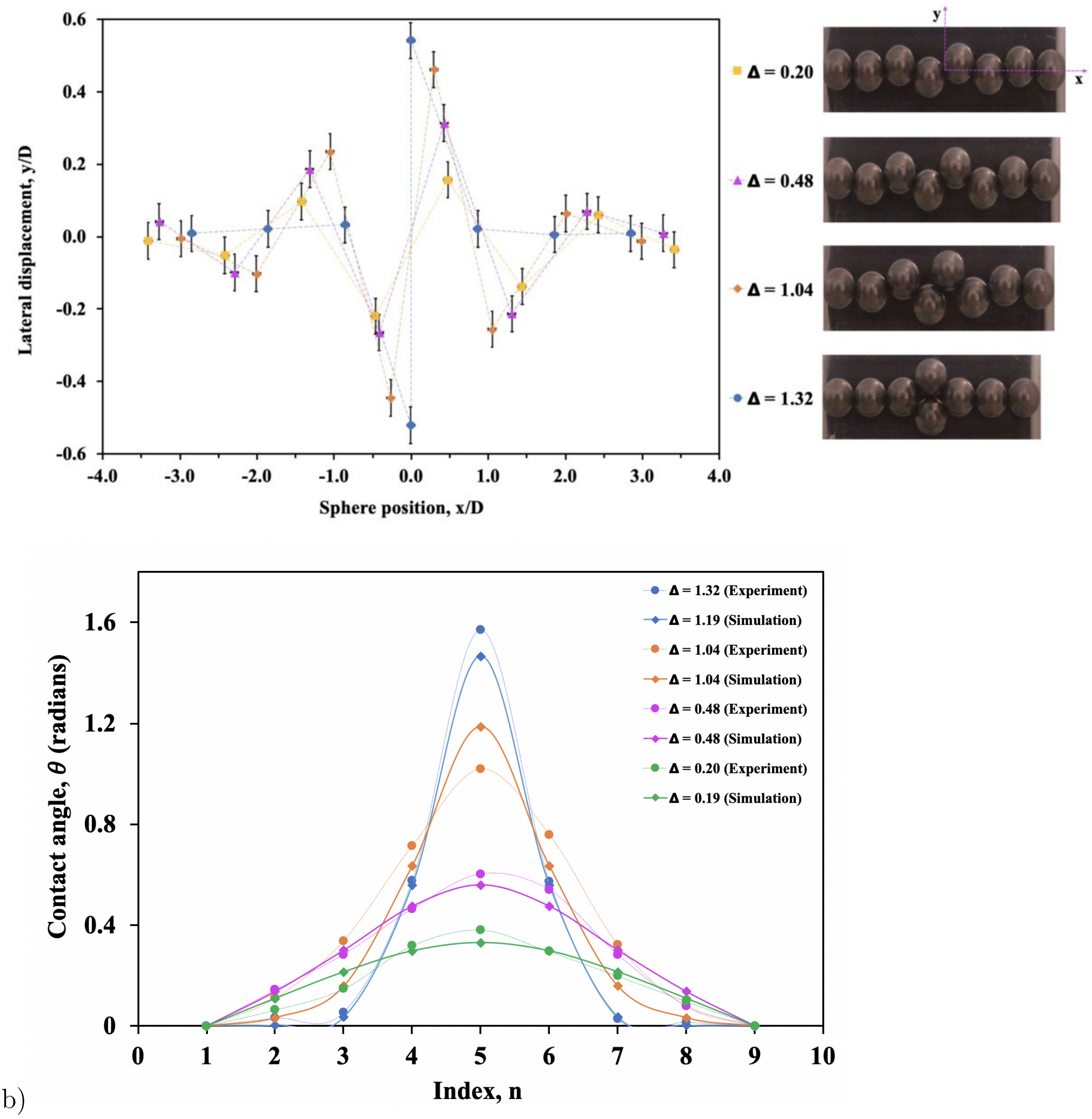

(a)

(b)

Fig 2.8: Experimental data for a chain of N = 8 hard spheres under different values of compression Δ. (a) Displacement profiles. At compression Δ = 1.32 we observe a doublet structure which refers to a specific arrangement of spheres where two neighboring spheres are in contact with three neighbors, while the rest spheres have only two contacts. (b) Profiles of contact angles θ_i for several values of compression. The Eq. 2.5 solved to obtain the numerical results in the case of $\tau = 0$. The experimental data are roughly matched by our numerical results.

2.3 Linear chain of hard spheres under tilt

As discussed in section 2.2, the compression of a straight linear chain of hard spheres leads to buckling, characterized by lateral displacements of the spheres. For the purposes of this thesis, the confining potential still will be approximated as harmonic for sufficiently small transverse displacements. This results in a buckling profile that is dependent on the degree of compression and exhibits multiple forms at high levels of compression.

Here, a longitudinal force was introduced, acting on each sphere, by *tilting* the apparatus (so that a component of gravity plays the role of the longitudinal force). The movement of localized buckling concentration under the influence of the longitudinal force, is of further interest, in relation to Peierls–Nabarro potentials [11].

In the following, we present our experimental results for a chain of hard spheres under low compression.

2.3.1 Experimental method and results

The experiments were carried out with metal spheres (sets of ball bearings with diameter $D = 9.5mm$ and mass $m = 3.52g$), confined in a cylindrical perspex tube (diameter $D_T = 34mm$) which was filled with vegetable oil to reduce friction. The angle of tilt of the cylinder against the horizontal was determined using a digital spirit level (Neoteck NTK034). The cylinder was sealed with rubber stoppers at both ends; the surface of the stopper in contact with the spheres was covered with a circular plastic sheet to further reduce friction at the contact point. Figure. 2.9 shows a sketch of the experimental set-up for a chain of hard spheres under tilt.

Here, we present our experimental results. However, the challenge of conducting these experiments lies in the inherent frictional forces that arise between the spheres, typically hard spheres (ball bearings). This issue can

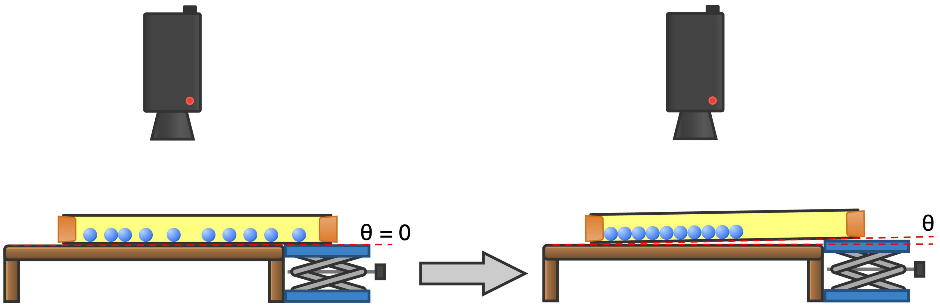

Fig 2.9: A sketch of the experimental setup for a chain of hard spheres under tilt. Sets of hard spheres with diameter $D = 9.5mm$ and mass $m = 3.52g$ confined in a Perspex tube with diameter $D_T = 34mm$ which is filled with vegetable oil that was sealed at both ends. Left: initially, the tube is horizontal, $\theta = 0$. Right: by tilting the tube for an infinite tilt angle, $\theta > 0$, and the procedure described in Section 2.3.1 the chain starts buckling at a critical value of tilt.

be addressed using bubbles, as discussed in Chapter 3. Nevertheless, this alternative approach also presents its difficulties, as bubbles are deformable, and therefore, the current theoretical framework would need to be expanded to incorporate this new aspect.

The stability of a chain of spheres confined in a tube, when subjected to tilt, was investigated experimentally. The results showed that when the tube was simply tilted, no instability was observed until the tilt was significantly greater (by a factor of 3) than a critical tilt calculated for an ideal system of hard spheres (see Section 2.4 for theory). This suggests that friction between the spheres is sufficient to keep the system in its straight-chain arrangement, up to a certain point.

The experimental procedure consisted of starting with an initially linear arrangement of spheres and tilting the tube away from the horizontal by a tilt angle α. This was followed by ten cycles of manual rolling of the tube back and forth, with a fixed period of 10 seconds and a specified amplitude.

In order to overcome the effects of friction, large perturbations were avoided as they tend to force the system into a doublet arrangement (doublet structure

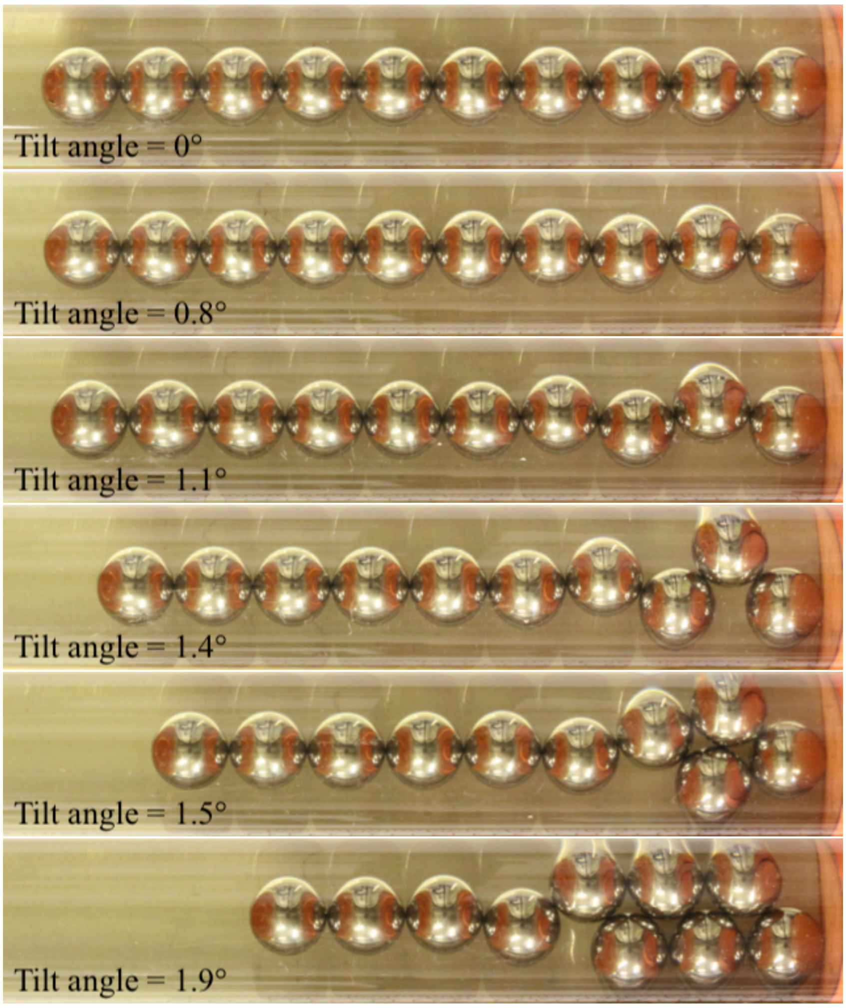

Fig 2.10: Sphere arrangements were obtained using the rolling procedure described in the text. The examples shown are the straight chain (no tilt), buckled single peak structures for tilt angles 0.8, 1.1, and 1.4 degrees, respectively, a *skewed doublet* structure for 1.5 degrees, and a *zipper* structure for 1.9 degrees. (The presence of oil in the tubes results in optical distortion. We have corrected this in these images by re-scaling the photographs by a factor of 2.04 to result in circular shapes for the sphere. Sphere diameter 9.50 mm, inner tube diameter 34 mm, uncertainty in angle measurements, 0.03 degrees. Rolling amplitude, 30 mm.)

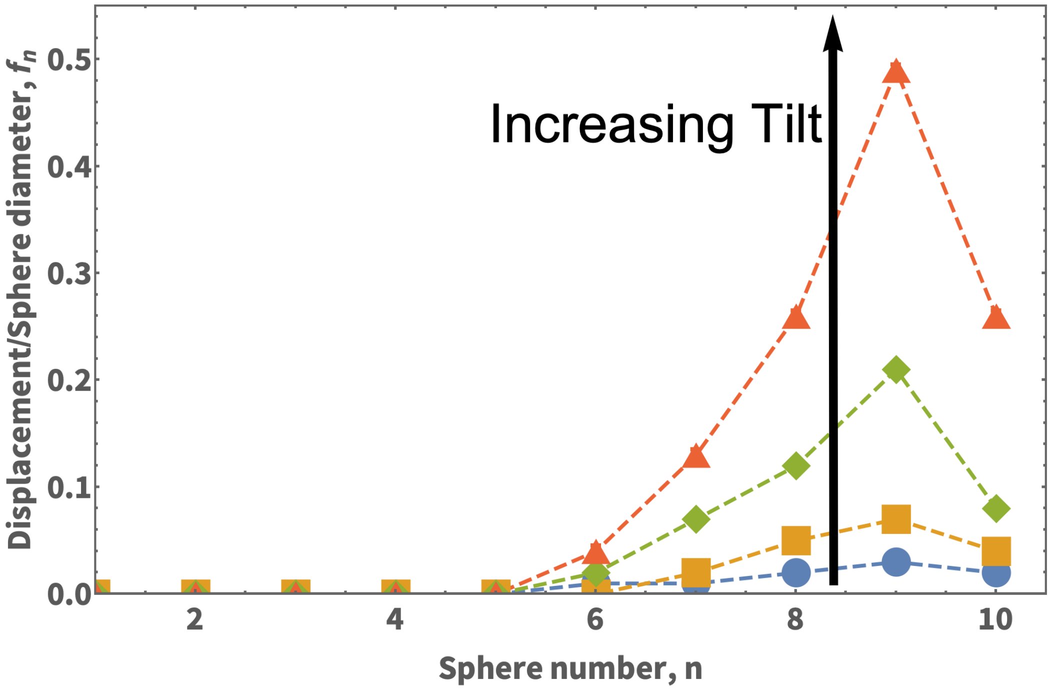

Fig 2.11: Experimental displacement profiles for (from bottom to top) tilt angles 0.40, 0.80, 1.10, and 1.40 ±0.03 degrees, corresponding to τ = 0.009, 0.018, 0.024, and 0.0315 (using Eq. 2.12 for conversion).

refers to a specific arrangement of spheres where two neighboring spheres are in contact with three neighbors, while the rest of spheres have only two contacts) over a wide range of tilt angles. Instead, the tube was gently rolled back and forth, providing a perturbation to the linear chain.

A picture was captured after the rolling process was concluded, with Figure 2.10 presenting visual illustrations of the arrangement of spheres for varying tilt angles. The sphere arrangement profiles, relative to the axis of the tube, were obtained through the utilization of image analysis techniques utilizing *ImageJ* software. In order to ensure accurate results, the experiments were conducted three times at each specified angle, with each iteration commencing from an initially linear arrangement of spheres.

Our findings demonstrate that, despite the initiation of the experiments with a straight-line configuration of spheres, upon cessation of rolling, even for

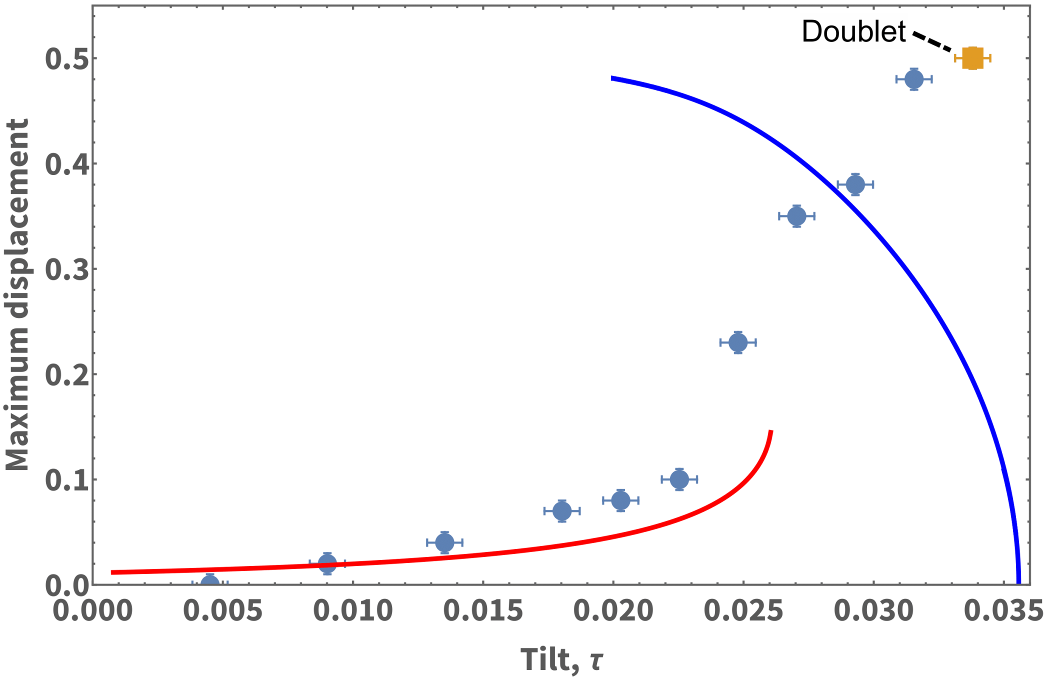

Fig 2.12: Contrasting experimental and simulated results for maximum displacement (i.e. corresponding to the displacement of sphere 9) as a function of tilt τ. In the simulation, solving the iterative Eqs. 2.5 will result in the solid blue line which indicates the amplitude of the *unstable* buckled state decreases to zero at the critical value τ_c, where the spheres rearrange to form a doublet structure (see Fig. 2.13). Unlike the simulation, in the experiment (data points) the buckled state is friction-arrested, with increasing amplitude as the doublet is approached. To interpret the experimental data, a simple heuristic model, as described in Appendix A is used (solid red line).

values of tilt well below τ_c, the system did not revert back to its original linear form. On the contrary, a consistent result was observed with the formation of a single crest-shaped zigzag pattern.

However, the friction causes the observed displacement to increase with tilt, as shown in Fig. 2.11.

Figure 2.12, displays a comparison between numerical and experimental data regarding the maximum displacement of the ninth sphere as a function of the tilt angle τ. This comparison highlights the different behavior of the system as it approaches the critical point in experiment and simulation as the

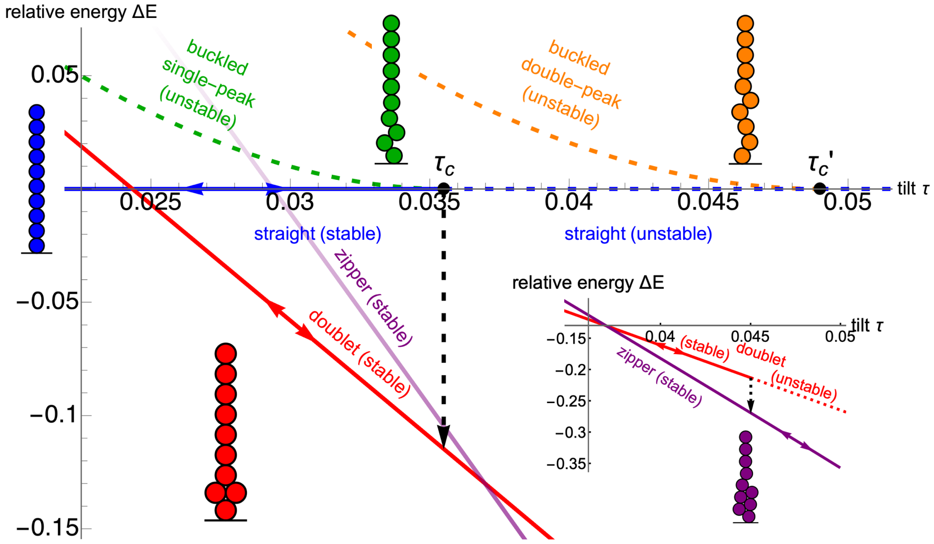

Fig 2.13: Bifurcation diagram for a system with $N = 10$, obtained from simulations. Shown is the variation of the energy difference $\Delta E = E - E_s$ of total energy E (Equation 5) and energy of the straight chain, E_s, as a function of tilt τ. Examples of the various structures described in the text are shown, with arrows indicating allowed directions of change of stable solutions. The transition from the doublet to the zipper structure is shown in a close-up in an inset. Here, the key difference between the experiment and simulation about the formation of a doublet as shown in Fig. 2.12 can easily be seen as simulation predicts a doublet structure even at lower tilts.

friction plays a key role here. As shown in Fig. 2.11, despite the experiments the displacement will increase with tilt, in the simulation we observed different behavior. See Fig. 2.12 and 2.13. The bifurcation diagram (Fig. 2.13, shows a doublet structure can be observed even for lower tilt in the simulation which is different from experiments (doublet will be formed at a higher tilt) as already shown in Fig. 2.12.

Calculating the critical tilt for a specific number of spheres (N) is a straightforward task. However, the study's objective is to broaden its scope and analyze the nature of the buckling transition and other relevant buckling states, summarized in Fig. 2.13.

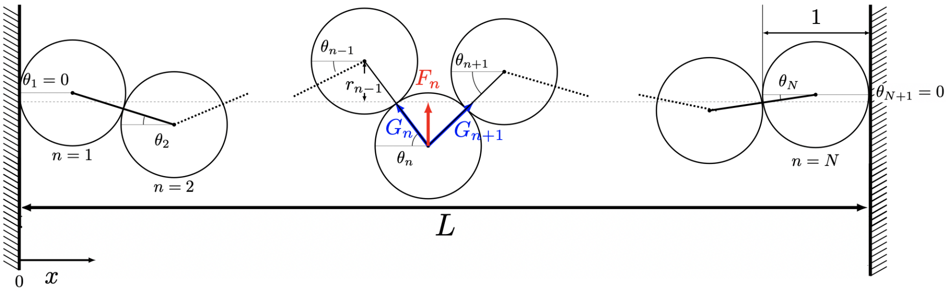

Fig 2.14: Schematic for the analysis of a chain of hard spheres under compression. In non-dimensional units, the transverse restoring forces F_n equals the transverse displacements y_n. G_n is the compressive force between contacting spheres $n-1$ and n. G_0 is the compressive force exerted by the top wall on the first sphere, $n = 1$. The angles θ_n are defined so as to be always positive for the modulated zig-zag structures (hard walls: $\theta_0 = \theta_N = 0$).

2.4 Theory

As explained in Section 2.2, we examine a chain of N contacting identical hard spheres that are compressed between hard walls, as illustrated in Fig. 2.14. Displacement of a sphere by a distance R_n away from the central axis results in a transverse restoring force (the transverse restoring force is provided by the curvature of the cylinder) f_n with magnitude kR_n, where k is a force constant. We introduce non-dimensional quantities by defining $r_n = R_n/D$, where D is the sphere diameter. The dimensionless transverse force F_n is defined as $F_n = f_n/(kD)$. Inserting for f_n leads to $F_n = r_n$; in our non-dimensional formulation, the transverse force F_n acting on a sphere equals its transverse displacement r_n, a positive quantity.

Figure 2.15 illustrates the buckling behavior of a chain of hard spheres under low compression. Without the application of a longitudinal or tilt force, buckling occurs at an infinitesimal compression. However, in the absence of a confining boundary at the upper end of the system, the buckling occurs at a finite critical tilt, as shown in Fig. 2.15. This scenario can be related to the collapse of a tower under gravity, where the lateral confining potential is equivalent to the tower's stiffness.

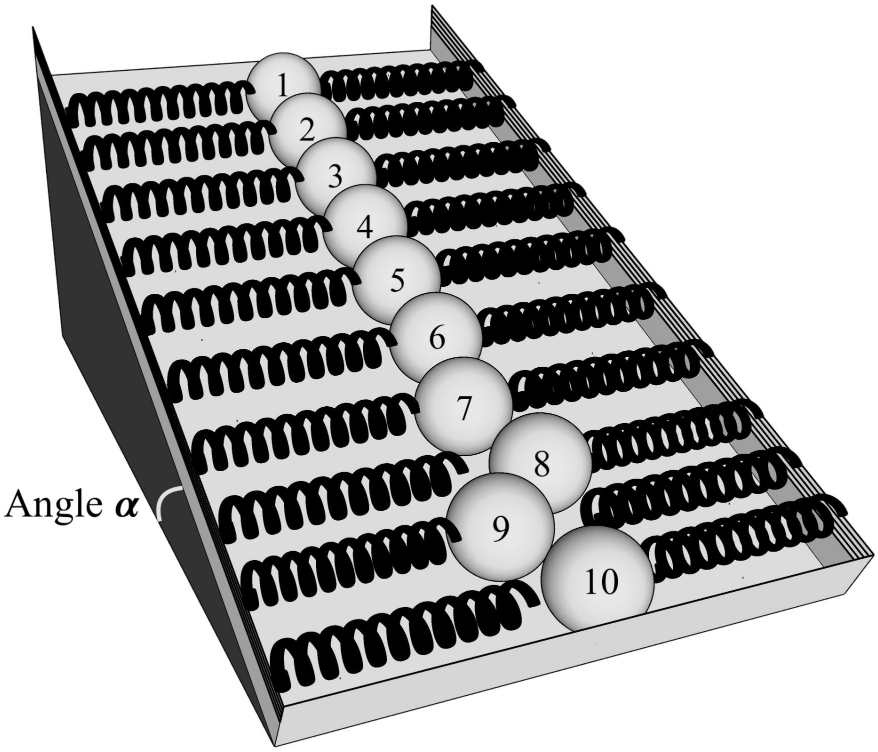

Fig 2.15: Schematic illustration of the model used in this section, i.e. a tilted line of spheres in a harmonic confining potential, with the final sphere (here $N = 10$) in contact with a hard wall. A tilt by an angle α beyond a critical value leads to a buckling of the initially linear chain; transverse sphere displacement results in a harmonic restoring force.

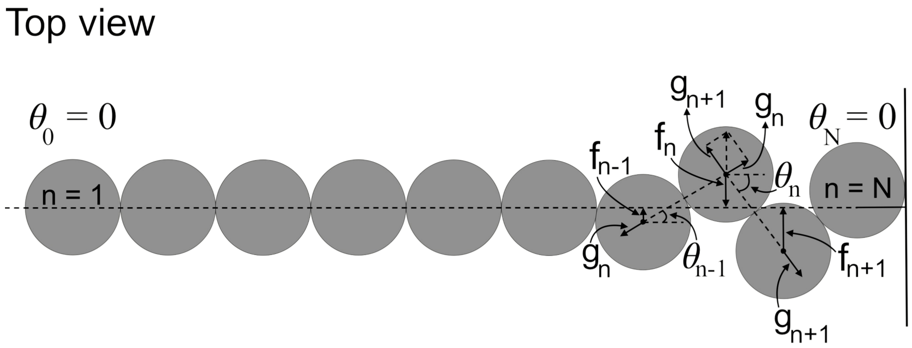

Fig 2.16: Top view of the buckled chain of Fig. 2.15, with the relevant notation of the dimensionless quantities, as defined in the main text. The forces f_n (equivalent to the dimensionless displacements) are due to the confining potential, and g_n are the compressive forces at sphere-sphere contacts). The sphere positions in this example were obtained from computer simulations for the dimensionless tilt, $\tau = 0.03$.

In a chain that is tilted by an angle α with respect to the horizontal, as shown in Fig. 2.16 each sphere of mass m experiences a tilt force $mg \sin \alpha$ along the axial direction. In the following, we introduce the non-dimensional tilt variable τ by $\tau = mg \sin \alpha/(kD)$.

In the case of a finite value for the axial component, τ of the compressive force between contacting spheres depends on the position of a sphere within the chain, according to,

$$G_n \cos \theta_{n-1} = G_0 + \tau(n-1), \tag{2.1}$$

from the condition of force equilibrium. G_0 is the magnitude of the compressive force exerted by the wall on the top sphere, $n = 1$.

The transverse force balance for the displaced nth sphere is expressed as

$$F_n = G_n \sin\theta_{n-1} + G_{n+1} \sin\theta_n = (G_0 + \tau(n-1)) \tan\theta_{n-1} + (G_0 + \tau n) \tan\theta_n. \tag{2.2}$$

and we thus obtain

$$\tan\theta_n = \frac{F_n - (G_0 + \tau(n-1)) \tan\theta_{n-1}}{G_0 + \tau n}. \tag{2.3}$$

The centers of contacting spheres are separated by their diameter. Hence in our dimensionless variables, the radial distances and forces are given by

$$F_n + F_{n+1} = r_n + r_{n+1} = \sin\theta_n. \tag{2.4}$$

Rewritten in terms of $\phi_n = \tan\theta_n$, the two iterative equations are thus

$$\begin{aligned} \phi_n &= \frac{F_n - (G_0 + \tau(n-1))\phi_{n-1}}{G_0 + \tau n} \\ F_{n+1} &= \frac{\phi_n}{\sqrt{1+\phi_n^2}} - F_n \end{aligned} \tag{2.5}$$

The hard wall boundary condition for sphere $n = 1$ requires the first tilt angle θ_0 to be zero, with an arbitrary F_1. Using Eqs. 2.5 we proceed iteratively to (F_{n+1}, ϕ_{n+1}). The angle θ_N corresponds to the contact of the Nth sphere with the wall, which can be made equal to zero.

Compression Δ is defined as

$$\Delta = (ND - L)/D, \tag{2.6}$$

where L is the total chain length. This results in

$$\Delta = N - \sum_{n=1}^{N} \cos\theta_n = N - \sum_{n=1}^{N} (1+\phi_n^2)^{-1/2}. \tag{2.7}$$

The total energy is given by the sum of the energy due to transverse sphere displacement and the energy due to tilt,

$$
\begin{aligned}
E = \frac{1}{2}\sum_{n=1}^{N} F_n^2 + \tau \left(\sum_{n=0}^{N}(n\cos\theta_n) - \frac{N}{2}\right) = \frac{1}{2}\sum_{n=1}^{N} F_n^2 \\
+\tau\left(\sum_{n=0}^{N} \frac{n}{\sqrt{1+\phi_n^2}} - \frac{N}{2}\right),
\end{aligned}
\tag{2.8}
$$

where we have used $\cos\theta_n = (1+\phi_n^2)^{-1/2}$.For the case of a straight chain ($F_n = 0$, $\theta_n = 0$, $\phi_n = 0$) this reduces to

$$
E_{straight} = \tau N^2/2. \tag{2.9}
$$

2.4.1 The non-dimensional tilt variable τ for hard sphere experiments

In our experiments with hard spheres the restoring transverse force is provided by the curvature of the cylinder, see Fig. 2.17. Transverse displacement Y of a sphere of mass m is opposed by a gravitational force $\frac{2Ymg}{D_T-D}[1-4(\frac{Y}{D_T-D})^2]^{\frac{-1}{2}} \simeq (\frac{2Ymg}{D_T-D})(1+2(\frac{Y}{D_T-D})^2)$, where D_T and D are cylinder and sphere diameter, respectively. The maximum displacement is about $\frac{D}{2}$ (doublet structure) and we thus obtain $2(\frac{Y}{D_T-D})^2 \simeq 0.08 \ll 1$.The restoring force is thus approximately linear in displacement Y with a force constant k_p of

$$
k_p = \frac{2mg}{D_T - D}. \tag{2.10}
$$

In a cylinder tilted by an angle α against the horizontal, a sphere exerts a longitudinal force $mgsin\alpha$ on its contacting neighboring (in the direction of tilt) sphere. As in our modeling of the discrete system, we introduce τ as a non-dimensional tilt variable via

$$
\tau = \frac{mg}{k_p} sin\alpha \tag{2.11}
$$

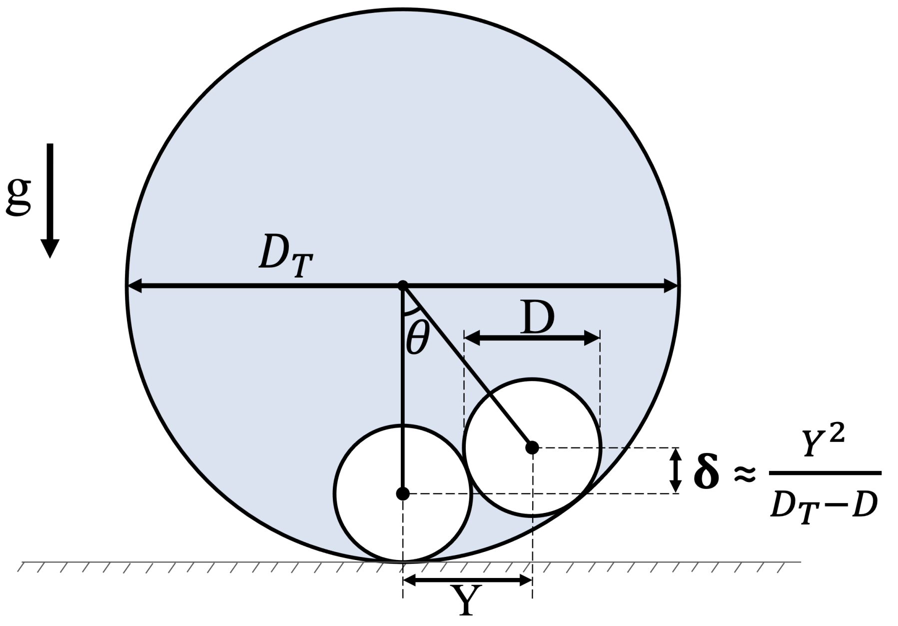

Fig 2.17: Diagram showing the geometry of the hard spheres held against the curved surface of the tube, which can be used to relate the physical dimensions of the system to k_p, the (approximate) spring constant of the confining potential.

In these experiments, the restoring transverse force is provided by the curvature of the cylinder. Inserting for k_p (Eq. 2.10), we obtain the dimensionless tilt variable τ

$$\tau = \frac{1}{2}(\frac{D_T}{D} - 1) sin\alpha \tag{2.12}$$

In conclusion, the stability of the linear chain and the appearance of the buckled configuration in our experimental findings demonstrate the impact of friction in stabilizing structures that would otherwise be unstable. Our findings are similar to previous studies of columnar structures composed of tennis balls, which were found to be stable only due to the presence of friction between the balls [44].

Despite the broad agreement between our experimental results and numerical and theoretical predictions, the influence of friction makes a direct comparison challenging. However, our upcoming experiments with bubbles will be explained in the next Chapter and will provide a more accurate experimental counterpart to our theory.

In summary, this study underscores the importance of considering friction in studying stability in systems with subtle properties. These findings contribute to our understanding of the mechanisms that govern the stability of simple systems and open new avenues for further exploration.

2.5 DIY Science: Hands-on Experiments

2.5.1 Onset of buckling

For a set of equal size hard spheres, the critical tilt angle as a function of N, $\tau(N)$ in which the onset of buckling occurs could be easily investigated as shown in Fig. 2.18.

Accessibility	Cost	Duration
★★☆	💵	⧗

Materials:

✓Twenty hard spheres, i.e. marbles or ball bearings.

✓Perspex cylindrical tube with a different diameter about three times larger than hard sphere's diameter)

✓One stopper to seal one end of the tube

✓A flat surface

✓A ruler or a protractor

To conduct the experiment, begin by sealing one end of a tube with a stopper and placing two marbles inside the tube. Gradually raise one side of the tube in a vertical direction, while the opposite end remains fixed on the table. Initially, the marbles will be arranged linearly, but once a specific angle is reached, known as the critical angle, the chain of marbles will buckle and no longer be arranged linearly. The critical angle can be determined using a

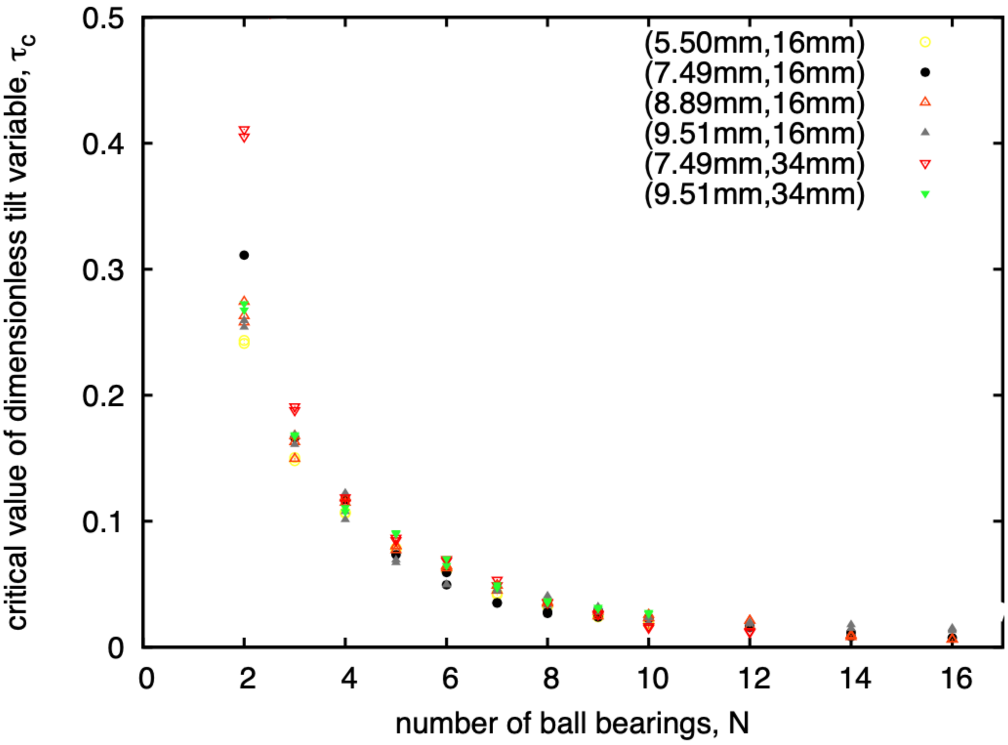

Fig 2.18: Experimental data for the critical value of the dimensionless tilt variable as a function of the number of spheres, N. The experiments were carried out for spheres and cylinders of different sizes. The first number in the key (,) is the sphere diameter, the second is the tube diameter.

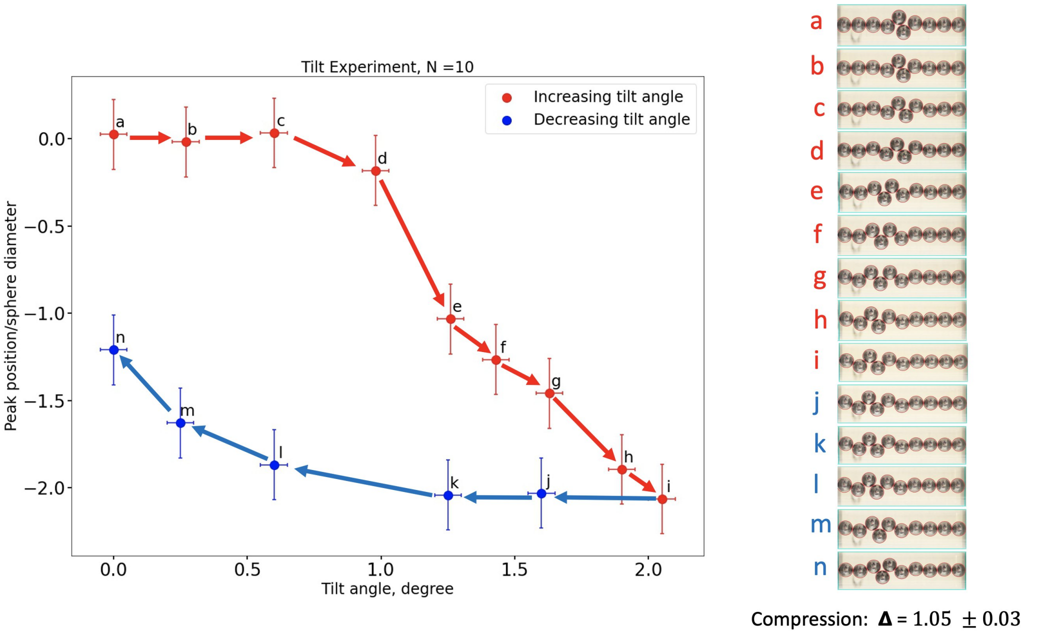

Fig 2.19: A hysteresis loop. A linear chain consisting of ten hard spheres, each with a diameter of 6.30 mm, that are confined within a perspex tube with a diameter of 15.60 mm and are held at a fixed compression. The experiment commences with structure (a), which has a compression of $\Delta = 1.05 \pm 0.03$ at a tilt of $\tau = 0$. The peak position is centered in the middle of the tube. The tilt is gradually increased by small increments while lightly tapping the tube, causing the peak position to move to the sides. Tilt is further increased until the separation of the spheres takes place. The tilt is then reversed in small increments until zero tilt is reached again (Structure (n)).

protractor or, alternatively, by measuring the height of the pipe and its length and using the relevant formula. The experiment should be repeated with increasing numbers of marbles, ranging from three to twenty, with each trial's critical angle recorded. For more accurate results, the experiment should be conducted multiple times, and the average critical angle determined.

2.5.2 Hysteresis

A hysteresis loop can be observed for a linear chain of hard spheres confined in a cylindrical tube (See Fig. 2.19).

Accessibility	Cost	Duration
★★☆	💵	⌛⌛⌛

Materials:

✓Ten hard spheres (Ball bearing) in diameter 6.30mm or similar

✓Perspex cylindrical tube with a diameter of 15.6mm or similar

✓Two stoppers

✓A ruler or a spirit level meter (you can download a mobile app[3])

✓A camera

✓A ruler

To conduct the experiment, begin by placing ten hard spheres into the tube and sealing both ends using stoppers. Push the stoppers further to compress the chain into the structure (a), as depicted in Figure 2.19. Measure the separation length between stoppers using a ruler, then calculate the compression parameter Δ using the method described in the relevant chapter. Place the tube horizontally at a tilt of $\tau = 0$ and capture an image of the entire structure from beneath.

Next, gradually increase the tilt by small increments while gently rolling or tapping the tube. The peak position will move to the sides, and another image of the resulting structure should be taken. Tilt should be increased further until separation occurs between the spheres and the wall, and then gradually reversed in small increments until zero tilt is reached. Images should be captured at regular intervals during this process.

Due to presence of the friction, the hysteresis can be observed by plotting the tilt angle as a function of the peak position. To observe more hysteresis, different initial structures and compressions can be used as starting points for the experiment.

---

[3] $https : //play.google.com/store/apps/details?id = net.androgames.level\&hl = en_I E\&gl = US$

Chapter 3

Buckling Experiments Using Soap Bubbles

> ”**It doesn’t matter how beautiful your theory is, it doesn’t matter how smart you are. If it doesn’t agree with experiment, it’s wrong.**
>
> — **Richard P. Feynman**

In Chapter 2, we discussed the experimentation involving hard spheres where friction is a critical factor. However, to eliminate friction, soft spheres can be utilized, for example, gas bubbles in our study. Despite its malleability, the use of soft spheres eradicates friction completely.

In the current chapter, we present a novel series of simple experiments aimed at demonstrating the non-linear characteristics of a linear sequence of soft spheres when subjected to compression. The experiments serve as a means of illustrating the non-linear properties of this system and provide further insight into the behavior of soft spheres under compression.

3.1 Introduction

For many years, linear chains of particles have been widely employed as a means of demonstrating the principles of classical mechanics through simple examples and analysis. As a result, these chains are frequently studied in classroom settings, with demonstrations designed to explore their properties and behaviors. One such example is the calculation of the force exerted by a falling chain, which provides a useful illustration of the concepts and techniques involved in the study of linear chains of particles [45–47], the physics of collisions and shock waves [48], as well as numerous other interesting problems suitable for the undergraduate physics curriculum [49].

The previous works in this field have mainly centered around the application of linear elastic theory and dynamics to linear chains of particles [50, 51]. This approach provides a useful pedagogical tool due to the simplicity of one-dimensional systems, making them easier to observe, analyze, and theorize. These models share many properties with more complex two and three-dimensional systems and serve as a useful introduction to these.

In this study, we aim to broaden the spectrum of classroom demonstrations by examining the stability of linear chains of mutually repulsive particles. The compression exerted on the chain along its length, similar to being confined in an axial potential in related physical systems, and the radial constraint imposed by a cylindrical symmetrical potential, make it an intriguing and relevant demonstration. Our primary focus is on the static equilibrium of the system under high compression conditions, where complex non-linear phenomena become pronounced.

Our demonstration experiments and the accompanying theoretical analysis and simulations offer a visual representation of the underlying physics and have the potential to stimulate further research and investigation in various fields. The related research already presented in sections 2.1.1, 2.1.2, and 2.1.3. The demonstrations are also a valuable tool for teaching the principles of physics, and they could help students understand the underlying concepts with greater ease.

The arrangement of the bubbles is determined by the interplay of radial and axial confinement forces. At high levels of compression, the bubbles are arranged in a straight linear chain. However, as the radial force decreases, the system transforms from a linear chain to a modulated zigzag structure [52]. This transformation is characterized by a wide range of intriguing properties, such as buckling, localization of the particles (often referred to as "kinks" or "solitons"), the presence of multiple alternative (meta)stable structures, topological changes, bifurcation diagrams, and a Peierls-Nabarro potential that explains transitions between these structures [52, 53].

The study of buckling in linear chains has garnered significant attention in various fields, including materials science and engineering, where it is related to the mechanical properties of materials [54]. It is also relevant to the study of active colloidal chains found in biology [55]. The formation of buckled structures is a common occurrence in cooled ion formations in traps and has numerous advanced applications in areas such as spectroscopy, quantum computing, and reaction kinetics [56].

In the following, we present two series of experimental setups that are both simple and practical in nature, and that serve to showcase and measure the nonlinear properties of a system comprised of mutually repelling particles. The setups are designed to be easily implemented with commonly available equipment in a classroom setting.

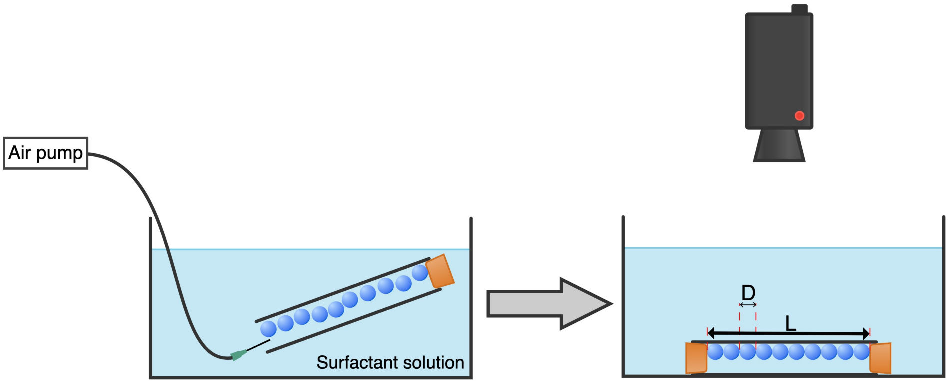

Fig 3.1: The experimental setup involves a horizontal liquid-filled tube with trapped gas bubbles. The tube is filled with bubbles and then tilted to remove any excess bubbles so that only a single line of bubbles remains. A stopper is inserted at one end of the tube to confine the bubbles axially. The other stopper is then inserted and adjusted manually to vary the compression of the bubble chain. The observations are carried out under water to prevent air from entering the tube. The inner diameter of the tube is 6.7 mm, the outer diameter is 8.0 mm, and the uncompressed axial extension of the bubbles is approximately D = 2.3 mm.

3.2 Buckling of a Linear Chain of Soft Spheres, N = 19

Here, we use a simple experimental setup to demonstrate and quantify the buckling properties of 19 air bubbles under compression. The setup is easily assembled with readily accessible materials commonly found in the classroom, such as a test tube, stoppers, an aquarium pump, and dish-washing solution (as shown in Fig. 3.1). The experimental design involves trapping gas bubbles in a horizontal liquid-filled tube, where the bubbles are confined by stoppers at both ends. By compressing the linear chain of bubbles, buckling occurs only at some critical value of deformation. These structures are similar to previous findings in studies of hard spheres in a cylindrical tube which was discussed in Chapter 2.

3.2.1 Experimental Method and Results

The production of bubbles of equal size was achieved by utilizing a flow-controlled air pump to introduce air through a nozzle into a commercial surfactant solution (Fairy Liquid). The resulting bubbles were then deposited into a horizontally-oriented perspex tube (with an inner diameter of 6.7 mm and an outer diameter of 8.0 mm), situated at the bottom of a container filled with a surfactant solution. The placement of stoppers at each end of the tube served to confine the bubbles within. Given a specific separation, L_0, of the stoppers, N bubbles were arranged so as to be in direct contact with one another and the stoppers. This arrangement resulted in an uncompressed axial extension, D, of the bubbles, defined as $D = \frac{L_0}{N}$. In the experiments described herein, 19 bubbles with an uncompressed axial extension of 2.3mm were utilized.

Decreasing the length of confinement L by manually pushing the stoppers, we may observe and record (as photos or videos) the structures that are formed; for example, see Fig. 3.2. For small values of compression Δ, as defined in Eq. 2.6, the chain of bubbles remains straight, with all bubbles suffering equal deformation. However, at some critical value of compression Δ, buckling occurs (see Fig. 3.2). The critical value of Δ is zero for hard spheres and finite for soft (elastic) spheres, as in the case of bubbles.

In the present experimental setup, buckled structures are observed as shown in Figure 3.3.

In order to quantify the buckled structures formed under compression, a method was devised to determine the transverse width of the minimal rectangular bounding box that encompasses all bubbles in a particular chain. This width, represented by the symbol W, was used as a simple and convenient parameter for measurement and was obtained through the use of image processing software (ImageJ) rather than manual measurements from

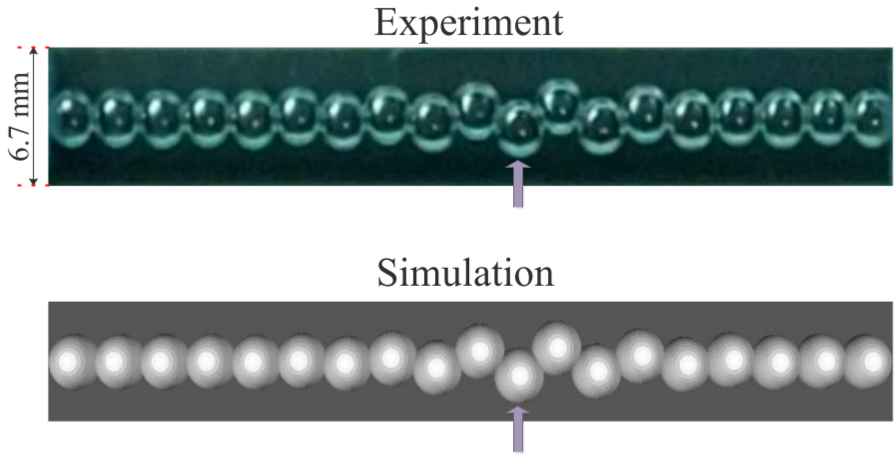

Fig 3.2: The compression of a linear chain of bubbles results in buckling, once a critical value of compression is exceeded. (a) Photograph of 19 gas bubbles in a tube filled with surfactant solution for compression $\Delta = 2.36$ (corresponding to image/datapoint 6 in Figs. 3.3 and 3.4). (b) A computer simulation of 19 soft spheres using the model of Sec. 3.2.2 and the ratio of force constants $k = 2.25$ yields a closely similar structure, cf. the region around the maximally displaced bubble, marked by an arrow.

photographs. An illustration of this method can be seen in Fig. 3.4 (a).

The re-scaled width W/D for ten different levels of compression Δ are displayed in Figure 3.4, which encompasses all the structures depicted in Figure 3.3. The graphical representation indicates a pronounced enhancement in the width once the compression surpasses its critical value.

It is imperative to discuss a particular feature of the experimental setup prior to a thorough examination of the data. In an uncompressed chain of solid spheres ($\Delta = 0$), the width W is equal to the diameter D. Nevertheless, when interpreting the value of W in experiments with bubbles, two crucial factors must be taken into account. The utilization of liquid-filled tubes causes optical distortion, resulting in a minor increase in the ratio W/D, even for solid spheres in these experiments. Additionally, the influence of buoyancy, which presses the gas bubbles against the tube surface, leads to non-spherical shapes, even in the absence of compression ($\Delta = 0$).

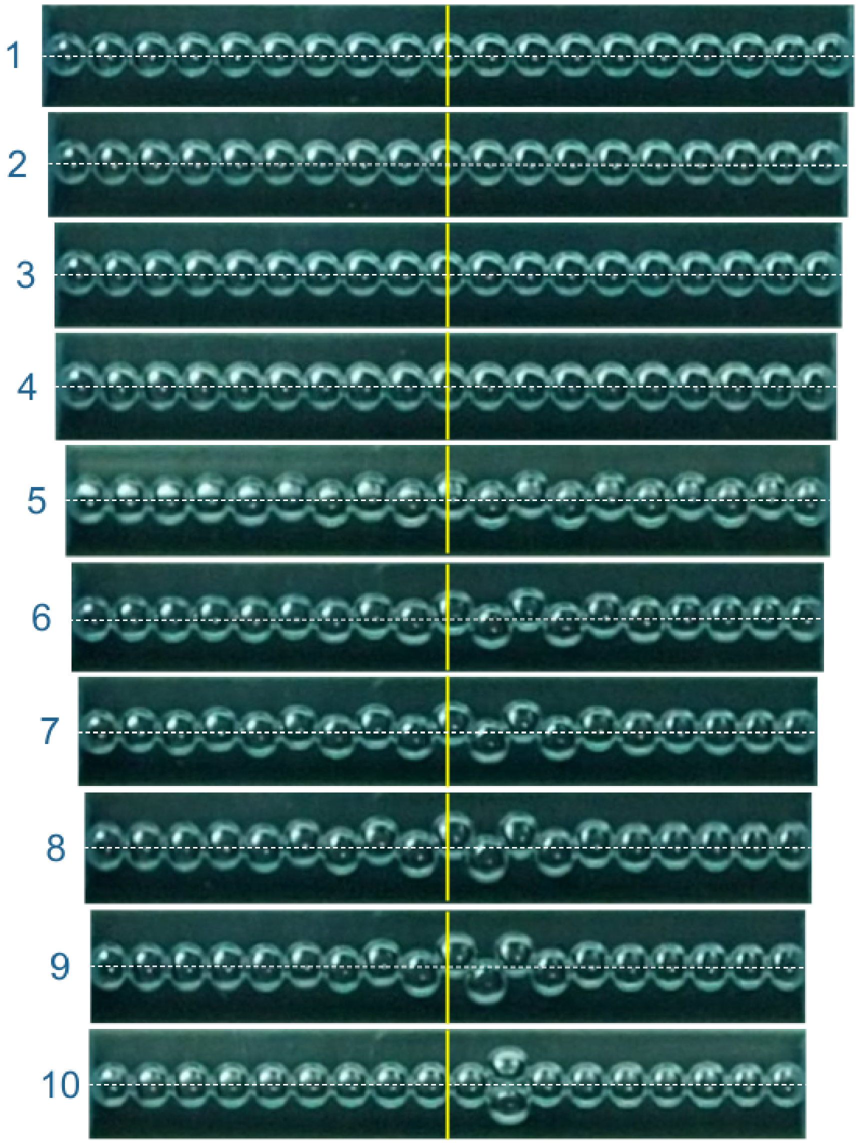

Fig 3.3: Sequence of 10 photographs of a chain of 19 bubbles under compression ($\Delta_i =$ 0.13; 0.32; 1.00; 1.56; 2.13; 2.36; 2.56; 2.62; 2.80; 2.85). For geometrical dimensions, see the text. Compression was progressively increased by small amounts. The solid yellow line marks the center of each chain. Buckling becomes visible in the fifth image, leading to a modulated zigzag pattern of bubble displacement. Note eventual exceptional case 10, in which a transverse pair (or doublet) of bubbles is surrounded by a straight linear chain. Variations of the experimental procedure can produce localization at other places in the chain.

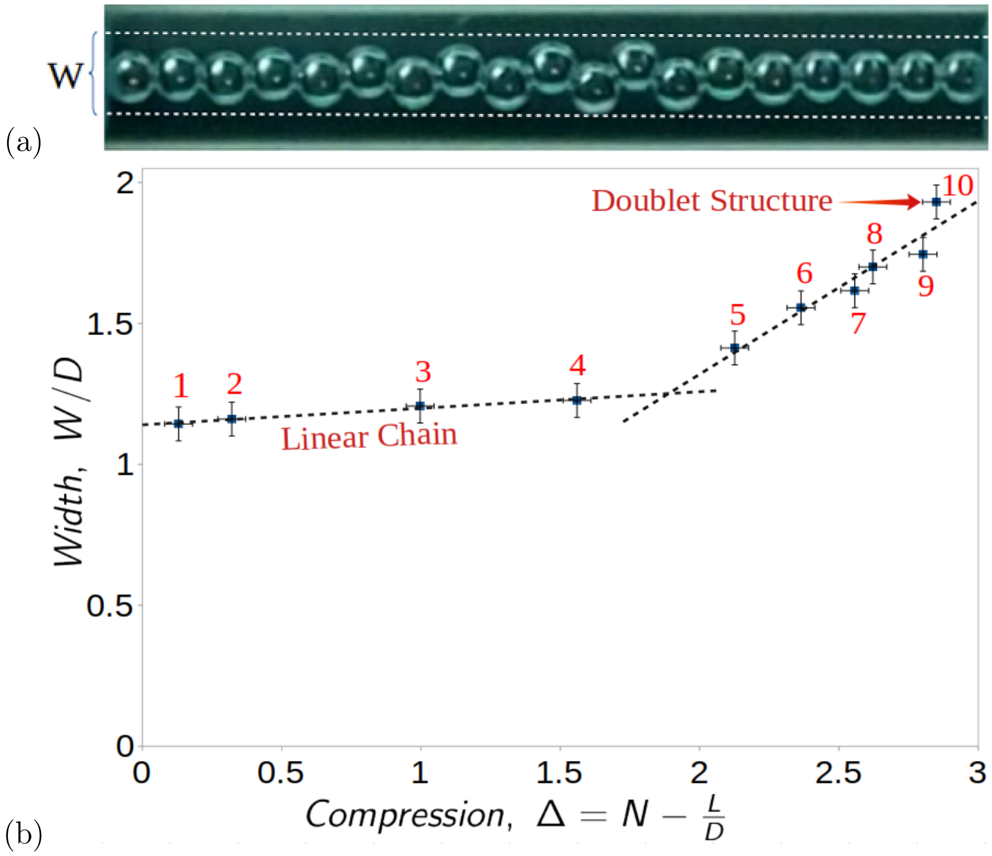

Fig 3.4: The variation of the normalized chain width $\frac{W}{D}$ with compression Δ reveals the onset of buckling at a critical value of $\Delta \simeq 1.9$. Values of Δ exceeding 2.7 lead to the occurrence of an increasing number of doublets within the same structure. (Numbers refer to the chains shown in Fig. 3.3, and the photograph at the top marks the width W for structure 7.).

To furnish additional enlightenment, the data for a chain of solid plastic spheres with a diameter of 3mm, placed in the water-filled tube within the container used for the bubble experiments, was determined to be $W/D \simeq 1.04$. This highlights the occurrence of optical distortion and non-spherical shapes of gas bubbles, even under uncompressed conditions, that must be taken into consideration when analyzing the results.

The observed variation in the re-scaled width W/D as a function of compression Δ is the result of two distinct physical effects, which are evident from the data presented in Fig. 3.4. The use of liquid-filled tubes in the experimental setup leads to optical distortion, causing a slight increase in the ratio W/D even for uncompressed hard spheres, as well as non-spherical shapes for gas bubbles.

For small compression, $\Delta \simeq 0.13$, the combined effects result in a value of $W/D \simeq 1.14$. As compression increases, the width increases slightly to about $W/D \simeq 1.23$ for $\Delta \simeq 1.56$. When compression reaches $\Delta = 2.13$, the chain has undergone buckling, leading to a significant increase in the width to approximately $W/D \simeq 1.41$. As compression continues, the width increases in a roughly linear fashion, with the lateral displacement of the chain becoming increasingly localized.

For compression values exceeding $\Delta \simeq 2.7$, the previously observed zigzag structure transforms into a chain containing a doublet, characterized by a transverse pair of bubbles, as seen in photograph 10 in Fig. 3.3.

In order to determine the compression at which buckling occurs, the variation in width of the buckled structures is extrapolated linearly. This analysis estimates the onset of buckling to be around $\Delta_c \simeq 1.75$. Nevertheless, buckling is typically characterized by a square-root scaling with compression, as evidenced in the simulations described in Section 3.2.2. Taking this characteristic into account, the critical compression value is estimated to lie within the range of $1.8 < \Delta_c < 2.0$, as illustrated in Fig. 3.4.

3.2.2 Theory and Simulations

We have made a preliminary comparison of the above data with the results from an elementary numerical simulation. It is important to note that the simple model for the interactions between bubbles, which will be employed, is not designed to be highly precise and thus the comparison will not be completely quantitative.

The focus of the simulation will be on structures with length L comprised of N idealized spherical particles of diameter D. A visual representation of these structures can be seen in Figure 3.5. The analysis will be limited to structures that are formed under low compression, $\Delta = N - \frac{L}{D}$.

A demonstration of one simulation result has already been presented in Figure 3.2.

In order to generate numerical results, the Durian Model [57, 58] was utilized. This model characterizes bubbles as spheres that exhibit a repulsive force between their centers when in contact. The interaction energy E_i for two bubbles of equal size is expressed as $E_i = \frac{k_1}{2}(\left|\overrightarrow{R_i} - \overrightarrow{R}_{i+1}\right| - D)^2$, where $\overrightarrow{R}_i$ denotes the positions of the sphere centers and k_1 represents the spring constant of the bubble-bubble interaction. Despite its roughness, this model has been considered useful in foam physics [59, 60], offering qualitative and semi-quantitative insight.

In the present case, we write the total energy due to *contacts*, including the contribution of the two bubbles in contact with the confining walls ($i = 1$) and ($i = N$), in the approximate form,

$$E_{contact} = \frac{k_1}{2}[\sum_{i=1}^{N-1}(((X_i - X_{i+1})^2 + (Y_i - X_{i+1})^2)^{\frac{1}{2}} - D)^2 + (\frac{D}{2} - X_1)^2 + (\frac{D}{2} + X_N - L)^2] \tag{3.1}$$

The numerical model considered here only accounts for the X_i and Y_i coordinates, which serves as a planar approximation and is deemed appropriate

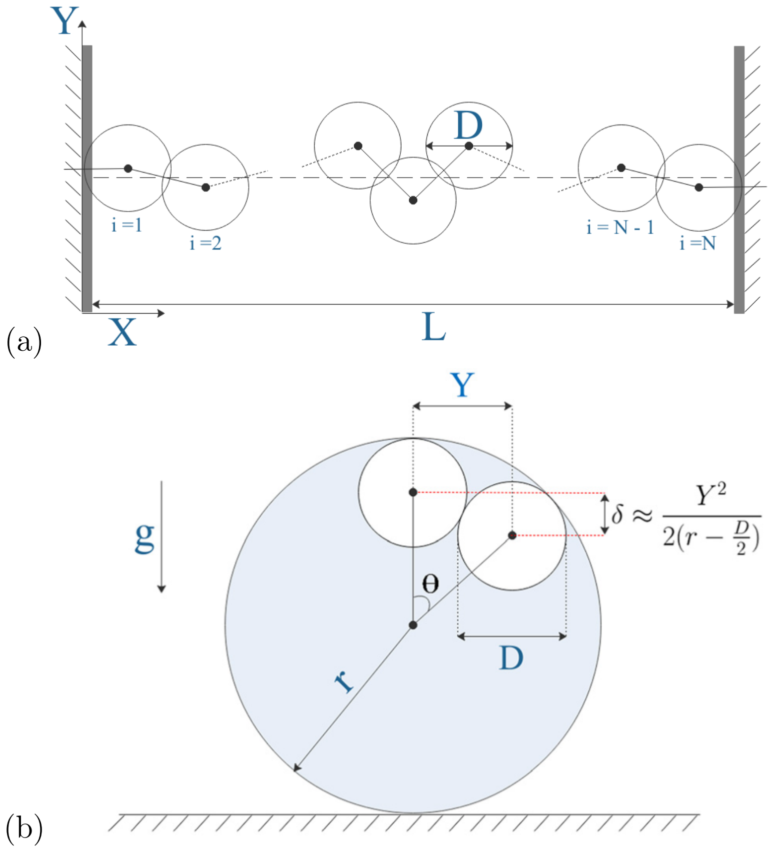

Fig 3.5: Schematics for the modeling of a chain of soft spheres under compression. (a) Top view and notation. (b) View along the X direction, showing bubbles (diameter D) pressed against the surface of a liquid-filled tube (radius r). For small displacements Y of a bubble in the horizontal direction, its downward movement leads to an increase in potential energy due to buoyancy of approximately $\frac{1}{2}\frac{\Delta\rho g V}{(r-D/2))}Y^2$. Here, $\Delta\rho$ is the density difference and V is the volume of the bubble, $V = \frac{4}{3}\pi(\frac{D}{2})^3$.

for situations characterized by low compression.

The corresponding approximation for the gravitational potential energy due to the *buoyancy* of a particle held in place by the cylindrical surface is

$$E_{gravity} = \frac{k_2}{2} \sum_{i=1}^{N} Y_i^2. \tag{3.2}$$

The force constant K_2 is given by

$$k_2 = \Delta\rho g \frac{4}{3} \pi (D/2)^3/(r - D/2),$$

(3.3)

where $\Delta\rho$ is the density difference of gas and liquid, g is the acceleration due to gravity, and r is the radius of the cylinder, see Fig. 3.5(b).

The total energy is thus approximated by $E_{total} = E_{contact} + E_{gravity}$. Expressed as a dimensionless energy, $E = E_{total}/(k_2 D^2)$, this may be written as

$$E(\Delta) = \frac{1}{2} k \sum_{i=0}^{N} (\delta_{i,i+1} - 1)^2 + \frac{1}{2} \sum_{i=1}^{N} y_i^2 \tag{3.4}$$

here we have introduced the dimensionless quantities $x_i = X_i/D$, $y_i = Y_i/D$, $\delta_{i,i+1} = ((x_i - x_{i+1})^2 + (y_i - y_{i+1})^2)^{1/2}$, as early in Sec. 2.4 we already introduced for the hard sphere case,

(for $0 < i < N$), $\delta_{0,1} = \frac{3}{2} - x_1, \delta_{N,N_{N+1}} = \frac{3}{2} + x_n - (N - \Delta)$, and the ratio of the two force constants,

$$k = \frac{k_1}{k_2}. \tag{3.5}$$

This is essentially the same expression used in [54].

The system has been limited to two dimensions, which differs from the other physical systems referred to in Sec. 3.1. In those systems, planar structures occur only at low compression and become twisted at higher compression, whereas in the present study, planar structures are imposed by geometry from the outset.

A linear chain with a small compression value Δ was initially employed. Subsequently, Δ was gradually increased and the previous equilibrium structure was utilized as the starting structure for each minimization step, in concurrence with the experimental methodology. The energy E, as described by Eq. 3.4, was minimized numerically through adjustments to the coordinates X_i and Y_i.

At compression levels below a certain threshold, which is contingent upon the value of the force constant ratio k defined in Eq. 3.5, the minimum energy configuration assumes that of a straight linear chain. However, as compression reaches the critical value, this structure buckles and transforms into a zigzag chain, as observed in the experiment. This instability can be triggered by a slight perturbation.

Mughal *et al.* [1] conducted numerical simulations with increments of $\delta\Delta = 0.01$ until reaching a compression of $\Delta = 3.0$, for various values of k. The results obtained for $k = 2.5$ and $N = 19$ are displayed in Fig. 3.6, depicted by the dimensionless maximum transverse displacement, represented as $y_{max} = \max(|y_i|)$. This parameter was selected for comparison with the experimental results because it is easier to determine and less impacted by optical distortion and bubble deformation, compared to the width W.

For compression values slightly exceeding the critical value $\Delta_c = 1.83$, the maximum transverse displacement, y_{max}, was found to exhibit a variation of $(\Delta - \Delta_c)^{1/2}$, which is a common characteristic of buckling transitions. The displacement profile in this range is characterized by a broad envelope, which has a general cosine form.

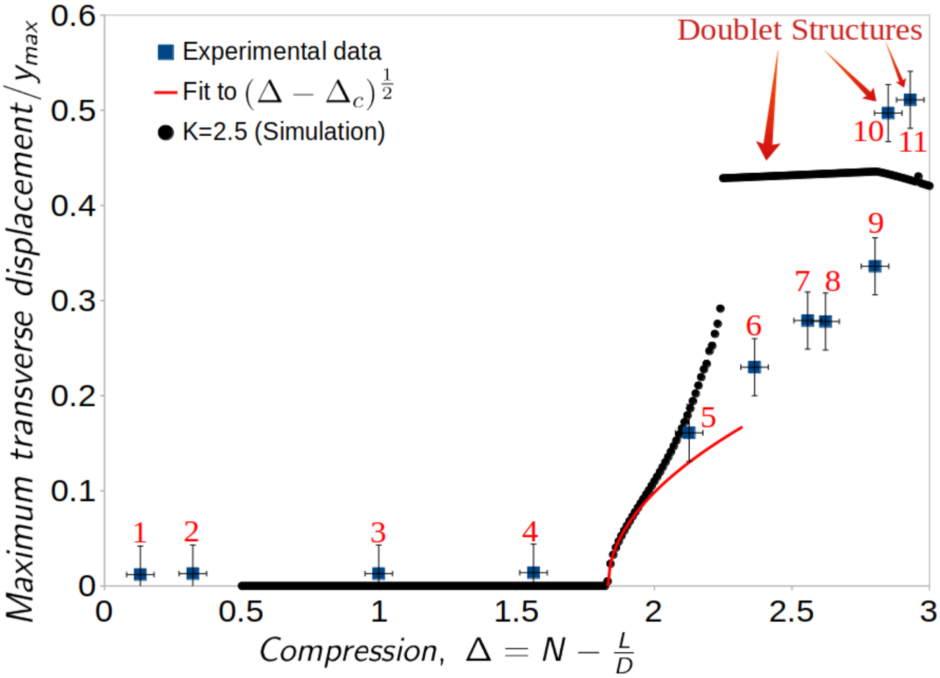

Fig 3.6: Experimental data and results of a model simulation, for the variation of maximum lateral bubble displacement y_{max} with compression Δ. Data points correspond to the experimental data of Fig. 3.4. The solid line represents numerical data obtained from a minimization of the energy of a chain of soft particles, Eq. 3.4, for a value of the force constant ratio $k = 2.5$. At the onset of buckling, the numerical results indicate a square-root dependence of y_{max} with compression (dashed line).

As compression increases, there is a trend towards heightened localization of buckling, as exemplified in Figure 3.2. At a certain level of compression, there is a rapid increase in the maximum transverse displacement. This marks the point where the doublet structure, consisting of two spheres in a transverse configuration, becomes the preferred arrangement. The maximum transverse displacement linked to this structure experiences only a slight rise with further compression before undergoing another transformation.

In Figure 3.6, experimental data is also provided for comparison. The maximum lateral displacement of the bubbles, $y_{max} = Y_{max}/D$, was obtained by identifying the lateral midpoint of each bubble and then determining its distance from the axis of the tube, as depicted in Figure 3.3. It is worth noting that representing the buckling of a bubble chain through its width W, as demonstrated in Figure 3.4, might be more appropriate for educational purposes as it necessitates fewer measurements.

The theoretical results for a specific value of the ratio $k = 2.5$ agree well with experimental observations, as indicated in Figure 3.6. A higher value of k would cause the critical compression Δ_c to decrease, eventually reaching the limit for hard spheres ($k_1 \to \infty$), which has been reported in previous studies [42]. Additionally, the theory correctly predicts the emergence of the doublet structure, as seen in number 10 of Figure 3.4.

Efforts have been made to estimate the value of k using the experimental parameters. The spring constant k_1 can be calculated as $\gamma/2$, where $\gamma \simeq 0.03 N/m$ represents the surface tension of the surfactant solution [58]. By using this value and plugging in the density, diameter, and radius of the bubbles into Equation 3.2.2, the ratio $k = k_1/k_2$ can be determined. The resulting estimate, $k \simeq 0.5$, is of the same magnitude as the value obtained through comparison with numerical data shown in Figure 3.6.

The method of estimating k by determining the spring constant k_1 and utilizing the relevant physical parameters of the bubbles has proven to be effective. By substituting the values of the density, diameter, and radius into Equation 3.2.2, the ratio of $k = k_1/k_2$ can be estimated to be approximately 0.5. This value is in agreement with the one obtained through comparison with numerical data, as demonstrated in Figure 3.6.

3.3 Compression of a Linear Chain of Soft Spheres, N = 1, 2, 3

In 1993, Morse and Witten described a process by which they derive a first-order theory for the deformation of a droplet under low compression. The result of their work is a relationship between an applied force on a bubble which results in the deformation of the bubble [61]. Höhler *et al.* have conducted a review of the original paper by Morse and Witten, as well as much of the subsequent research on the topic [62].

Here, we explain our new experiments, in which we are interested in how the transverse bubble width changes as a function of axial compression. Furthermore, we will show in a two or three-bubble configuration, the buckling of the chain is observed beyond a critical level of compression.

For further exploration, the buckling can be interpreted using Morse and Witten that account for the variation in bubble width due to buoyancy and compression forces.

3.3.1 Experimental Method and Results

In our experiments, we used a small N. i.e., one, two, and three bubbles were created using the same method as already mentioned in Sec. 3.2.1. The bubbles were confined within a horizontally oriented, liquid-filled tube. These bubbles are buoyant and are therefore pressed against the upper surface of the cylinder. The cylinder is sealed at both ends with stoppers, with one of the stoppers serving as a movable piston. Here, the tube that contains bubbles is fully immersed in the container that was filled with the same liquid. A hole was created on the surface of the tube to allow water exchange from the tube and the liquid bath

In contrast with experiments described in Sec. 3.2.1, here, the experiments were executed utilizing surfactant solutions, SDS above the critical micelle concentration (CMC). This concentration is high enough to ensure bubble stability and to neglect the depletion of surfactant by adsorption to the interfaces. The temperature at which the equilibrium surface tension was measured was 24 degrees Celsius, yielding a value of $34.3 \pm 0.1\ mN/m$. The diameter of the tube employed in the experiments was $2r = 15.6 \pm 0.03\ mm$ while the diameter of the bubbles was $D = 3.727\ mm \pm 0.055$. This produced a ratio of the bubble to tube diameter of approximately 0.24. The volume of the bubbles when crystallized in the 2-1-1 structure in a capillary tube of diameter 5.18 mm was used to determine the size of the bubbles.

When confined within the horizontal cylinder the bubbles are compressed against it due to the buoyancy force F_B with $F_B = \rho g \frac{4}{3} \pi R_0^3$. Now, we define a dimensionless Bond number B_0 as

$$B_0 = \Delta\rho g R_0^2/\gamma \tag{3.6}$$

where $\Delta\rho$ is the difference in the density of the liquid and gas. The Bond number for the bubbles in our experiments is thus given by $B_0 = 0.993$. The capillary number λ is defined as

$$\lambda = (\frac{\gamma}{\Delta\rho g})^{1/2} \tag{3.7}$$

resulting in

$$B_0 = (\frac{R_0}{\lambda})^2 \tag{3.8}$$

where R_0 is the radius of an undeformed bubble.

We are measuring the transverse width of one, two, or three bubbles at a range of piston positions, corresponding to different values of compression as computed using Eq. 2.6.

Here, we define the compressive strain ϵ as

$$\epsilon = \frac{\Delta}{N} \tag{3.9}$$

Experiments were carried out with a chain of one, two, and three identical bubbles which initially arrange an undeformed structure at zero compression and are in contact with hard walls. Then by increasing the compression (decreasing the chain length) in small increments, bubbles start buckling and deforming and a photo is captured in each stage from above the tube as described in Sec. 3.2.1. There is no onset of buckling is observed until a critical value. The variation of transverse width as a function of the distance between the two pistons is shown in Fig. 3.7, together with some photographs of the bubble configurations. Using Eq. 3.9 the compressive force for the two and three-bubble systems is 0.21 and 0.18 respectively. Figure 3.8 shows the increase of the transversal chain width as the chain is compressed, where we have divided the length of the chain by the respective number of bubbles in the chain.

In the case of a single bubble, compression results in a gradual widening of its width. This same trend is also observed for two and three-bubble systems, but with a significant difference. In these systems, buckling occurs at a critical value of chain length, causing the bubble centers to deviate from their alignment along the axial direction. As a result, there is a sharp increase in the width of the chain that is being measured.

In Fig. 3.9 we re-plot the data of Fig. 3.8 as a function of compressive strain, Eq. 3.9. These data using the 1, 2, and 3 bubble systems can be used for further exploration and to interpret this data using the Morse-Witten

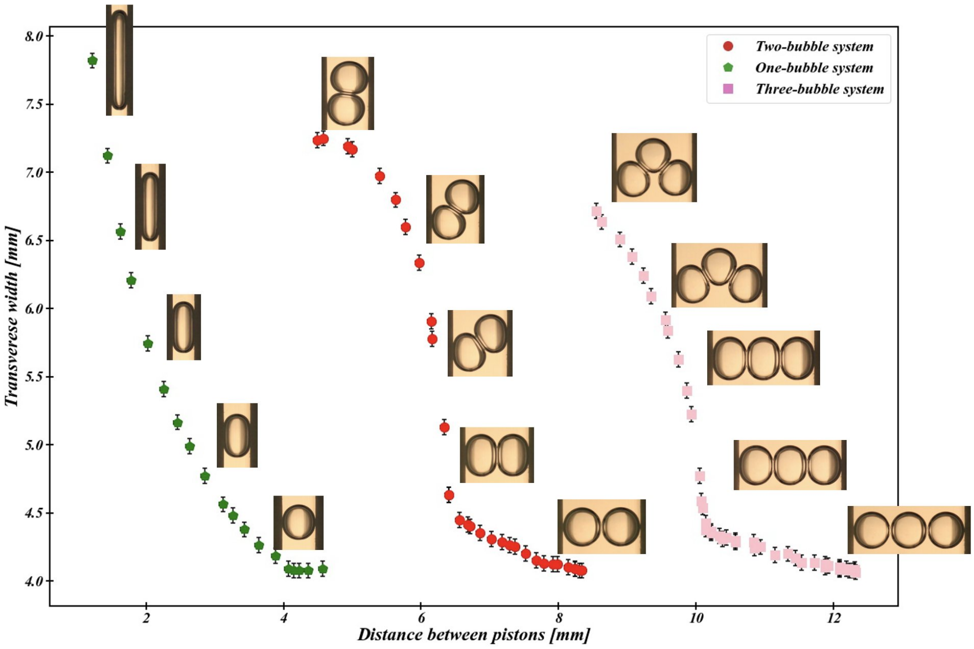

Fig 3.7: Transverse width as a function of the distance between pistons for one, two, and three-bubble system of a diameter of $D = 3.727mm$ is plotted. For two and three-bubble systems, the onset of buckling was observed when the distance between pistons was 6.5mm and 10mm respectively which corresponds to a transverse width of about 4.5.

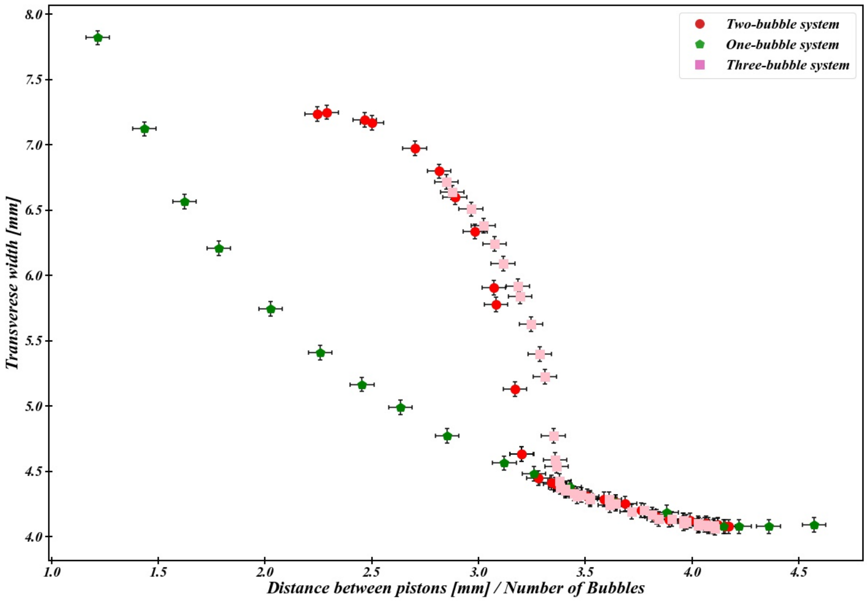

Fig 3.8: Transverse width of systems consisting of 1 bubble, 2 bubbles, and 3 bubbles as a function of the chain length per bubble. In the pre-buckling stage, the variation in width is identical, as all bubble centers are still aligned.

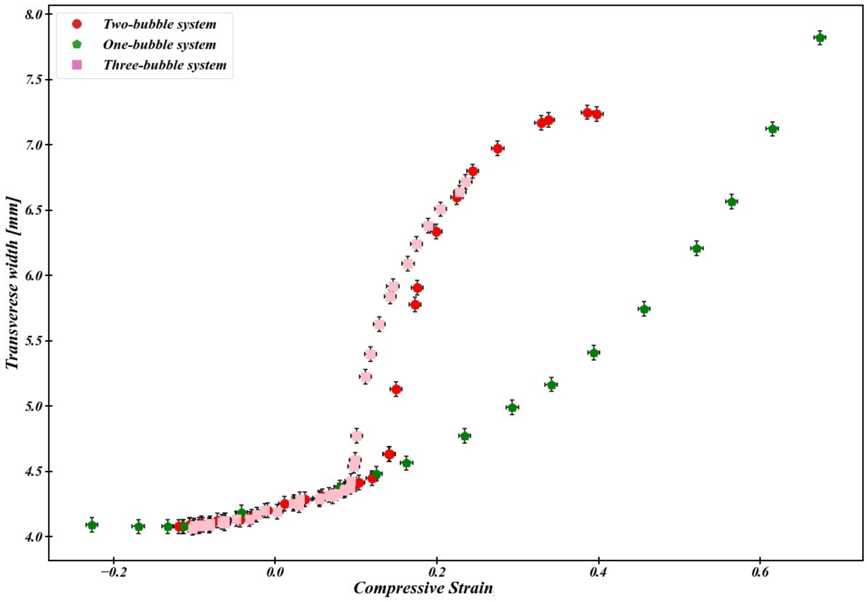

Fig 3.9: Replot of the width data of Fig. 3.8, but now in terms of compressive strain (Eq. 3.9). Data points for negative strain correspond to uncompressed systems where the bubbles were not in contact with each other and the wall.

model as described in the Appendix.B for bubble-bubble interaction.

3.3.2 Conclusion

We have presented two simple experimental set-ups that can be used to study the buckling properties of a chain of soft spheres.

In Section 3.2 we introduced a simple experimental setup to demonstrate 19 soap bubbles under compression. We showed our experimental results are in good agreement with the simulation.

Then in Section 3.3, our experiments using the 1, 2, and 3 bubbles system showed good results and potential for further exploration to study the soft spheres under compression.

In both experiments, one can easily investigate the onset of buckling for

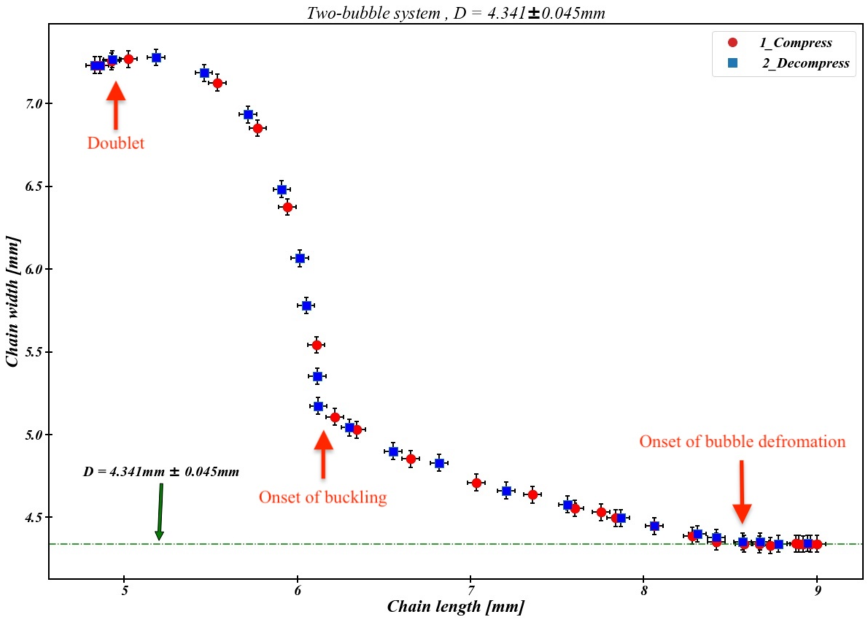

Fig 3.10: The width of a two-bubble system as a function of chain length is plotted, where the diameter of each bubble is 4.341 $mm \pm 0.045$ mm. Starting with an uncompressed chain, then the system is compressed in small increments, and the resulting red circle data is collected. Observations of the onset of deformation, the onset of buckling, and the doublet structure are made. The system is then decompressed, and the resulting blue square data is collected, demonstrating a return to the initial configuration without any observed hysteresis here. Here, the experimental results confirm the Morse-Witten theory.

such a chain of soft spheres.

The experiment described in this chapter incorporates the use of bubbles, which provides an extra aspect for exploration. The softness of the bubbles, which can be controlled through their size, is a key factor.

3.4 DIY Science: Hands-on Experiments

3.4.1 Accurate determination of the diameter of an air bubble

What methods can be employed to obtain precise measurements of the volume of a small air bubble while it is suspended in a liquid? One approach is the simple experiments explained here.

Accessibility	Cost	Duration
★★☆	💵💵	⌛⌛

Materials:

✓A container

✓One liter of water

✓Dish soap (Fairy Liquid)

✓An aquarium pump

✓A needle nozzle

✓Capillary tube (D $\simeq 0.5 - 1cm$)

✓A ruler

✓A camera

First, fill the container with water and add a few droplets of Fairy Liquid to it and slowly stir it until the dish soap is mixed in. A capillary tube with a diameter of D $\simeq 0.5 - 1\ cm$ is partially submerged in the solution.

Air is injected at the tube's submerged end through the needle nozzle which is connected to the aquarium pump. Monodispersity of bubbles is achieved by having constant pressure.

Then, fully filling a capillary tube with monodisperse bubbles, which form a 2-1-1 crystalline structure, should be carried out (refer to Fig 3.11). Then, a photograph should be taken with a ruler fixed adjacent to the tube. The number of bubbles, denoted by N, should be determined by counting them over a known distance, l. Subsequently, the radius of the bubbles can be accurately calculated using the equation $R = \sqrt[3]{\frac{3}{4}\frac{r^2 l}{N}}$, where r refers to the radius of the capillary tube.

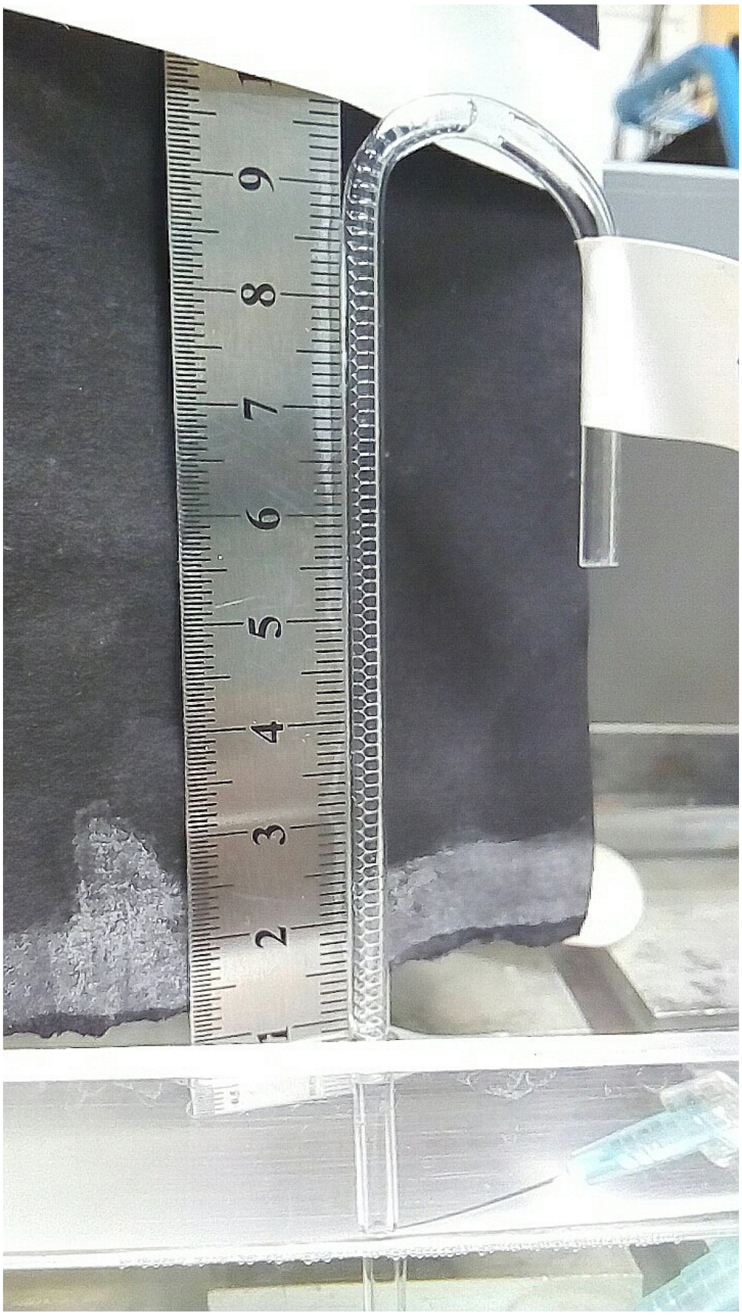

Fig 3.11: A 2-1-1 crystalline structure. A capillary tube with diameter $D = 2.89\ mm \pm 0.03\ mm$ is filled with a monodisperse bubble as described in sec. 5.8. $N = 66$ bubbles are confined in length $l = 44\ mm$, will result the bubble diameter of $D = 1.66\ mm$. Note, the bubbles are monodisperse and there is no variance in the diameter of the bubbles.

Chapter 4

Packing Experiments with Hydrogel Spheres

> ” **The beauty of experimental physics is that you never know where it will lead you.**
>
> — **Robert Hofstadter**

4.1 Introduction

The previous Chapter concerned the buckling of the bubble chain. In the current chapter, first, in Section 4.2 we will start with *"What are hydrogels?"*, then in Section 4.3 we will show how a line of hydrogel spheres lying at the bottom of cylindrical tubes can be hired to represent a zigzag pattern as discussed in Chapter 2 and Chapter 3.

The remainder Chapter will introduce an alternative way of playing with soft spheres by using hydrogels and will show that the hydrogels can be utilized also in different types of packing experiments.

Many different types of packings can be realized experimentally using hydrogel beads, which are readily and cheaply available. The deformability of the swollen hydrogel spheres allows a smooth transition from sphere packings to denser packings. The experiments that we describe here, are easy to set up and thus suitable for use in the class-room or in the undergraduate teaching laboratory.

The packings can generally not be realized instantaneously but might require several hours to form, during which the hydrogel soaks up water. They might thus be set up on one day, left in the classroom overnight, to be studied the following day. This may be accompanied by video imaging to capture the slow dynamics of the packing process.

We will in the following describe five different types of experiments, making contact with current research problems.

Packing experiments do not appear to have yet entered the canon of classroom demonstrations. They can make a good introduction to various concepts in mathematics and physics, including geometrical considerations, minimal surface areas, elasticity, computer simulation, and much more.

4.2 What are hydrogels?

Hydrophilic gels ("hydrogels") are made up of hydrophilic ("water-loving") polymers that are cross-linked in a 3D network which can absorb large amounts of water. They were first reported by Wichterle and Lim (1960) [63] and can be formed from natural or synthetic polymers [64]. Hard in the dry state, they are soft and rubbery after water absorption. Hydrogels may also exhibit volume changes in response to certain physical or chemical stimuli. Physical stimuli include temperature, electric and magnetic fields, solvent composition, light intensity, and pressure. Chemical stimuli include changes of pH value, ionic concentration, and the presence of particular chemical compositions [65, 66]. Most transitions are reversible, thus, once a volume change has occurred and the trigger has been removed, the hydrogels can return to their original state [66]. Here we will not explore the opportunities for further experiments presented by such properties.

Hydrogels are classified according to their structure, which may be amorphous, semi-crystalline, crystalline, or consists of hydrocolloid aggregates. They can be produced in different morphologies: amorphous, thin film, peelable, soft, spherical, stiff, etc [67]. They have many applications, including use in drug delivery, sanitary products, heavy metal ion removal, scaffolds in tissue engineering, contact lenses, pH-sensors, biosensors, injectable hydrogel for spinal cord regeneration, supercapacitor hydrogels, and oil recovery [63, 65, 66, 68–71].

One of the most common uses of (spherical) hydrogels in agriculture is to help plants by retaining moisture in the soil surrounding them. They are thus readily purchased from garden shops, or over the Internet, also from toy shops.

4.3 Buckling of a line of hydrogel spheres in a confining potential

The experiment is related both to an observation concerning plant growth, and our buckling experiments as already discussed in Chapters 2 and 3.

The experiment described below was performed with standard commercial spherical hydrogels with a diameter of 2.10 ± 0.05mm when in the dry state. The colour of these spheres was bright red, but the gradual absorption of water turns them increasingly pink. When immersed in water they eventually turn transparent.

In addition to the hydrogels, an Acrylic hollow cylinder cut in half along its long axis, and two stoppers are required for this experiment.

Here, we have placed 10 hydrogel beads in a horizontally placed trough. This was made from a cylindrical tube that was cut in half longitudinally. Stoppers were fixed at both ends, as shown in Fig. 4.1. Then using a pipette, water from the top of each hydrogel was added; once all the water had been absorbed, the system was photographed and then more water was added. This process is repeated several times. As the spheres grow, they eventually make contact with their neighbors and the stoppers, resulting in the formation of a line of spheres, placed at the bottom of the trough to minimize gravitational energy (at about 4 hours and 10 minutes in our experiment). At some critical time (about 4.5 hrs) the linear chain is no longer stable and gives way to a modulated zigzag structure in which spheres are displaced from the bottom of the trough; the displacement from a straight line is maximal for the spheres in the center. The time between a linear chain being formed and buckling observed was about 25 mins. The buckling of the chain increases as time progresses and we gathered data over the course of 32 hours. In addition, Fig. 4.1 shows the displacement profile for the experimental data and the predicted one from the analytical solution using Eq. 2.5.

The shape of the modulated zig-zag profile which is obtained after the onset of buckling (Figure 4.1(c)) can be interpreted using the theoretical model which we described in Chapters 2 and 3 in which the theory predicts the displacement profile as a function of compression as shown in Fig. 4.1(d).

It is tempting to relate the growth of the hydrogel beads within their cylindrical confinement to the growth of peas in a pod. The straight linear arrangement of a row of peas in an oblong pod was already commented on by Kepler [73], who contrasted it with the arrangements of pomegranate seeds, which are tightly pressed together from all sides, resulting in polyhedral-like seed shapes.

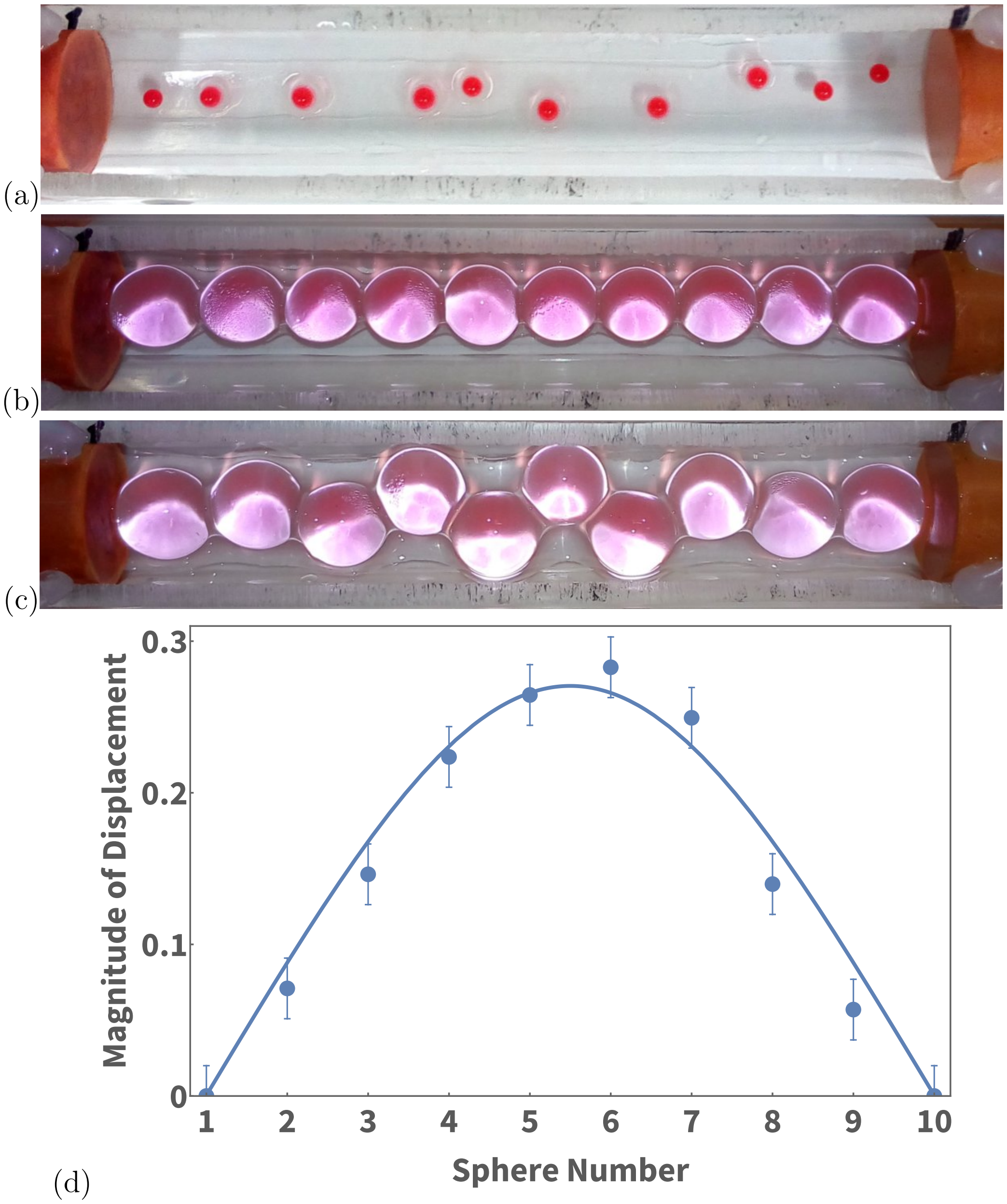

Fig 4.1: Ten hydrogel spheres lying at the bottom of a horizontal trough in which the distance between the stoppers: is 84.4 *mm* (a). Upon the addition of liquid they grow, come into contact, and form a straight linear chain (b). Eventually, upon further swelling of the spheres, the chain buckles to form a modulated zig-zag structure (c). The corresponding displacement profile as discussed in Chapter 2, Eq. 2.5, is plotted for the structure (c) together with the theoretical result (for the same compression), which involves a Jacobi function which is an analytical solution and contains two free parameters, i.e. the number of spheres and compression [72]. In our experiment, D is the average sphere diameter with a value of 9.3mm ±0.2 and the distance between stoppers is 84.4 *mm* which corresponds to a compression value, Δ, of 0.93 (d).

Fig 4.2: Photograph of a zig-zag arrangement of peas in a pod (Photo by Rachel Gorjestani, Pixabay gc10209902_1920. (license is here: $https://pixabay.com/service/terms/$))

Generally the row of peas is straight, essentially. However, this is not always the case, as is evident when looking at a number of carefully opened-up pods, or simply browsing the Internet, where even X-ray images of unopened pods can be found. The peas can display a zigzag arrangement as shown in Figure 4.2, very much reminiscent to the modulated zig-zag structure displayed by the swollen hydrogel beads shown in Figure 4.1. The biological example is more complicated as both peas and the confining pod grow, but not necessarily at the same rate. We are reminded of Johannes Kepler's comments regarding pomegranates, "for it is not from its formal properties that it induces its shape in this fruit, but it is insisted by material necessity" (translation into English from [73]).

4.4 Hydrogels in packing experiments

The study of the dense packing of objects has a rich and fascinating history [18, 74]. Often Kepler's description of the stacking of spheres in crystalline layers is cited as one of the earliest descriptions of a packing problem. The proof of Kepler's claim from 1611 that an arrangement in which each sphere is in contact with twelve neighbours is the densest possible sphere packing (filling around 74% of space), was achieved only in 1998 by Thomas Hales [75]. This was experimentally difficult for dense packing spheres as friction plays a role and causes the gaps between spheres which leads to empty space.

Deformable spheres have also been the subject of longstanding debate. In 1727 the Reverend Stephen Hales reported the arrangement of peas contained in a pot, compressed using different weights [76, 77]. This resulted in dense polyhedral packings, described by him as "pretty regular Dodecahedrons", i.e. cells with 12 faces. Such packings are not dissimilar to those found in the arrangement of many biological cells. Indeed, a particular shape of cells, i.e. *scutoids* as explained in Section 1.3.2 have since also been found in experiments using soap bubbles that are packed between two concentric cylinders as already shown in Fig. 1.8.

D'Arcy Wentworth Thompson's book "On Growth and Form", first published in 1917 and substantially extended by the author in 1942 [78], remains a classic in the area of geometric and physical principles of biology. It dedicates a full chapter to packing problems ("The forms of tissues"), with many examples taken from the arrangements of soap bubbles. Also discussed in detail is the 1887 conjecture of Lord Kelvin (then Sir William Thomson) to the effect that the cell type which partitions space with a minimum of surface area is that of the 14-sided tetrakaidecahedron [79, 80]. Based on computer simulations, Weaire and Phelan presented an alternative arrangement of bubbles with a slightly lower surface energy [23] in 1994. As already shown in Fig. 1.5 of Section 1.3, Its elegant form inspired the design of the Water Cube for the Beijing Olympics.

Packings of hard (undeformable) objects continue to offer surprises. Experiments by Bernal in 1959 established that the densest *disordered* packing of equal spheres has a packing fraction of about 64%, significantly lower than that of the ordered Kepler packing [81]. In 2004 an experimental study of the packing of ellipsoidally shaped M&M candies showed that their packing density is about 72%, with even 74% possible, depending on the aspect ratio of the ellipsoid [82]. The situation is similar in two dimensions, where ellipses within a certain range of aspect ratios pack closer than spheres [83].

Nowadays, computer simulations are at the forefront of research into packing problems, such as packing spheres into cylinders [84], or the packing of non-spherical objects, such as sphero-cylinders [85], or so-called superellipsoids which allow for a continuous mathematical representation of objects ranging from spheres to cuboids to platelets [86]. Simulation results can then be compared with experimental packing data obtained using X-ray tomography, for example for spheres [87, 88], ellipsoids [89], or foams [90, 91].

4.5 Materials and equipment for demonstration experiments

The following experiments were carried out using hydrogels as described in Section 4.3.

In addition to the hydrogels the following equipment is required for the individual experiments.

Experiment 1: Petri dish, water (beaker), pipette, ruler, camera (mobile phone), white sheet of paper to be placed underneath the Petri dish for contrast.

Experiment 2: in addition to the above: flat container with hexagonal boundary: this can be produced by gluing together six (microscopy) glass slides of equal length with a glue gun.

Experiment 3: acrylic or glass cylinders (in our experiments the inner diameter is 16 mm), stoppers, pipette/syringe needle.

Experiment 4: acrylic cylinder with stopper and piston, two watch glasses, concentric cylinders, adhesive tape.

4.5.1 Experiment 1: Controlled swelling of hydrogels

The growth of hydrogel beads is readily observed upon placing them into a pool of water. However, in the experiments described in the following we proceeded by adding controlled amounts of water in small increments to the beads using a pipette. Only after full absorption of all liquid did we add a further increment. This procedure has the advantage that at any stage we can decide to stop the growth and experiment with beads of a certain size.

Figure 4.3(a) shows a single hydrogel bead (diameter 2.10 ± 0.05mm) placed in a Petri dish. A few drops of water (about three times the size of the bead volume) are added to the bead, using a pipette. As the liquid is gradually absorbed the hydrogel begins to swell. Once all added water is absorbed, further drops of are added, resulting in a further growth of the bead. After some transient time, the hydrogel develops a spherical shape [92], see Figure 4.3(b,c).

This procedure is repeated, until eventually the bead is no longer able to absorb any more water, resulting in a sphere diameter of about 11.95 ± 0.05mm in our experiments, i.e. a roughly six-fold increase of the initial dry bead.

4.5.2 Experiment 2: Two-dimensional packings within circular and hexagonal boundaries

Having demonstrated the growth of a single hydrogel bead, we will now monitor how a large number of these arrange themselves when left to grow in a two-dimensional layer, in a circular Petri dish. Upon coming into contact with

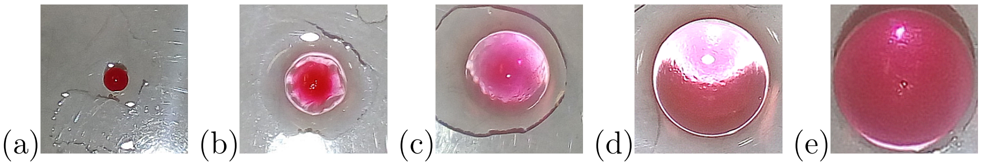

Fig 4.3: Controlled growth of a hydrogel sphere as achieved by adding water droplets in small increments onto an individual hydrogel bead. (a) Photo of the initially dry bead (diameter $d = 2.10 \pm 0.05$mm). (b) The addition of water has led to some swelling, but not all of this water has yet been absorbed after 13 minutes. The shape of the bead is not yet spherical. (c) The hydrogel after 67 minutes. The addition of further water led to more growth. (d) Photo taken after 318 minutes, showing the bead at a stage when all the water that was provided so far was absorbed. (e) Photo taken after 600 minutes. The bead has reached its maximum size (diameter $d = 11.95 \pm 0.05$mm).

each other they self-organise into a mainly triangular pattern.

100 hydrogel beads were placed in a Petri dish with a flat bottom (diameter 86.02 ± 0.03 mm) and observed over the course of thirty hours. Water was added by a pipette intermittently on occasions when the hydrogels had soaked up all previous water. Figure 4.4 shows how over the first two hours an increasing fraction of the Petri dish is covered by the hydrogel beads. The establishment of a triangular lattice is very evident after about 120 minutes, and after about 150 minutes the entire surface is covered by beads which still appear circular when viewed from the top.

As the beads continue to grow, some of them are pushed upwards to lie on top of the existing layer. (In Figure 4.4 we have specified the number of beads that lie in the bottom and in the top layer for each of the photos shown.) These beads were removed using a syringe to obtain a better view of the completion of the layer in contact with the bottom of the Petri dish.

The formation of a hexagonal arrangement is well known from studies of a single layer of soap bubbles of equal size, floating on a bath of soap solution. Indeed, this observation dates back to the experiments of the Nobel Laureate Lawrence Bragg and his research student John Nye in 1947. They introduced

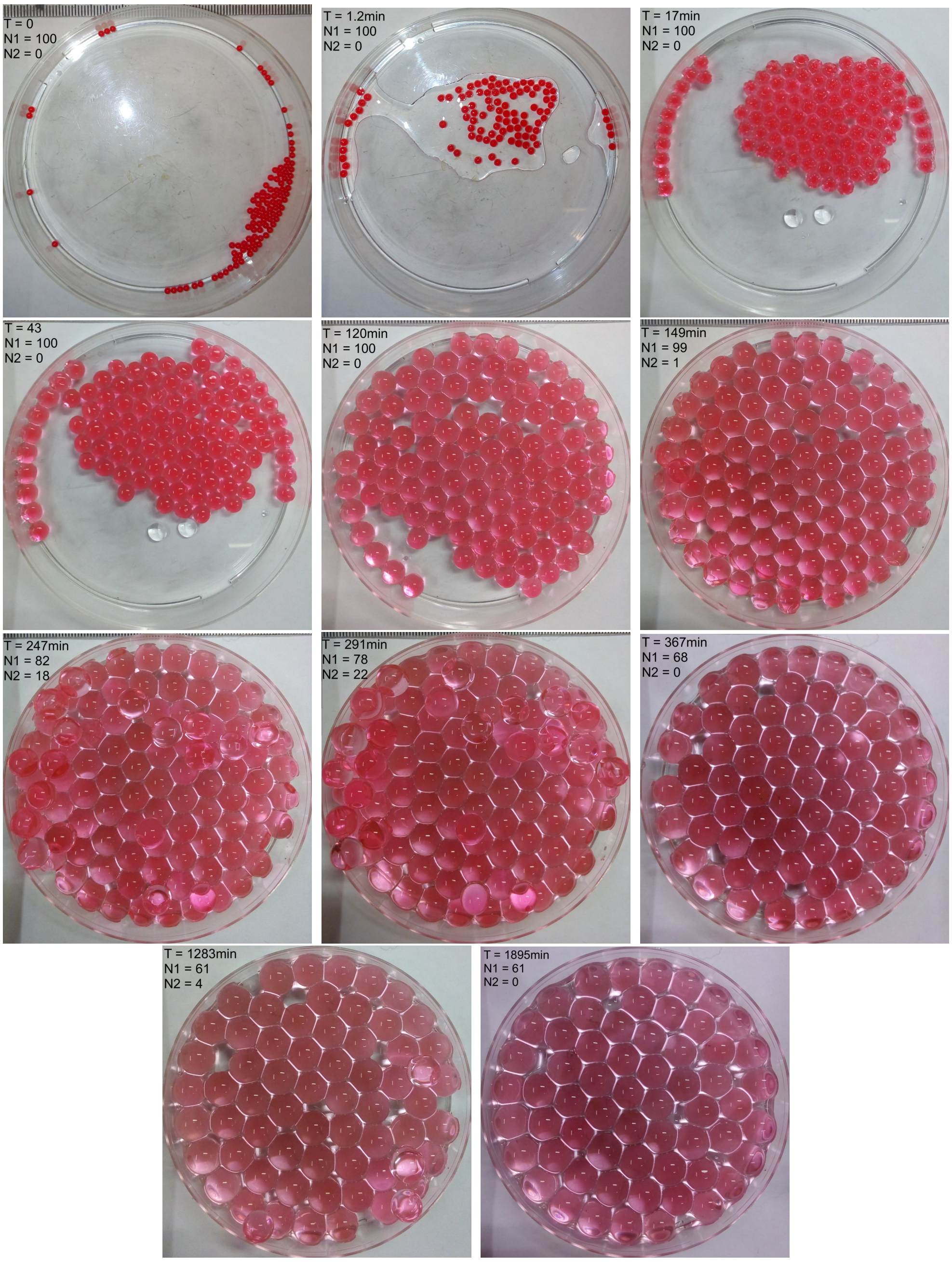

Fig 4.4: Photographs showing the growth of initially 100 hydrogel beads in a Petri dish. After about 30 hours all hydrogels beads had reached their maximum size. Over the course of the growth some of the beads are ejected out of the formed layer to lie at the top of it. These were removed, but are still visible in some of the snapshots shown. (In each photograph we indicate the number of hydrogel beads in the formed layer, N_1, and the number N_2 of ejected beads lying above it.) At the end of the experiment 61 spheres remained in the monolayer.

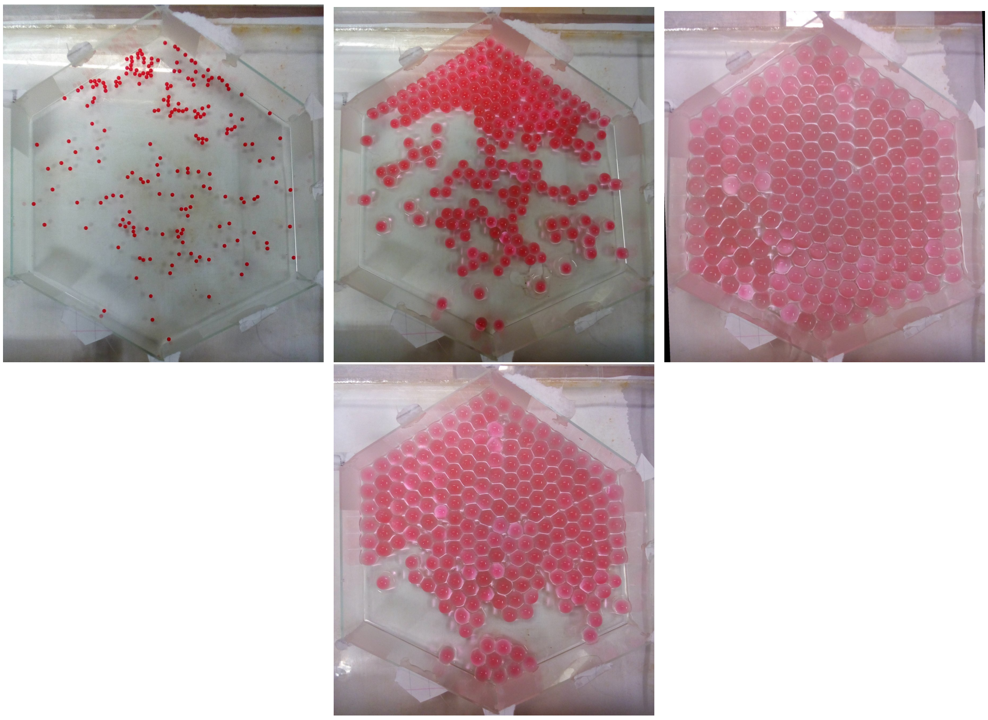

Fig 4.5: Clockwise from top left: 200 hydrogels were placed in a Petri dish of hexagonal circumference and oberved to grow over the course of four hours. This resulting hexagonal arrangement of the spheres features a number of defects.

the bubble raft as a model for the crystal structure of metals [18, 93]. Since the circular container wall is not consistent with hexagonal arrangements, it introduces defects. These may take the form of dislocations, vacancies or grain boundaries. Bragg's experiment was intended to illustrate features such as these, which were being studied in the bulk packings of metal atoms at the time.

To avoid these and thus possibly create a single crystal we constructed a hexagonal confinement using glass slides as side walls (side length 75.68 ± 0.03 mm). 200 hydrogel beads were placed inside the hexagon and were grown in the same manner as the hydrogels in the Petri dish.

As seen in Figure 4.5 the hydrogels readily form a hexagonal packing. In comparison to the arrangement in the circular confinement, fewer vacancies have occurred and the spheres align well along the straight walls.

The two-dimensional packing fraction (or packing density), ϕ, is defined as the fraction of the area filled by the packed objects. In the case of an infinite plane filled with equal-area circles, the densest packing is a triangular arrangement of the circles. Its packing fraction is given by $\phi_{tri} = \pi/(2\sqrt{3}) \simeq 0.907$.

Packings in confinement are less dense, with their packing fraction depending both on the number of packed circles and the geometry of their confinement. Comprehensive catalogs of computer-generated packings of circles confined by a circular or a hexagonal boundary are provided by [94]. For 99 circles within a circle (as in our experiment) the densest packing has a packing fraction of $\phi = 0.813$. The value reported by [94] for 200 circles within a hexagonal boundary (as in our experiments) corresponds to $\phi = 0.871$.

When the 99 spheres in our circular Petri dish came into contact (one had been ejected earlier on) to cover the entire surface, their diameter was about $d = 7.4$ mm (Figure 4.4). For the diameter $D = 86.02$ mm of the Petri dish we thus obtain for the packing fraction ϕ

$$\phi = \frac{N(d/2)^2\pi}{(D/2)^2\pi} = N(d/D)^2 \simeq 0.73. \tag{4.1}$$

For the packing obtained for the 200 beads in hexagonal confinement (side length $a = 75.68 \pm 0.03$ mm) we obtain a packing fraction at the point in time when all beads have come into contact (at a bead diameter of $d = 8.7mm$) of

$$\phi = \frac{N(d/2)^2\pi}{3\sqrt{3}a^2/2} = \frac{N\pi}{6\sqrt{3}}(d/a)^2 \simeq 0.80. \tag{4.2}$$

Both these values are about 10% lower than those for the computed maximal packing fractions mentioned above [94]. Expanding spheres might encounter dissipation due to sphere-sphere and sphere-container contacts. This would limit their movement and thus their ability to fill space most efficiently. In other words, expanding spheres allow for the formation of packing where the beads take on the polygonal-like shape and prevent movement of the other spheres to fill the space efficiently.

4.5.3 Experiment 3: Columnar sphere packings in a cylinder

In the following, we describe the arrangement of equal size spheres in a cylinder, also called *columnar* packings.

There is an extensive background of computational studies of these packings whose details depend on the ratio D/d of cylinder diameter D to sphere diameter d [84, 95, 96]. For $D/d = 1$ the spheres can only sit on top of each other in a straight chain while in the range $1 \leq D/d \leq 1.866$ the densest arrangement is that of a zigzag structure, with each sphere in contact with two neighbouring spheres and the cylinder wall. Forty different structures have been identified for $D/d \leq 2.873$; all structures beyond $D/d = 2.7379$ contain internal spheres which are not in contact with the cylinder wall [84]. Even at $D/d \simeq 4$ the packing fraction is below 0.61, thus much lower than Kepler's (fcc/hcp) bulk value of 0.74.

Hydrogel beads may also be used to demonstrate columnar packings and how these depend on the size of the beads, for a fixed cylinder size. We proceeded by placing dry beads into cylindrical perspex tubes and then added some water to let them expand. Once all water is absorbed we repeated the process until the desired sphere size is obtained.

Figure 4.6 shows two examples of columnar structures which were obtained by this simple procedure. The sphere arrangements are labelled using a notation borrowed from the field of phyllotaxis, which describes the arrangements of leaves along a stem [97]. In the "zig-zag" structure on the left in Figure 4.6 each sphere (apart from the ones at the two ends of the cylinder) is in contact with two other spheres [84].

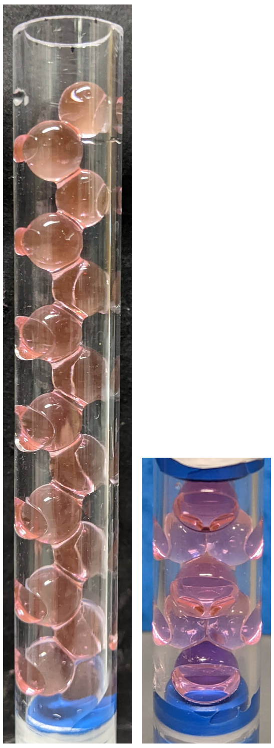

Fig 4.6: Placing hydrogel beads into cylinders and gradually wetting them results in their growth into a columnar ordered structure. The type of structure is determined by the ratio of cylinder diameter D to sphere diameter d. Left: zig-zag structure, $D/d \simeq 1.9$. Right: (2,2,0) structure, $D/d \simeq 2$. Here, the spheres at the top and the bottom of the tube are still spherical and only the contact area between the spheres at the bottom of the tube is higher than the ones on the top due to the mass of the hydrogels.

Unlike hard spheres, such as ball bearings, hydrogel spheres are deformable and will thus suffer some deviations from sphericity due to the weight of spheres placed above them. This has the effect that the distance between the centres of neighbouring spheres decreases with distance away from the open top of the cylinder, as is clearly visible in the zig-zag structure shown in Figure 4.6.

In the structure on the right of Figure 4.6, called (2,2,0) in the phyllotactic notation, each sphere (apart from the ones at bottom and top) contacts five other spheres.

While the flat stopper at the bottom of the cylinder is compatible with the (2,2,0) arrangement, it is incompatible with the zig-zag structure (see Figure 4.6), resulting in some local disturbance of the structure. Such an effect can be avoided in computer simulations, where so-called twisted boundary conditions allows for the realisation of crystalline arrangements without any defects [84].

Figure 4.7 illustrates the growth of 17 hydrogel beads (and consequently a steady reduction of the ration D/d) which leads to a sequence of at least three well-identified columnar crystals. The 17 dry beads were initially placed at the bottom of the cylinder and small amounts of water was added at somewhat *ad-hoc* chosen time-intervals.

After about 165 minutes the growth of the beads has led to the formation of the columnar structure which is labelled (3,2,1). After about 200 minutes the (2,2,0) structure (already shown in Figure 4.6) has formed. Figure 4.7(e) features a (3,2,1) structure only in the upper part of the cylinder. The final photo shows the (2,1,1) which the spheres have taken on after about 25 hours.

It is difficult to determine a value for the sphere-diameter from these photographs. Our rough estimates for the ratio of cylinder to sphere diameter are around $D/d = 2.16$ for the (3,2,1) structure of Figure 4.7(c) and around 2.0 for structures shown in (d)-(f).

We note that throughout this growth sequence no external perturbation of

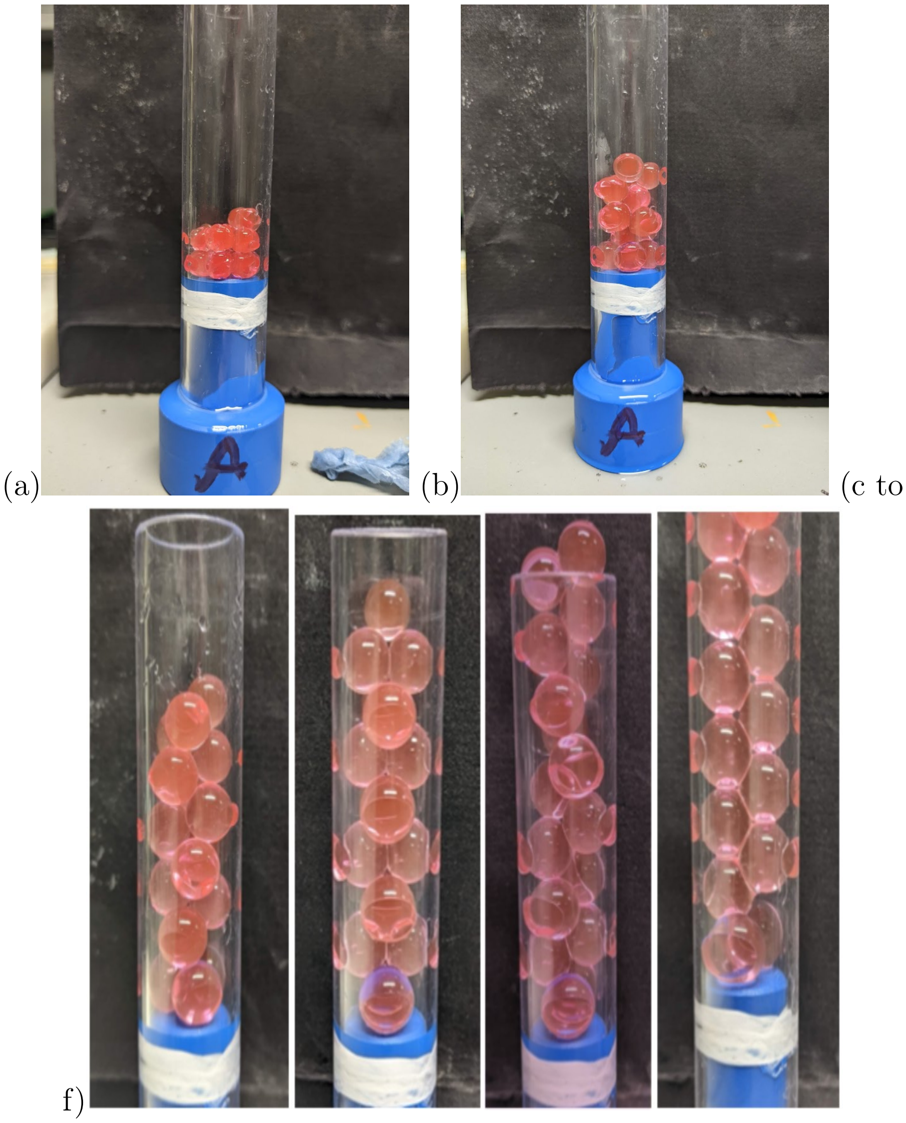

Fig 4.7: The gradual wetting of 17 hydrogel beads which are contained in a vertically placed cylinder results in the growth of ordered columnar structures. (a) Wetted beads after 28 minutes; (b) growth after 59 minutes; (c) 2hrs 45 mins: (3,2,1); (d) 3 hrs 18 mins: 2,2,0 structure; (e) 3 hrs 52 mins: intermediary structure containing sections of 3,2,1; (f) 25 hrs 48 mins: (2,1,1) structure with two hydrogels at the base.

the spheres took place. The formation of the various structures, in response to the sphere growth due to the addition of liquid, is entirely self-organised.

Such a self-organisation into ordered arrangements can also be observed in nature: the huddling together by flocks of penguins, packing densely to mitigate the cold of winter, is a good example [98].

4.5.4 Experiment 4: Packings under external compression

We have also applied compressional force to the type of columnar crystal reported in the previous section. This was achieved by inserting a piston into the open upper end of the cylinder. Pressing down on the piston results in deformations of the hydrogel spheres, eventually leading to the establishment of further contacts or rearrangements. The observed transitions can be compared to those studied in computer simulations of packings of soft spheres, in which spheres are allowed to overlap under compression as discussed in Chapter 3.

In our experiments, we added beads, one by one, into a cylindrical tube which was vertically placed and sealed at the bottom using a stopper. The beads were grown outside the cylinder, using the procedure described above, i.e. via an incremental increase of their water content. Once the tube is filled, a movable stopper (piston) is inserted on the top.

Photographs were taken for different values of compression. Figure 4.8 shows a columnar structure formed by 16 beads at four different values of compression ϵ, defined as $\epsilon = 1 - L/L_0$, where L_0 is the length of the uncompressed and L that of the compressed column.

The initial structure, at compression $\epsilon = 0$, displays the zig-zag structure. However, it is noticeable that hydrogels closer to the bottom of the cylinder are closer together than the ones further up the cylinder. This is a consequence of

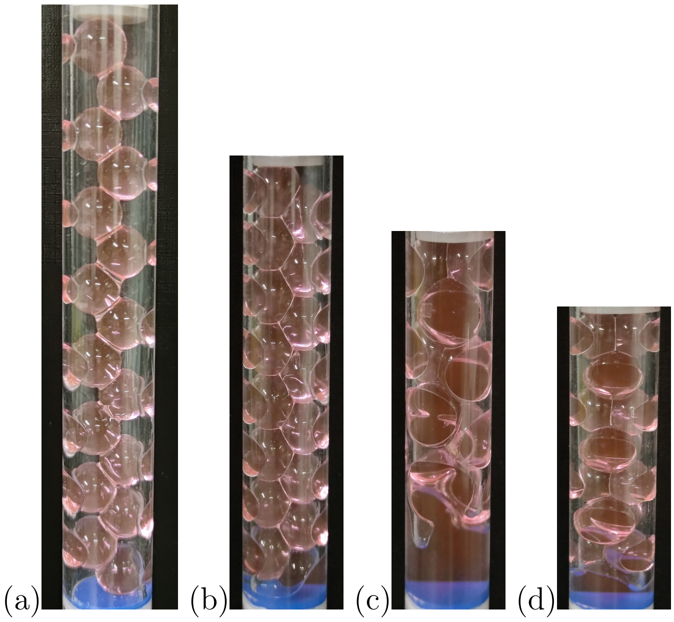

Fig 4.8: Sequence of structural changes, induced by pushing down a piston into a cylinder filled with 16 hydrogel spheres. (a) Zig-zag structure, ($L_0 = 135mm$, compression $\epsilon = 0$). (b) (2,1,1) ($L = 87mm$, compression $\epsilon = 0.36$). (c) twisted zig-zag structure ($L = 79mm$, compression $\epsilon = 0.41$). (d) (2,2,0) (towards the upper section of the cylinder only) ($L = 66mm$, compression $\epsilon = 0.49$).

the softness of the hydrogels, which results in deformation due to the weight of the spheres above them in the column. Downward movement of the piston results in the formation of additional sphere contacts, leading to the (2,1,1) structure displayed in Figure 4.8, at compression $\epsilon = 0.36$. Further compression results in the so called twisted zig-zag structure, shown in Figure 4.8(c) at compression $\epsilon = 0.41$. Finally, at the even higher compression $\epsilon = 0.49$, we can see that the upper part of the cylinder displays yet another structure, called (2,2,0). This sequence of structural transitions was also seen in the computer simulations by [99].

We also produced dense packings by manually pushing pre-wetted hydrogel beads into the space between two concentric cylinders, or between two watch-glasses which were sealed around the rim so that the beads could not escape

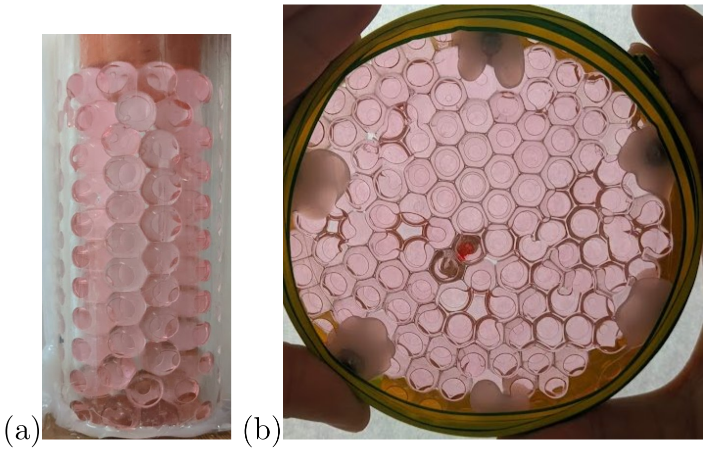

Fig 4.9: High density packings of hydrogels obtained by pushing hydrogel spheres into the spacing between two concentric cylinders (a), and between two watch-glasses (b). In both cases the result is a foam-like or cellular structure.

when compressed. Figure 4.9 shows that this allows for the formation of packings where the beads take on polygonal-like shapes. This is reminiscent of the shapes of bubbles in a foam with low liquid volume fraction or of cells in biological tissue.

4.6 Summary and suggestions for further experiments

We have shown that hydrogels lend themselves to a variety of class-room experiments related to the packing of equal-volume spheres. In contrast to hard spheres, which are of course also suitable for the study of packings, hydrogels can absorb water and grow, and they are soft. The first feature allows for amusing and fascinating observations of structure formation due to growth, not dissimilar to what is observed in biological tissue. The softness enables the formation also of polyhedral packings, as achieved via the confinement of the growing spheres into a fixed space.

Hydrogels thus prove to be an ideal way to explore cellular structures in experiment, to complement the highly sophisticated computational studies performed on high-performance computers.

The presented list of experiments should only be seen to provide stimulation for further explorations. It would for example be of interest to run the growth experiment of Figure 4.7 for longer times (and longer cylinders) to observe additional structural transitions. Since the hydrogels are deformed by the weight of hydrogels placed above them, using longer cylinders would lead to the occurrence of a range of structures along the cylinder. To mitigate against the gravity induced vertical compression of the packings one could in the end, i.e. once the spheres have grown to their maximum size, add a density matched-liquid. This should result in a re-organization into a uniform structure throughout the cylinder.

Further variations of the presented experiments could involve the use of tubes with square or triangular cross-sections (see [100] for foams), or the growth of hydrogels between curved walls, with relevance to curved epithelia tissue material as mentioned in Section 1.3.2.

Playing with hydrogels can provide motivation and amusement. One may well add to the growing literature of packing [18] by exploring their special properties.

4.7 DIY Science: Hands-on Experiments

4.7.1 Swelling of a hydrogel

Swelling is a classical topic in soft matter. In experiment 4.5.2, we presented a controlled swelling of hydrogels where a small amount of water was added to the single hydrogel in short and various increments. One could easily investigate hydrogel growth by placing an individual hydrogel into a pool of water to find the time evolution of the swelling of a single hydrogel (See Fig. 4.10).

Accessibility	Cost	Duration
★★☆	💵	⌛⌛⌛

Materials:

✓A hydrogel (can purchase from toy shops [1])
✓A small container
✓1 L water
✓A ruler
✓A camera
✓A stopwatch (you can use an online stopwatch)

To record the hydrogel size as a function of time, it is suggested to fill a container with water and immerse a hydrogel into it. Capturing images at predetermined intervals while keeping track of the time is crucial. Placing a ruler beside the container would be beneficial in determining the hydrogel diameter from the collected images.

Upon image acquisition, the diameter of the hydrogel can be determined. Conducting the experiment multiple times (at least three times) is advised to obtain an average hydrogel diameter.

After obtaining the hydrogel diameter as a function of time, plotting the diameter against time. Normalizing the hydrogel diameter using its initial diameter (as a dry bead) is suggested for better visualization.

---

[1] https://www.smythstoys.com/ie/en-ie/toys/arts-crafts-and-music/arts/orbeez/orbeez-challenge-meez/p/197694

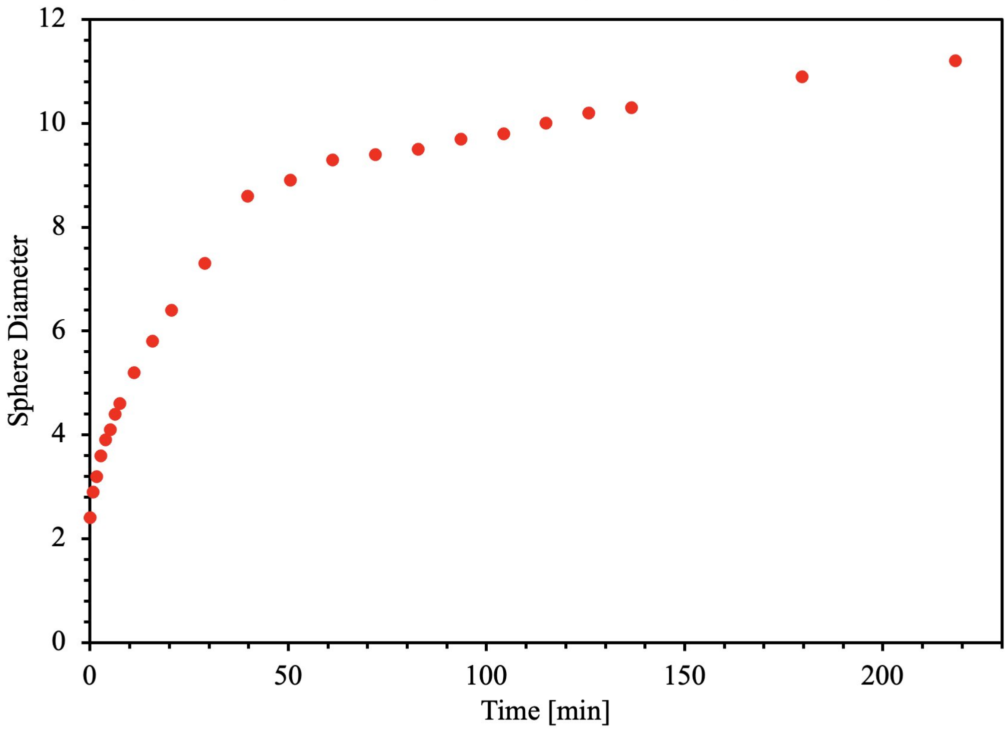

Fig 4.10: Time evolution of the swelling of a single hydrogel. A single dry hydrogel with $D = 2.1mm \pm 0.05$ in diameter was immersed in a container that was filled with one liter of Millipore Water. Due to the optical distortion, the initial hydrogel diameter is greater than D, i.e. $2.4mm$. The variation of the hydrogel diameter as a function of time is plotted. Initially, it grows faster, then at about $t = 60min$ levels off.

Chapter 5

Understanding Mortality Curves Using Thin Liquid Films

> ” **Physics is not a discipline, it’s a way of life.**
>
> — **Richard Feynman**

In Chapter 3 we presented extensive results for the buckling of a chain of soap bubbles under compression when confined in a cylindrical tube. This extended the results for the hard sphere experiments, presented in Chapter 2, to a simple example of deformable soft spheres (A further example of the soft sphere were the hydrogels, used in Chapter 4.1). Bubbles are a relatively easy system to experiment with, and we had referred to classroom experiments already in Section 1.3.

In the current Chapter we will leave behind the study of buckling, but instead present another field of research, where bubbles, or in previous experiments of individual thin soap films offer themselves as a suitable experimental demonstration system.

We will in the following explore how such films can be used to obtain experimental data related to studies of reliability and mortality.

This is follow-up research already done by our former group members. First, in 2009, Tobin *et. al.* presented data for the lifetime distribution of over 2500 soap films (contained in 150 Perspex tubes) made from commercial dish-washing solution (Fairy Liquid) gathered during a public exhibition in Dublin's Science Gallery [101]. The visitors were invited to create 10-20 parallel soap films (with 1-2cm spacing between films) in tubes sealed at both ends. Then the tubes were placed vertically. Every day, the total number of films that remained in every tube was manually counted. The histogram of the bubble lifetime is well described by a Weibull distribution, which indicated that the failure rate is not constant and increases over time.

It was followed by recent research in 2018, Haffner *et. al.* initially showed a fit of survival function, $S(t)$ to Gompertz distribution is superior to the fit of Weibull distribution to the data presented by Tobin [101, 102]. Then prepared their new data set, in which they measured the lifetime of parallel sets of over 2200 soap films made of SDS surfactant solution contained in the Perspex tube. Soap film systems offer an interesting way to explore mortality or failure since they can be introduced in a controlled and systematic manner.

Here, we introduce controlled experiments using *individual* soap films as a simplified physical system to model the complex phenomena of mortality and failure. These experiments provide a controlled and reproducible environment to observe and analyze the processes of ageing and failure. Through examining lifetime statistics, we aim to gain valuable insights into the underlying dynamics of these processes and contribute to advancing our understanding in this field.

The controlled experiments utilizing thin liquid films as a simple physical system also provide a tangible and accessible way to demonstrate complex concepts in a classroom setting. The survival analysis and statistical analysis carried out in this study offer students a hands-on approach to exploring the mechanisms of mortality and failure, while also demonstrating the application of statistical methods in real-world problems.

5.1 Introduction to Concepts of Mortality/Failure

Reliability theory is a general theory of systems failure developed by mathematicians. The theory was published in Russian by Leonid A. Gavrilov and Natalia S. Gavrilova in 1986, and in English as The *Biology of Life Span: A Quantitative Approach* in 1991 [103]. In reliability theory, the lifespan of systems, both biological and artificial, are divided into three main phases. These phases form the so-called ‘bathtub curve [104, 105].

Figure 5.1 shows bath-tub curves for human population and technical devices, respectively. First, the *infant mortality* or *burn-in* phase is a decreasing failure rate where the congenital defects in species or manufacturing defects in technical systems can cause items to fail, known as early failures. This is followed by a *normal life* phase or *working* phase where the failure rate is low and roughly constant, known as random failures. Finally comes the *ageing* phase, or *wear-out* phase, known as wear-out failures, in which the failure rate increases until eventually all species/devices in the sample have failed [106, 107].

5.1.1 Life Table

A life table also known as a mortality table or actuarial table, is a demographic tool used to assess various aspects of a community, including its health level, as well as in the insurance industry. It is based on the population of a gener-

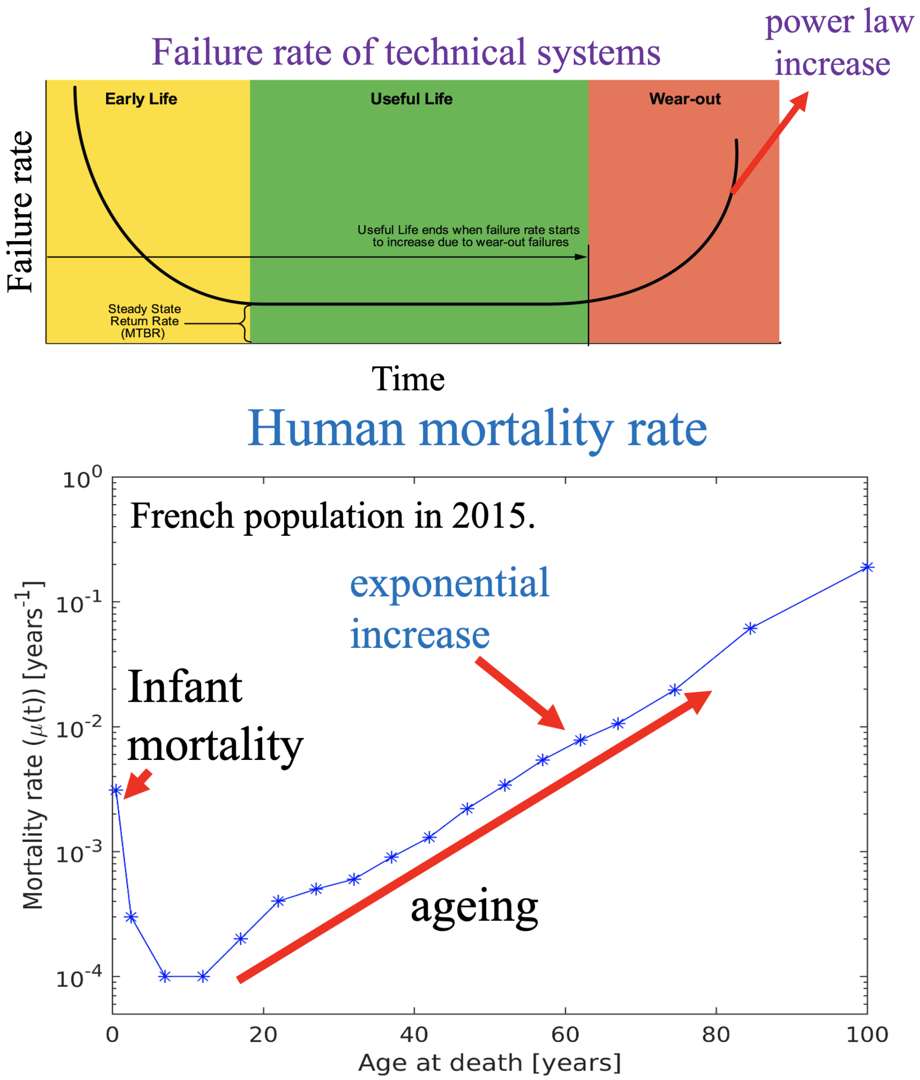

Fig 5.1: Bath-tub curve. Up: The so-called bathtub curve for technical devices where usually fail according to the Weibull (power) law [1]. Down: Bathtub curve for human mortality as seen in the French population in 2015 has the same shape as the curve for failure rates of many machines but they die according to the Gompertz (exponential) law (raw data source: https://www.insee.fr/en/statistiques/6039964).

ation, typically consisting of 100,000 or 1,000,000 individuals, and uses data on death rates and probabilities in each age group to determine the survival of individuals within that population.

Age interval	**% Surviving**
0-6	1.00
7-16	0.64
17-26	0.40
27-36	0.25
37-46	0.16
47-56	0.10
57-66	0.60
67-76	0.30
77-86	0.01

Table 5.1: John Graunt (1620-1674) was the first person who established the science of demography and created the first life table which shows the probability of surviving as a function of age[108]

The life table is also used to calculate life expectancy, which represents the expected number of years an individual will live, specifically life expectancy at birth for a newborn. In 2022, Hong Kong had the highest life expectancy in the world (85.29 years), while the life expectancy in the Republic of Ireland was lower (82.81 years), according to the latest data from the United Nations Population Division [2]. Life expectancy is generally higher for women and in developed countries with a high level of health [109].

Insurance companies use life tables to evaluate the risk of death for premium calculation, while governments use them to forecast future requirements for education and health services. Table 5.1 shows an example life table dating

---

[2] Data based on the latest United Nations Population Division

back to the 17th century, which was created by John Graunt, the founder of demography.

The aim of reliability theory is to model the lifespan distribution of systems using mathematical models.

The study of lifetime statistics features a range of subject areas, such as biology, engineering, demography, epidemiology, or actuarial science. Although the underlying mathematical concepts are shared, the use of different terminologies can lead to confusion. We will for this reason briefly introduce the key concepts here, which will be used throughout the chapter.

Given a population of size N, which could be made up of humans, light bulbs, animals, soap films, technical systems, etc., we wish to describe its evolution as a function of time t. Reliability is described by the *reliability function* $S(t)$ (also called *survival function*) which is the relative number of individuals that are surviving up to time t. $S(t)$ is defined as:

$$S(t) = \frac{N(t)}{N(0)} \tag{5.1}$$

where $N(t)$ is the number of members in the population that is still alive/intact at time t. The function $S(t)$ decreases with time from its initial value $S(0) = 1$, to 0, when all members have *died*. The *failure function* $f(t)$ is defined as its complement, $f(t) = 1 - S(t)$.

The failure function may also be introduced via a *failure density function* $f_T(t)$ as

$$f(t) = \int_0^t f_T(t)dt \tag{5.2}$$

Here, the $f_T(t)dt$ is the probability of failure in the time interval $[t, t + dt]$. Writing the reliability function $S(t)$ as $S(t) = 1 - \int_0^t f_T(t)dt$, we obtain:

$$f_T(t) = -\frac{dS(t)}{dt} \tag{5.3}$$

We shall use this relation when discussing defective systems in our soap film data.

As explained above, there is another function known as **force of mortality**, $\mu(t)$ (the mortality rate, hazard rate, or failure rate) which is used to describe ageing and failure. The force of mortality is the number of deaths (either in general or due to a specific cause) in a population per unit of time. Usually expressed as the number of deaths per 1000 individuals per year, in mathematical terms it is the negative time derivative of the logarithm of the survival function, S(t) [4]:

$$\mu(t) = -\frac{1}{S(t)}\frac{dS(t)}{dt} = -\frac{d}{dt}\ln[S(t)] \tag{5.4}$$

where the negative sign guarantees that $\mu(t)$ is always positive. Also, Eq.5.4 means $\mu(t) = \frac{f_T(t)}{S(t)}$. For short times, when $S(t) \approx 1$, one thus obtains $\mu(t) \approx f_T(t)$.

In demography, $\mu(t)$ in the Eq. 5.4 is called *mortality rate* while in some other text books which consider technical devices, rather than $\mu(t)$, $\lambda(t)$ is used and the function is called *failure rate* (or *hazard rate*, $h(t)$).

In ecology, graphs using a logarithmic scale for $S(t)$ as a function of (linear) time are called *survivorship curves*. A straight line in such a graph (i.e., $\mu(t) = const.$) is referred to as type II survivorship curve. An accelerating decay of $\log S(t)$ (i.e., $\mu(t)$ increases with time) defines type I, and a decelerating decay (i.e., $\mu(t)$ decreases with time) type III survivorship [110].

5.2 Mathematical Models for Variation of the Mortality Rate with Time

Can humans become immortal and live forever? The answer is "NO" so far, and ageing is still inevitable in humans. Moreover, ageing, disease, and injury are three main reasons of human mortality [111]. However, life extension seems to be more achievable in the near future and is of interest in various areas such as life insurance, pensions, health policy, medical research, and insight into the characteristics of the disease. In the following, we will focus on ageing, mortality and the laws governing these. An early pioneer in this field was *Benjamin Gompertz*.

5.2.1 Gompertz Law of Mortality

Benjamin Gompertz was born in London in 1779 to a family of successful diamond merchants. However, being Jewish, he could not attend university and instead taught himself mathematics by reading works of prominent mathematicians such as Isaac Newton and Colin Maclaurin.

Gompertz became a member of the Mathematical Society of Spitalfields and served as its President when it merged with the Astronomical Society. He was highly regarded in the mathematical community and was elected a Fellow of the Royal Society in 1819. In 1832, he became a member of the council of the Royal Society.

In addition to his mathematical achievements, Gompertz was also active in the insurance industry. He was appointed as actuary to the Alliance Assurance Company, founded by his brother-in-law Nathan Mayer Rothschild. In this role, he acted as a government advisor and assisted the Army Medical Board with his calculations. One of his notable contributions to the field was his *law of human mortality*, later expressed as the Gompertz function. This function reduced a large amount of data in life tables into a single equation and showed that human death rates double every eight years as an adult [107].

For an ageing system (for example see Fig. 5.1), the mortality rate is high at the beginning (known as infant mortality), then by an inverse power law nature is decreased to reach its minimum and the mortality rate becomes constant for a while until it finally increases exponentially. The exponential rising (i.e. the ageing of the system) for the first time was described by Gompertz [112]:

This law asserts that as we age (during the wear-out phase) the force of mortality, $\mu(t)$, increases exponentially with age [4, 107, 113]:

$$\mu(t) \simeq ae^{ct}, \tag{5.5}$$

with $a, c > 0$ [107, 112, 114].

From Eq. 5.4 the survival function $S(t)$ of a cohort is given by the integral

$$S(t) = e^{-\int_0^t \mu(t)dt}. \tag{5.6}$$

Inserting for the mortality rate, Eq. 5.5, yields

$$S(t) = e^{-\frac{a}{c}e^{ct-1}}. \tag{5.7}$$

The survival function $S(t)$ thus decreases as a double exponential. This is much faster than the decay of nuclear material for which the force of mortality or death rate, $\mu(t)$, remains constant with time. It is the change of $\mu(t)$ with time which is referred to as "ageing".

The evidence for the validity of the law of Gompertz in so far as it applies to humans is overwhelming. Fig. 5.2 (left) shows data published by Richmond and Roehner [115] for a group of countries where the data is reliable and spans ages up to 95. Fig. 5.2 (right) shows data for a second group of countries where the data is either incomplete or less reliable and spans a lesser age interval. In Fig. 5.2 (left) the convergence of data towards an apparent fixed point is clearly seen. For the data in Fig. 5.2 (right) this convergence is, not surprisingly, less evident.

Mortality of living organisms usually follows the Gompertz law, Eq. 5.5, (however, the naked mole rat as an non-ageing animal is an exception [116]).

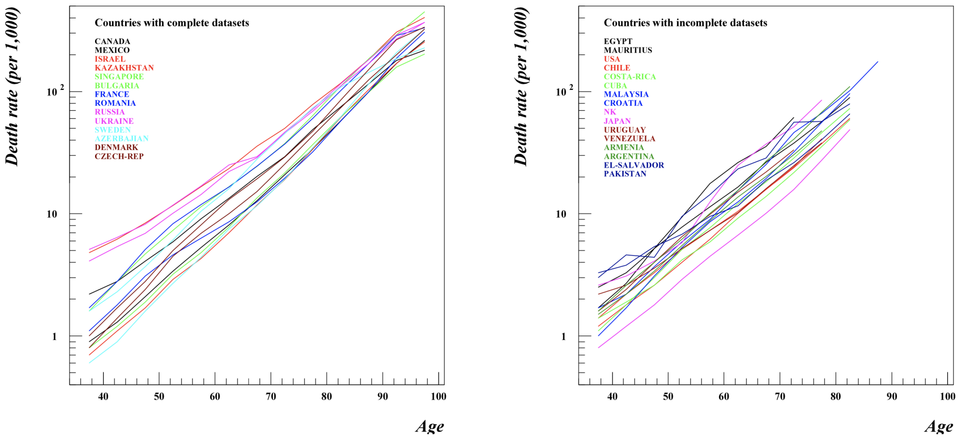

Fig 5.2: Demonstration of the Gompertz law for two sets of countries in a $log - lin$ scale. Left: The death rate data includes the age group 95–99. All data appears to converge towards an endpoint of (∼120,1000). Right: This data obtained for different countries is limited to ages below 85 years. Source: Figures from Richmond and Roehner [115], data source United Nations Demographic Yearbook, 2011.

Section 5.3 shows examples of mortality data for humans, mammals, and other biological species and reviews recent approaches for their interpretations [4].

5.3 Death-Rate Variation for Early and Late Stages of Life

Fig. 5.3 shows age specific death rates for humans in the USA [117]. The axes in Fig. 5.3(a) are log-linear and we see immediately after birth there is a sharp rise in the death rate which subsequently, over the first 100 days of life, decreases. This is mainly due to the inability of many foetuses to survive following the shock of emerging from the watery environment of the womb via the birth canal into the atmosphere. A number of foetuses have *defects*, such as a hole in the heart, cleft palates, aortic valve anomalies, breathing or other difficulties, which make survival extremely difficult, if not impossible.

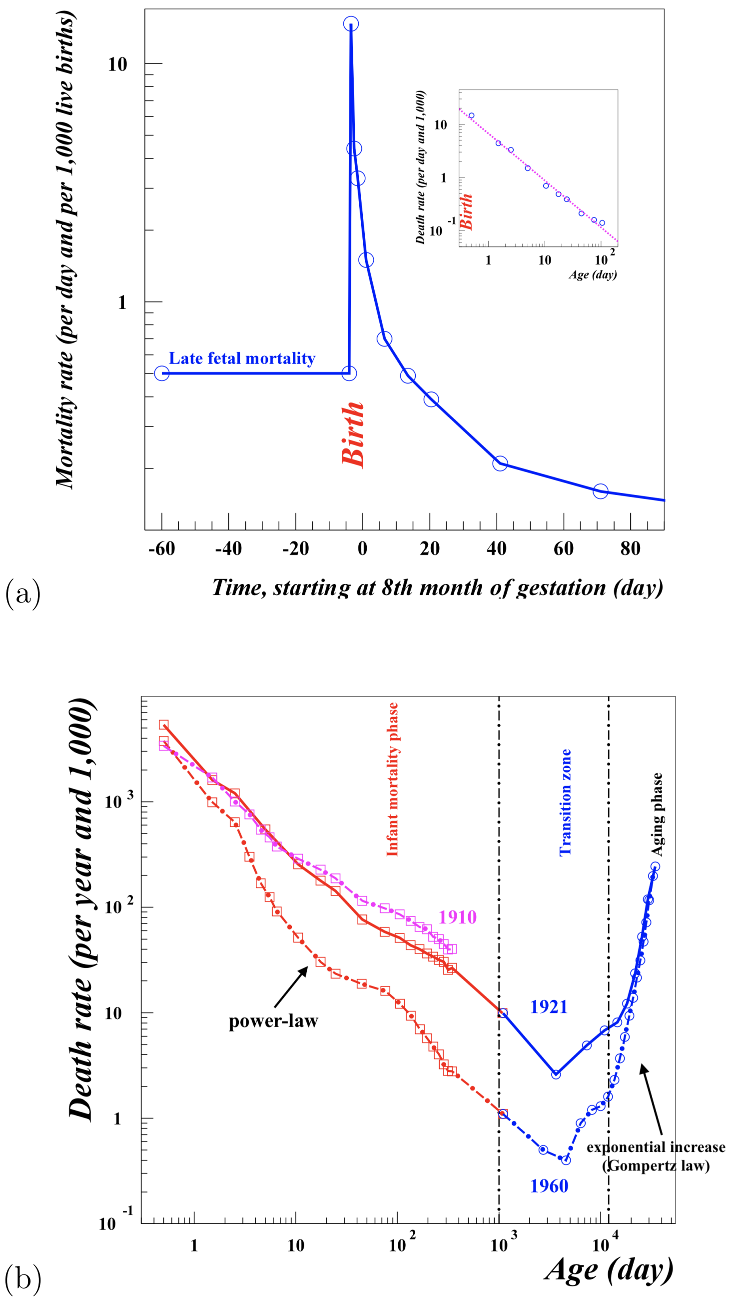

Fig 5.3: Examples of death rate data for the USA [117].(a) The death rate shows a transition from gestation to birth, with a significant increase after birth due to *defects* that were not severe during gestation. The highest point corresponds to the first day, and the rate decreases as a power law in the weeks and months following birth. The log-log plot of the same data has a high coefficient of linear correlation (0.996) and the slope (0.88) of the power law [118]. (b) The US death rate has two phases (infant and aging) separated by a transition. During the infant phase, the death rate decreases in a hyperbolic manner. In 1910, the slope of the falling regression line was $\gamma = 0.65 \pm 0.04$ whereas in 1960 it was $\gamma = 1.01 \pm 0.08$. The decrease has continued in recent years [119, 120].

From our perspective as physicists we could say that the birth process acts as a filter which admits into life only a sufficiently *fit* foetus. In Fig. 5.3b both axes are logarithmic: the death rate for infant mortality phase is seen to decrease as a power law not just for the first year of life but over almost the first two decades of life! So, the effect of any congenital defect remains for a substantial part of early life. Beyond the age of minimum death rate, during the 20–30 age period, the death rate then rises extremely rapidly. In spite of this reduction of the death rate over the infant period, the death rate for 1960 in the adult or wear out phase quickly reaches the same level as that in 1923. It is as if the trend is essentially unchanged as end of life approaches. There would thus seem to be two fixed points for the human death rate; one at the beginning of life and the other at the end of life. Both seemingly are resistant to change. Although at this point, we add a note of caution. Total numbers of deaths in any cohort as we approach the extreme end of life, typically age 95 and beyond, are small, so any statistical analysis towards the end of life is subject to error.

Fig. 5.4 shows that even the common fruit fly has a death rate variation which is similar to that of humans. However, the figure implies that here the death rate levels off for advanced ages.

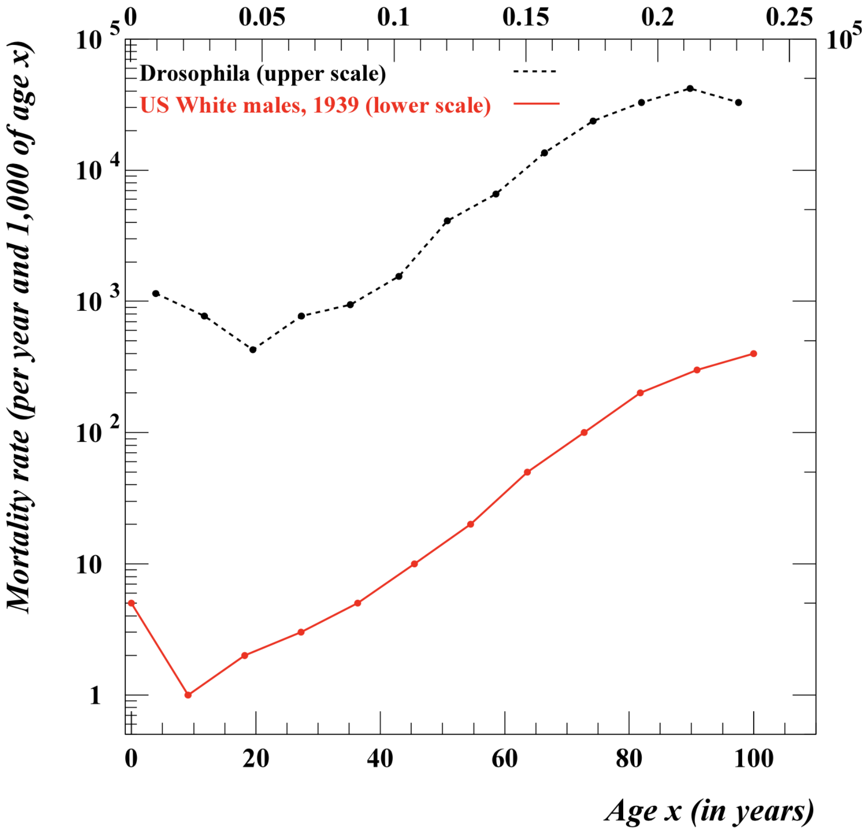

Fig 5.4: Age specific mortality rates for humans and drosophila. The Gompertz law holds in both cases. The levelling off for humans should be attributed to statistical fluctuations, for the drosophila data the reason for this is not entirely clear [115].

5.4 A Simple Model of Infant Mortality

Studies of mortality enable observation of both short and long-term effects arising from congenital abnormalities. Thus, it is tempting to attempt a reverse analysis and derive information about the defects from the death rate curves. Here, we examine how this can be done using a simple model for incandescent light bulbs for which one has a fairly clear understanding of the failure process. To keep matters simple, we assume that only one type of defect is present. Our goal then is to connect the statistical distribution of these defects to the age-specific failure rate of a device.

5.4.1 Failure Mechanism

Light from an incandescent light bulb is produced by a filament heated to a high temperature by an electric current passing through it. A common observation is that such light bulbs frequently fail when switched on. One route to failure may occur during the first milliseconds after the light is switched on when the temperature of the filament can increase rapidly. This creates thermal expansion through which the filament is slightly distorted. If there is already a marked narrowing, the filament may then break. Another cause of failure is the creation of a magnetic field. Again during the first milliseconds, there is a high surge in current intensity due to the fact that the resistivity of the tungsten increases with temperature. This creates a magnetic field that can deform the filament and break it at the most fragile place. This effect is reinforced when the filament is shaped as a coil forming a solenoid.

The resistance R of a filament of length L is given by $R = \int_0^L \rho(x)/A(x)dx$, where $\rho(x)$ and $A(x)$ are local material-dependent resistivity and wire cross-sectional area, respectively. We will, in the following discussion, treat resistivity as a constant, $\rho(x) = \rho$, but allow for fluctuations in the cross-sectional area $A(x)$ along the filament.

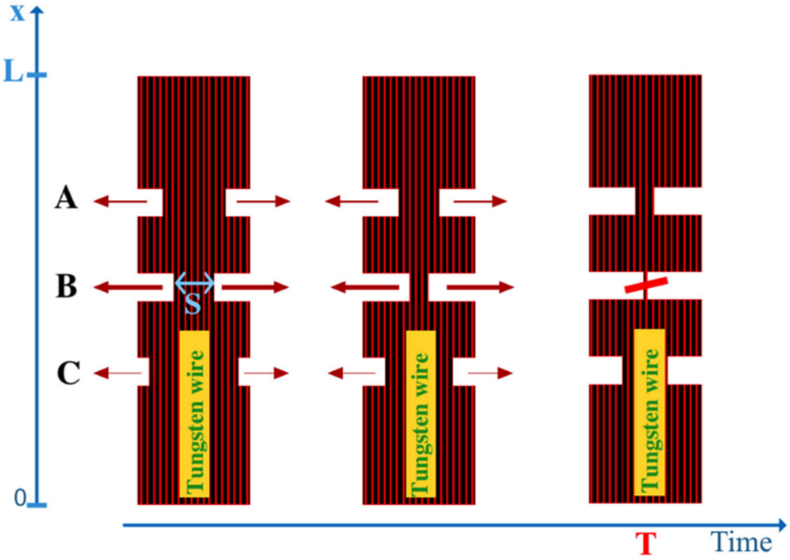

Fig 5.5: Simple model for the thinning and eventual breaking of a tungsten filament in a light bulb due to the flow of an electrical current. Since the local resistance of the filament increases inversely with the local cross-sectional area, there will be greater heat release at narrow sections. This in turn leads to greater local evaporation of tungsten (called filament notching and indicated by the horizontal arrows), eventually leading to the failure of the filament at the narrow section. Note that only the smallest local cross-section, S, that is to say, the most serious defect plays a role in this process. T denotes the time of failure, which is also the lifetime of the light bulb.

A smaller local cross-section $A(x)$ will result in a local increase in resistance dR, and greater heating, which increases the local temperature. (The effect would be even more enhanced had we allowed for an increase in resistivity ρ with temperature in our model.) Around this hot spot, the evaporation of tungsten will be faster than across the cooler regions. This will eventually lead to the severance of the filament and failure of the lamp (see Fig. 5.5). In the simple model considered here, it is the smallest value of $A(x)$ along the filament which will be responsible for the failure, and we denote this by $S = min\ [A(x); 0 \leqslant x \leqslant L]$.

5.4.2 Relation between Distribution of Defects and Distribution of Lifetimes

The time to failure depends upon the degree to which sections of the filament are reduced prior to initial use. This implies there is a one-to-one relationship:

$$T = g(s), \tag{5.8}$$

between the smallest cross-sectional area, s, and the failure time T of the filament (and thus bulb). In principle, $g(s)$ can be obtained from a fairly simple model involving physical relationships related to heating, evaporation, and electrical resistance. Conversely, one could infer the minimum cross-section from knowledge of the failure time.

Considering now an ensemble of light bulbs, a probability density distribution $f_s(s)$ of minimum values of cross-sectional area s, as defined above, translates into a probability density $f_T(T)$ of bulb lifetimes T.

In the simplest case, all bulbs have the same value of s; thus, they will all fail at the same time, say T_1. Thus, the probability density $f_T(T)$ (also called failure density function) will be 0 up until T_1, where there will be a spike (δ-function). For times exceeding T_1, $f_T(T)$ will again be 0.

In the general case, given a probability density $f_s(s)$ of minimal cross sections, the fundamental transformation law of probabilities states that

$$f_T(T)\delta T = f_s(s)\delta s. \tag{5.9}$$

The probability density for the smallest cross-sectional areas is then determined from the failure density function $f_T(T)$ as

$$f_s(s) = f_T(T)g'(s), \tag{5.10}$$

where we have used $\frac{\delta T}{\delta s} = \frac{dg}{ds} = g'(s)$, from Eq. 5.8.

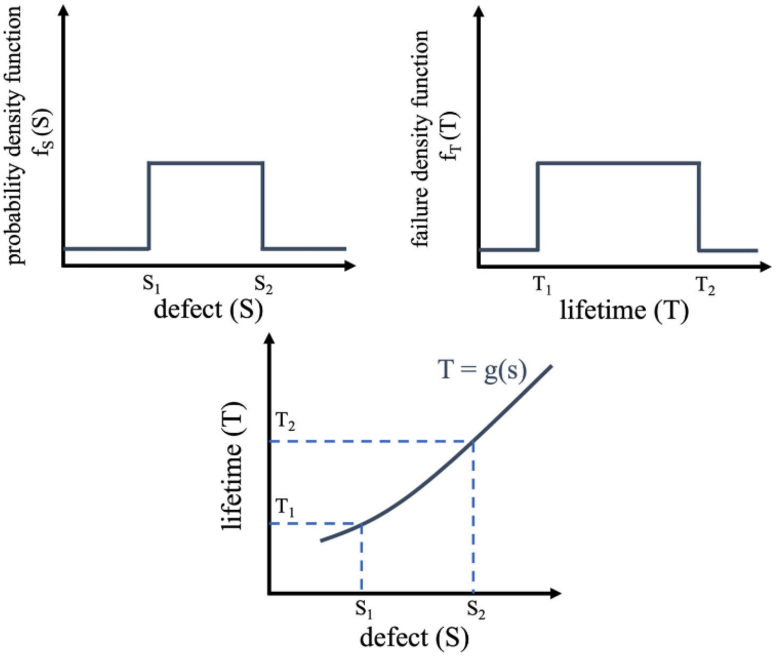

Fig 5.6: Relation between probability density function $f_S(S)$ of defects S, failure density function $f_T(T)$ of lifetimes T, and function $T = g(S)$, linking defect size to lifetime. Knowledge of any two of these relations allows for the computation of the third. For the illustrative example of light bulb failure discussed, we have chosen a rectangular distribution for $f_S(S)$, where the defect S corresponds to the minimal cross-section of the filament (Fig. 5.5).

Thus, knowing the probability density of the failure times, we can in principle compute the probability density of the defects, and reverse.

Let us consider the simple case of a linear function $g(s)$, i.e., $T = g(s) = as + b$, where $a, b > 0$, and a uniform distribution of minimal cross sections, i.e., $f_s(s)$ is constant, within the interval $[s_1, s_2]$; see Fig. 5.6. From $f_T(T) = \frac{f_s(s)}{a}$, it follows that the failure times are also uniformly distributed within the interval $[T_1, T_2] = [as_1 + b, as_2 + b]$. Thus, for this sample of bulbs, there will be no failures up to the time T_1 where the first failure will occur. More failures will follow with a constant frequency until time T_2 when every member of the sample will have failed [3]. It can be used for any device whose lifetime is determined by a single parameter and we will use it in Section 5.6 (in a

---

[3] This is indeed what one observes for fish mortality in the yolk sac phase [117].

modified form) for soap films confined in tubes of various lengths.

What makes this argument important here is that it connects what we can observe and measure, namely the age-specific death rate, to birth defects. Written in terms of the survival function $S(t)$, Eq. 5.10 is expressed as

$$f_s(s) = -g'(s)\frac{dS(t)}{dt}, \tag{5.11}$$

where we have used Eq. 5.3.

It is in this sense that infant mortality gives us an insight into the internal working of a device or organism. In Section 5.6, we will demonstrate the application of Eq. 5.11 for experimental data for the lifetime of soap films.

5.5 A New Approach for Studying Failure Statistics Using Soap Films as a Model System

Our discussion so far has centered on data for biological systems. The understanding of mortality curves is of relevance also to man-made products, where the term mortality rate is replaced by failure rate. While vast amounts of data undoubtedly exist, these are generally not available to consumers, but kept by the producers, possibly to avoid litigation. A notable exception is the data bank for the lifetime of computer hard disk drives (HDD) which is maintained by the cloud-storage provider Backblaze [4].

Having access to a simple physical system as a source of failure data would allow for a set of controlled experiments to accompany and probe theories of failure. Since such experiments are by definition of a statistical nature, the data sets need to be sufficiently large; failure times should not be too long.

Haffner *etal.* recently suggested that soap films, produced under controlled conditions and confined in cylindrical tube, may serve as such a system [102].

---

[4] https://www.backblaze.com/blog/how-long-do-disk-drives-last/.

In addition, using a simple model system for the lifetime of light bulbs, we have argued in Section 5.4, we will show in Section 5.6 that a defect distribution can be mapped into a distribution of soap film lifetimes, and vice versa.

5.5.1 Ageing of a Soap Film

Do soap bubbles show their age? To answer the question, first, let's define what we mean by a soap bubble. We use the word soap bubble to describe a thin aqueous film, stabilized by surfactant molecules, which assemble mainly along the two liquid-air interfaces (see Fig. 5.7)[121]. Also, there is a good review by Miguet *et. al.* talking about soap bubble lifetime in the absence and presence of surfactant molecules [122].

Over the course of its lifetime, a surfactant-stabilized liquid film experiences several stages of aging which are generally well understood within the framework of physics and physical chemistry [121, 123]. For instance, Hamlett *et. al.* studied the effect of surfactant solution on bubble lifetime and showed bubbles stabilized with a pure SDS are much more prone to burst than a commercial dishwashing liquid such as *Fairy Liquid* [124]. However, an understanding of the final stage of aging, i.e., the detailed mechanism of the film *rupture*, is still limited [125]. The longevity of such liquid films depends crucially on their (local) thickness. This generally reduces with time, as the films drain due to capillary forces and gravity, with a further loss of liquid due to evaporation. The evaporation effect on film lifetime for surface bubbles and giant soap films ($\sim$ 2m in height) has already been discussed in a humidity-controlled atmosphere [126, 127].

The thickness of a freshly formed film ranges between 1 and 100 μm [17], but it is rapidly reduced due to the drainage of liquid out of the film. In thick vertically displayed films, gravity plays an important role in establishing a vertical gradient in thickness. But, as in the case of horizontal films, capillary action is the key driver for film thinning. The timescale for this process is set by both bulk and surface viscosity of the surfactant solution [123], together with film orientation.

Once the local film thickness has decreased to about 100 nm, drainage is slowed down, as eventually the attractive van der Waals forces on the opposing sides of the film are balanced by steric and electrostatic repulsion due to the presence of surfactant molecules. This is accompanied by the formation of small areas (*spots*) on the film which appear black in reflection and are indicative of a thickness of less than about $30nm$ (common black film). These black spots grow in size and merge, resulting in a liquid film which appears completely black in reflection. Evaporation may reduce the film thickness even further, down to about 5 nm (Newton black film) [17]. Such films are metastable, but they ultimately rupture, as thermally induced thickness fluctuations may result in the formation of a hole which rapidly grows in size. Evaporation is seen to play a significant role in film stability in this regime [126] and film lifetime increases with relative humidity [128].

Film rupture may also be triggered via the deposition of particles onto the film or the addition of anti-foaming chemicals which reduce or replace the amount of surfactants at the interface. The former mechanism might play a role in our experiments described below since they do not take place in a dust-free environment. This would be a further support of the view that film rupture should ultimately be seen as a stochastic process [125].

Figure 5.7 shows a soap bubble along with a sketch of a planar soap film and Fig. 5.8 represents the rupturing process timeline of a soap film as described above. *drainage* and *evaporation* are the two main reasons for ageing of a soap film. Here, the lifetime is the time between the creation of a film out of a surfactant solution and its eventual rupture which is, in many cases, brought about by statistical thermal fluctuations. Furthermore, Fig. 5.9 shows a sequence of photographs of a soap film located in the middle

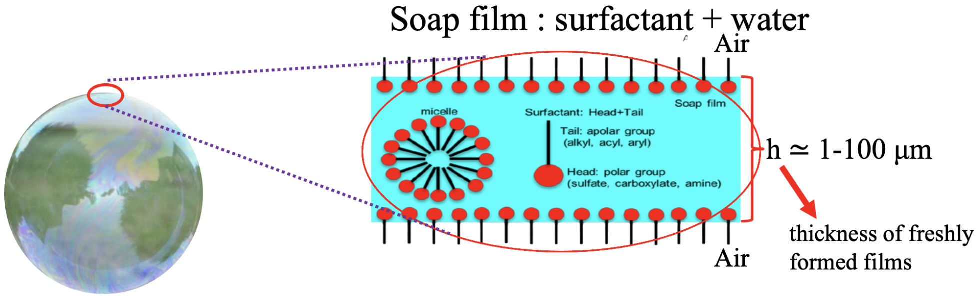

Fig 5.7: (a) Soap film comprises of surfactant solution and water, is thin aqueous film surrounded by air. Typically thickness of a soap film is less than 1 to 100 μm.

of a cylindrical tube placed horizontally and vertically.

So, thin liquid films, stabilized by surfactants, may be used as a simple physical system for an experimental study of the statistics of failure [101, 102].

The lifetime of a soap film is thus a well-defined quantity. A film either exists or has vanished: there is no in-between state. This, together with the simple and inexpensive experimental setup, makes such films a suitable experimental system for the study of failure. This was previously explored by Hutzler et. al. [101, 102], who studied ensembles of $10 - 20$ films that were placed equidistantly in (sealed) vertical glass or perspex cylinders. Data for over 4000 films showed that for this setup, which allowed for film interactions in the cylinders, the long-term failure/mortality rate is best described by an exponential increase in time (Gompertz law, see Eq. 5.7).

5.5.2 Experimental Set-Up

All our experiments were performed at room temperature using solutions made from sodium dodecyl sulfate (SDS, purity $\geq$ 90%, and molecular weight of 288.38 g/mol purchased from Sigma-Aldrich), dissolved in Millipore water at a concentration of 10.1 g SDS to 290 mL water which is 3 times above the critical micelle concentration, CMC [129]. This concentration is high enough to ensure film stability. Also, Champougny *et. al.* studied the effect of surfactant

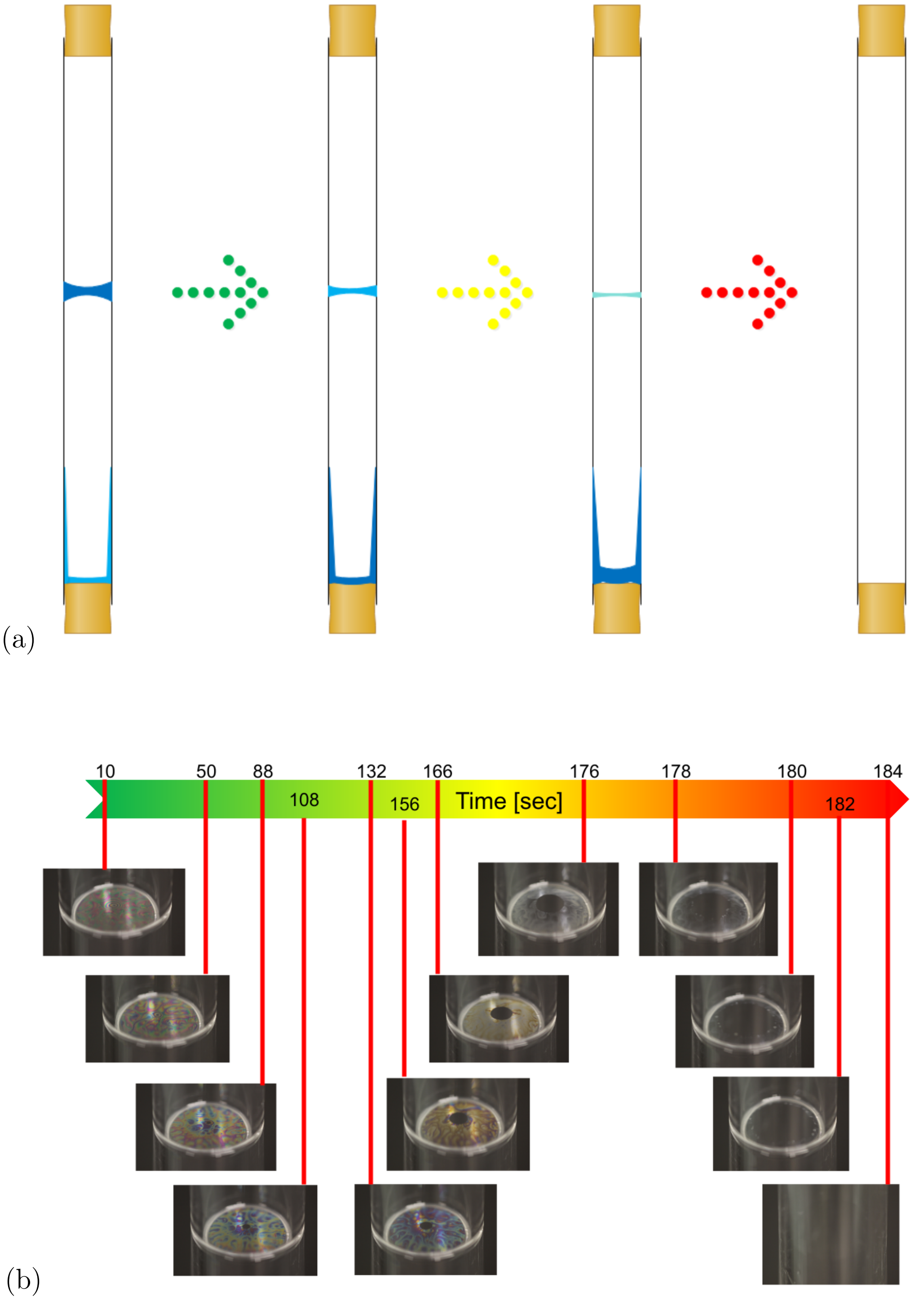

Fig 5.8: Rupturing process of a soap film. (a) Cross-sectional view of thin film placed in the middle of a sealed tube. (b) In the example shows a *Newton black film* appears at about $t = 108sec$ in the center of the soap film. The film grows, eventually leading to film rupture.

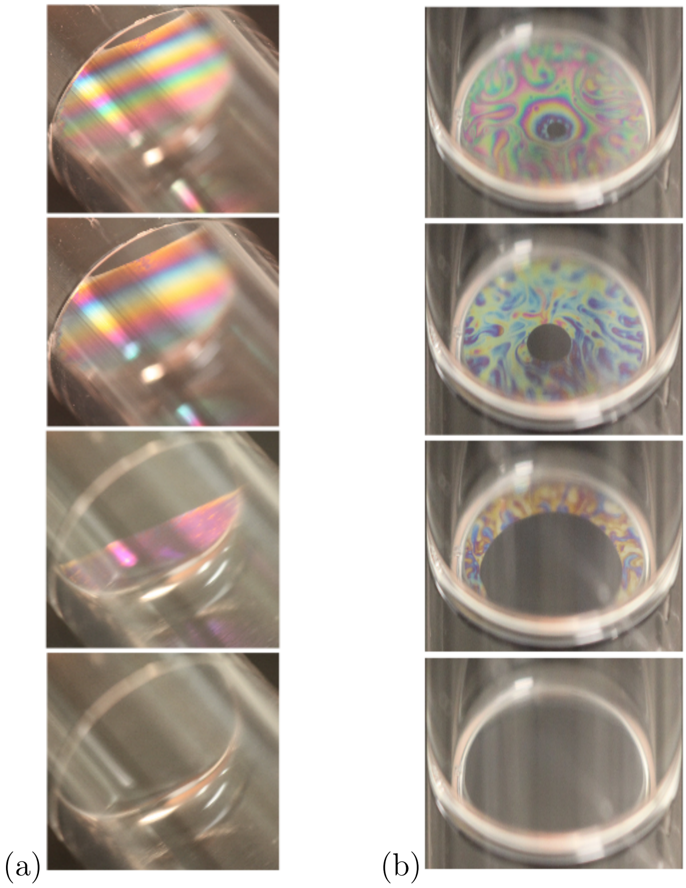

Fig 5.9: Appearance Newton black film and interference pattern in a soap film. A sequence of images of a soap film located in the middle of a cylindrical tube placed horizontally (a) and the tube placed vertically (b). Both show the interference pattern, appearance, and growing of the Newton black film due to drainage.

concentration on film stability and surface bubble lifetime [130]. The solutions were freshly prepared for each experimental run, using a magnetic stirrer for about 30 min. The temperature and humidity were monitored for some experiments but we could not detect any influence on average film lifetime for the fluctuations in the laboratory temperature, which were about ± 1.5°C.

We used sets of Perspex tubes of three different lengths (L = 3 cm, 10 cm, 20 cm) and internal diameter 1.6 cm which we sealed with one or two standard laboratory rubber stoppers. The tubes were cleaned and then dried before each experimental run.

An individual liquid film was created by dipping a tube perpendicularly into the SDS solution and then withdrawing it. Each of our tubes contained only one film, placed in its middle; see the schematic in Fig. 5.10 (a).

The tubes were monitored using a digital video camera (AVT Marlin F131B) connected to a PC, with images being recorded every 6 seconds. We found it convenient to image a row of 12 parallel aligned tubes in one experimental run; when using short tubes, as shown in Fig. 5.10 (b), it was possible to record two such rows (corresponding to two experimental runs) in one session. The lifetime of each film was determined from visual inspection of the recorded images and taking the time-stamp of the last image at which a film was still present in the tube.

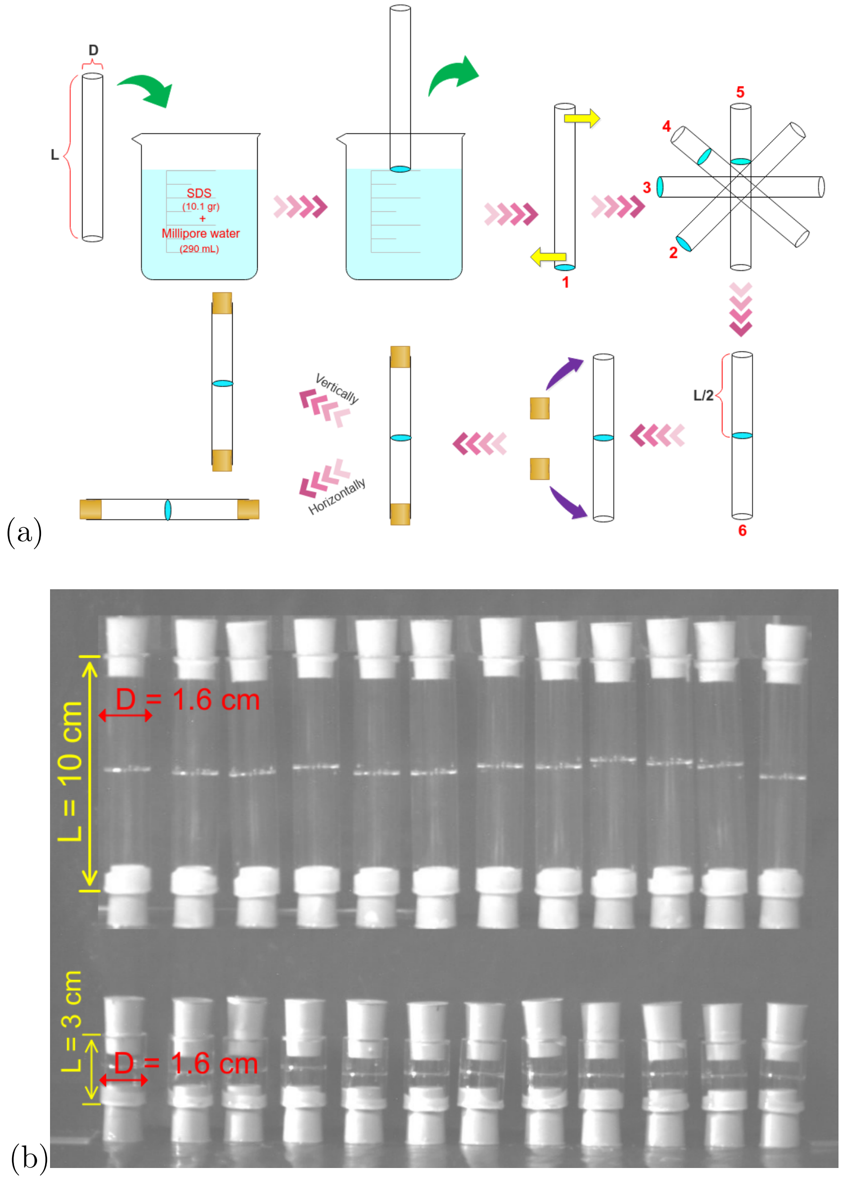

Fig 5.10: Experimental setup. (a) Liquid films were created by dipping glass tubes of three different lengths (and for the data presented here, with diameter 1.6 cm) vertically into an aqueous SDS solution and then withdrawing them. At this stage, by rotating the tube, the films are free to slide along the tube wall and can be brought to the center of the tube. Sealing the tube at the bottom end using a rubber stopper then fixes the film position. Finally, the tube were placed vertically or horizontally. Experiments were also carried out where the tubes were sealed with two stoppers. (Dimensions of the conical stoppers: length 2.4 cm: max. and min. diameters 1.5 cm and 1.8 cm). (b) Photograph of the setup for an experimental run featuring 24 vertical tubes of two different lengths, sealed with two stoppers, and containing one film each. The horizontal films appear as thin bright lines.

5.6 Results

The following section outlines our research findings. First, we will begin by presenting the results of our experiments, in which we will determine the average lifetimes of individual soap films. Our results reveal a bath-tub curve of mortality as discussed in Section 5.1 and illustrated in Fig. 5.1.

Lastly, we focus on early-stage (infant) mortality for soap films using the failure mechanism described in Section 5.4.1. Using measurements of lifetimes for soap films, we show how this methodology links failure rate to the geometry of the system; in the case presented, this is the length of the tube containing the films.

5.6.1 Lifetimes of Individual Soap Films

We determined the lifetimes of individual soap films, which were contained in fully sealed and vertically aligned tubes, as well as in tubes that were only sealed at the bottom end. Our results indicate that exposure to increased evaporation led to a reduction in the average lifetime of the second data set, bringing it down to approximately one-fifth of the average lifetime observed in films contained within fully sealed tubes.

In Fig. 5.11(a) we show as a function of time the fractions of films contained in the 144 tubes with two stoppers, and in the 144 tubes with only one stopper, respectively. After slightly over three minutes the film population in the one-stopper tubes has vanished entirely. Also shown is the survival or reliability function $S(t)$ of the combined data set, which steadily decreases from its initial value of 1. After about 15 min only 10% of the initial 288 films remain intact, all of which are in the two-stopper tubes.

From the survival function $S(t)$ we can compute the corresponding failure rate, $\mu(t)$, using Eq. 5.4. Fig. 5.11(b) shows that following a steep initial rise due to the rupture of films in the one-stopper tubes, $\mu(t)$ decays again in the time interval from 2 to 5 min, as this short-living film population gradually vanishes. This behavior is reminiscent of the death rate spike after birth shown in Fig. 5.3(a) (high burn-in rate or infant mortality). From about 5 min onward, $\mu(t)$ begins to rise again, as now rupture also becomes prevalent in the films contained in the two-stopper tubes. This functional variation of $S(t)$ is what is called the bath-tub curve of failure, a curve shape we have already encountered in Figs. 5.3(b) and 5.4.

5.6.2 Relation between Defect Distribution and Soap Film Lifetimes

So far, we presented the survival function and mortality rate for our collection of soap films in which the bath-tub curve also appeared. Now, we show a reverse analysis and derive information about the defects from the death rate curves using the methodology introduced in Section. 5.4.

Here, we show the lifetimes of individual films under a variety of different experimental conditions (see C.1 for a summary of all experimental data). For example, we placed the films in Perspex cylinders of different lengths or cross-sectional area. This resulted in a number of empirical relationships for the average lifetime, $\langle T\rangle$, as a function $g(S)$ of these "control parameters" which here we denote by S, in which they take on the role of lifetime-defining *defects*. The requirement to use the average film lifetime is due to the substantial role that fluctuations play in film stability (see the discussion below).

Using the relation

$$\langle T\rangle = g(s) \tag{5.12}$$

together with the failure density function $f_T(T)$ obtained from our experimental data, will allow us to identify the underlying defect distribution $f_s(s)$ using the mathematical framework developed above, see Fig. 5.6.

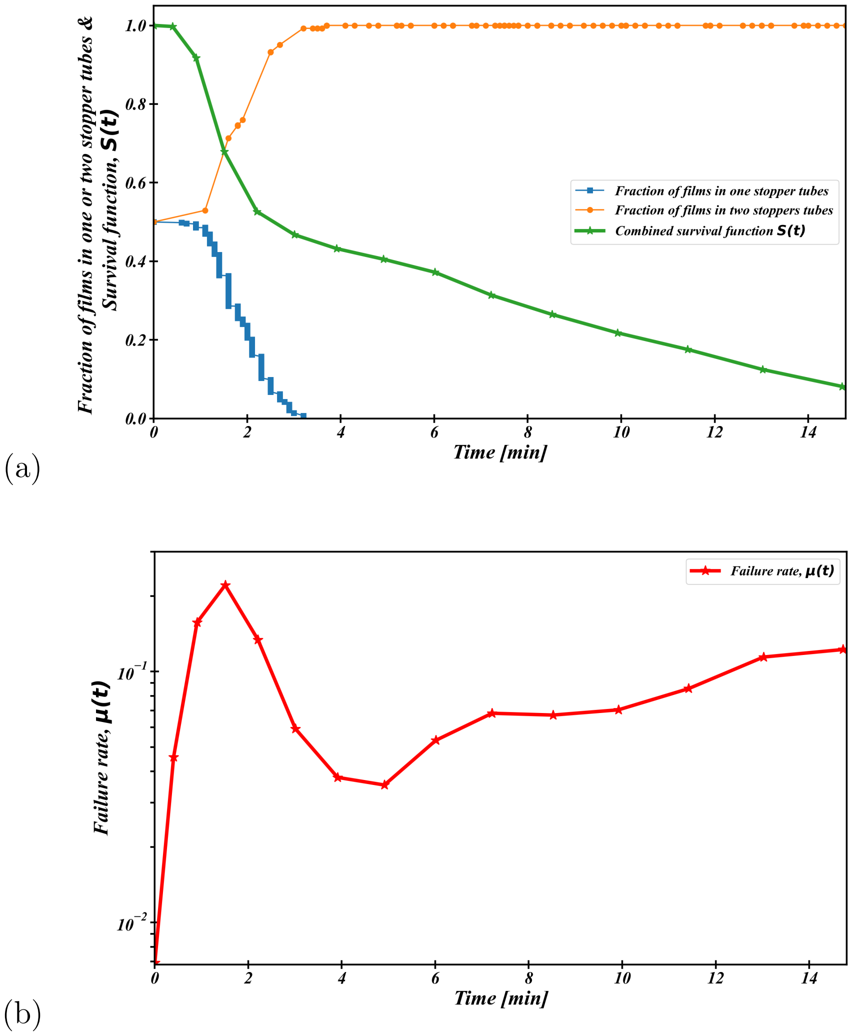

Fig 5.11: Experimental data for a total of 288 horizontal soap films contained in vertical glass tubes (length 3 cm, diameter 1.6 cm), 144 of which were sealed with one, and 144 sealed with two stoppers. Data is shown prior to when only 10% of the initial number of films are left in order to avoid fluctuations in the computation of the failure rate, $\mu(t)$, due to the small number of films remaining. (a) The films in the one-stopper tubes all rupture within about three minutes; as their fraction of the total number of films drops to zero, the fraction of films contained in the two-stopper tubes rises to one. Also shown is the survival function, $S(t)$, of the combined data set. Over the 15 min shown it decays from 1 to about 0.1. (b) Variation of the corresponding failure rate $\mu(t)$, computed using Eq. 5.4. At about 2.5 min $\mu(t)$, starts to decrease, as the rupturing of the films in the one-stopper tubes slows down. The failure rate rises again after about 5 min, due to the increased occurrence of film rupture in the two-stopper tube.

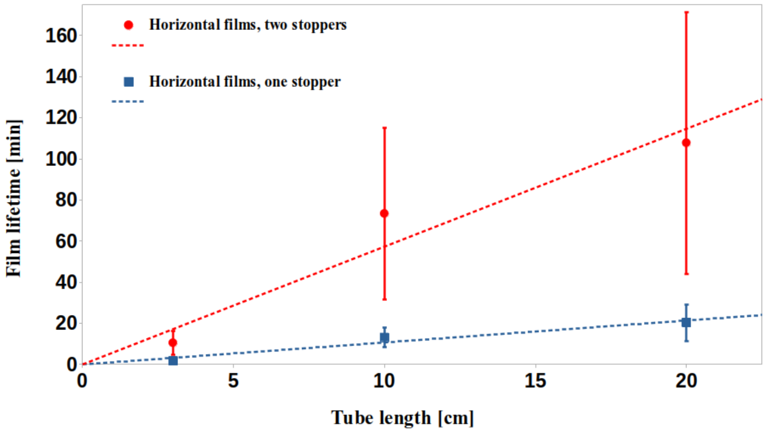

Fig 5.12: The average lifetime $\langle T \rangle$ of a liquid film enclosed in the center of a tube varies roughly linearly with the tube length L. Sealing the tube at both ends leads to a large increase of average film lifetime, in comparison to sealing it only at the bottom end. Each data point is the average over 144 measurements; the fluctuations are substantial (coefficient of variation $C_V \simeq 0.6$ in the case of two stoppers; $C_V \simeq 0.4$ in the case of one stopper). Linear regression leads to slopes $c = 1.08 min/cm$ (one stopper) and $c = 5.57 min/cm$ (2 stoppers), with corresponding offsets $T_0 = -0.09$ min and $T_0 = 2.56$ min

The data presented and analyzed below is for a total of 852 films, contained in tubes of width 1.6 cm and length 3 cm, 10 cm, and 20 cm, respectively. The tubes were placed vertically, i.e., all films were oriented horizontally. In one set of experiments, the tubes were sealed with rubber stoppers at both ends; in the other set, the stopper was inserted only at the bottom end.

Figure 5.12 shows that the average lifetime $\langle T \rangle$ of a film increases approximately linearly with the length L of the tube in which it is contained, i.e.:

$$\langle T \rangle = g(L) = T_0 + cL \tag{5.13}$$

where the fit parameters c (dimension: time/length) and T_0 (dimension: time) were determined using linear regression. (An offset T_0 was included in the fit since it is possible to maintain a film at finite lifetime even in the limit where a tube is shortened to just a ring. Note, however, that in the analysis that follows, only the value of the slope c is of relevance.)

Before moving on with our analysis, we need to comment on the possible origin of this linear relationship of Eq 5.13. We find that it is valid also for a number of variations of the setup described here, involving tubes that were placed horizontally or vertically, sealed with two or one stoppers, or even not closed at all. However, only the data sets for the tubes of 1.6 *cm* diameter that were vertically oriented have been analyzed in this thesis. Why? Because liquid drains from the films due to gravity when the tubes are oriented horizontally (and consequently, the films are oriented vertically). Moreover, liquid gathers in the menisci at the lower portion of the film, and since an accurate horizontal tube display could not have been ensured, there was a chance that liquid may have leaked from the menisci and gathered at one end of the tube.

Fig. 5.13 shows an example of the effect of film orientation on lifetime. Here, a single soap film was placed in the center of the tubes with three different lengths, i.e., $3\ cm,\ 10\ cm,\ and\ 20\ cm$ with a diameter of 1.6 *cm*. All tubes were sealed at both ends.

The range of average lifetimes differs in all these different sets of experiments; however, the linear dependence on tube length remains, although with different values for the constant c. The details of these findings, based on a total of $15 \times 144 = 2160$ films are shown in Appendix B.

What is the origin of the linearity? In not sealing tubes, there clearly is a (roughly linear) gradient in humidity along the tube, as it varies from 100% at the film location to its ambient value at both tube ends. As commented above, evaporation plays a major role in film stability, and evaporation is driven by humidity gradients. The longer the tube, the smaller the gradient will be, which should in turn lead to longer lifetimes.

We assume that such gradients also exist in tubes that are sealed (the quality of the seal was confirmed by probing for leakage when immersing a

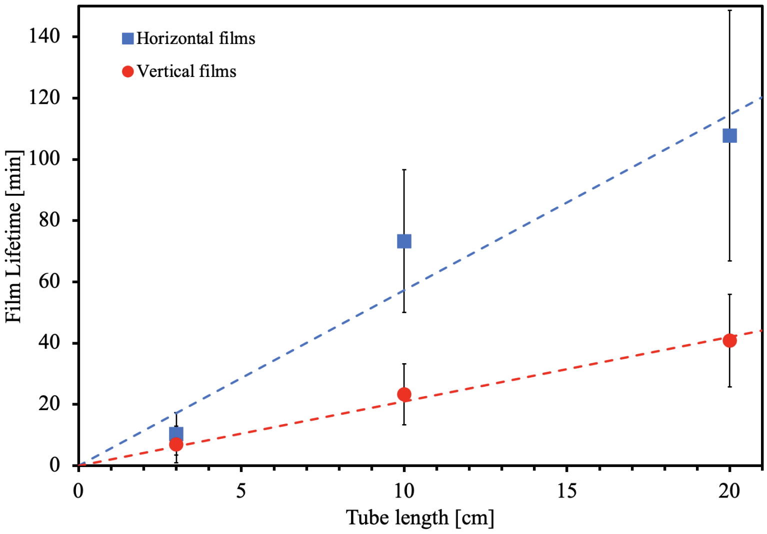

Fig 5.13: Effect of film orientation on lifetime. The average lifetime $\langle T \rangle$ of a liquid film enclosed in the center of a tube varies roughly linearly with the tube length L. Here, the tubes with three different lengths ($3\ cm,\ 10\ cm,\ and\ 20\ cm$) were sealed at both ends. Placing the tube vertically (horizontal film) leads to a large increase in average film lifetime, in comparison to tubes placed horizontally (vertical film). Each data point is the average over 144 measurements; the fluctuations are substantial. Linear regression leads to slopes $c = 2.11 min/cm$ (vertical film) and $c = 5.73 min/cm$ (horizontal film), with corresponding offsets $T_0 = 1.94 min$ and $T_0 = 2.56 min$.

sealed tube in water); also in this case humidity will be 100% at the film and decrease away from it to some finite value, in this case generally higher than that outside the tube. The argument for obtaining an increase in film lifetime by having longer tubes is thus as above.

Clearly, average film lifetimes cannot increase indefinitely with tube length and we expect it to level off eventually, making other factors the most relevant ones for film rupture.

Let us stress here that we do not claim to have a full understanding of both *origin* and the possible breakdown of the linearity. However, for the following discussion, the origin of linearity is not key. It is rather the existence of an empirical law for average film lifetime as a function of tube length which is required to make a prediction of the distribution of tube lengths from measurements of the lifetime of the films they contain.

We will for the following analysis represent our data in terms of the survival function $S(t)$ which was introduced in Eq. 5.1.

From our data for the lifetime of individual films, we can construct a time series $N(t)$, where $N(t)$ is the number of films that are still intact at time t. The survival function is then computed as $S(t) = N(t)/N(t = 0)$.

The initial number of films was $N(0) = 144$ in all but one of our different types of experiments (in the one-stopper experiment for the 10 cm tube $N(t = 0) = 132$). Note that $S(t)$ decreases whenever one (or more) film ruptures at time t. Figure 5.14 shows that in both our one- and two-stopper data an initially very slow decay of $S(t)$ away from $S = 1$ eventually gives way to a rapid drop, before the decay slows down again until all films have ruptured, i.e., $S = 0$.

In order to test whether information on the distribution of tube lengths (in our case, three $\delta - functions$ with peaks at $L = 3$ cm, 10 cm, 20 cm) can be obtained from an analysis of film lifetime data for the one- or two-stopper experiment we have proceeded as follows. Our starting point will be the

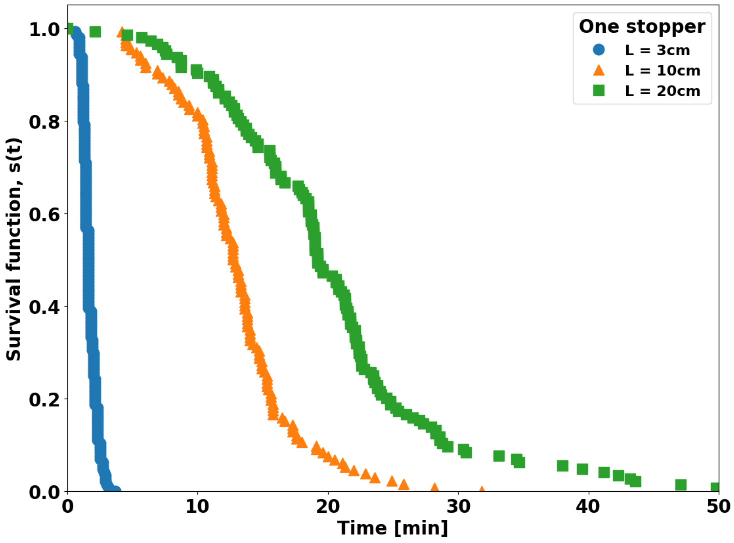

(a)

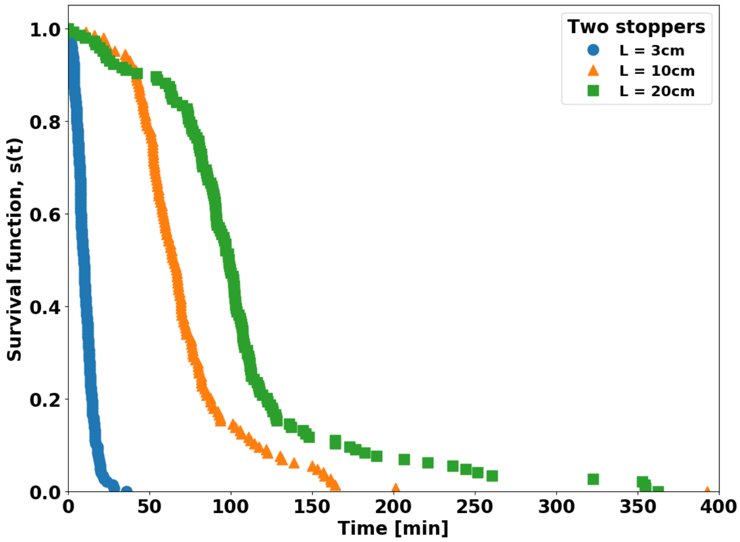

(b)

Fig 5.14: Variation of survival/reliability function $S(t)$ as a function of time for films in tubes of length 3 cm, 10 cm, and 20 cm, respectively. Note that the lifetimes of the films in the tubes sealed with two stoppers (b) greatly exceeds those in tubes sealed with only one stopper (a). This highlights the effect of evaporation. The initial number of films in each of the different types of experiments was $N(t = 0) = 144$, apart from the one-stopper data for the 10-cm tube, where $N(t = 0) = 132$. The survival curve for the 10 cm intercepting with 20 cm tube at about 5 min for the tubes sealed with on stopper and about 50 min for the ones sealed at both ends which indicates the drainage and evaporation for those tubes are initially at the same rate, then will be increased for the 10 cm tube.

aggregate of the three survival functions, shown in Figs. 5.15(a) and 5.16(a). We have employed some smoothing to the data by grouping it into bins along the time axis. We have also applied a time-weighting that takes into account the times within each bin at which $S(t)$ changes its value. Furthermore, we have chosen bin sizes that increase linearly with time to account for the fact that more film ruptures occur at earlier times.

Knowledge of the reliability function $S(t)$ allows for the computation of the failure density function $f_T(t) = -\frac{dS(t)}{dt}$ (Eq. 5.3). The derivative was obtained numerically from our binned data for $S(t)$ (Figs. 5.15(a) and 5.16(a)) using the central difference method.

In the case of our soap film data, we only know the variation of the average lifetime $\langle T\rangle$ with tube length L. Using Eq. 5.9, we argue that in this case the distribution $f_L(L)$ is approximately given by:

$$f_L(L) \simeq \frac{d\langle T\rangle}{dL} f_T(T) = -\frac{d\langle T\rangle}{dL}\frac{dS(t)}{dt}. \tag{5.14}$$

Similarly to the treatment in proportional hazard models [131], we have empirically identified a covariant, or risk factor (in our case the tube length), which is multiplicatively related to the "hazard". As in a so-called semi-parametric model, the mean response in our population of films, namely the average film lifetime, depends linearly on the covariant.

We have also computed the coefficient of variation (ratio of the standard deviation of $f_T(T)$ to its mean $\langle T\rangle$) and find that it is independent on tube length (although it differs between the two-stopper and the one-stopper data). The mean lifetime $\langle T\rangle$ may thus be taken as a first approximation to the distribution $f_T(T)$. The distribution function itself is independent on the specific set of lifetimes we observe in our experiment. Were we to repeat the experiment we would observe a different set of lifetimes but the distribution function $f(T)$ would be unchanged.

From Eq. 5.14, and use of Eq. 5.13, we then obtain:

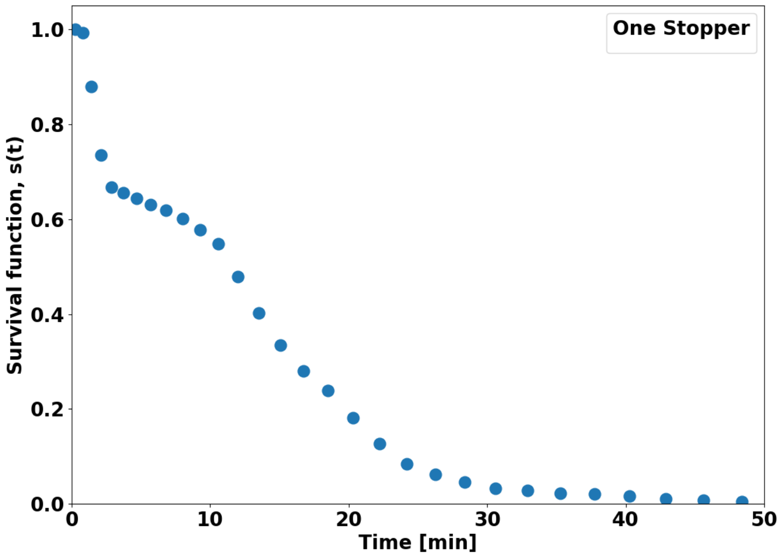

(a)

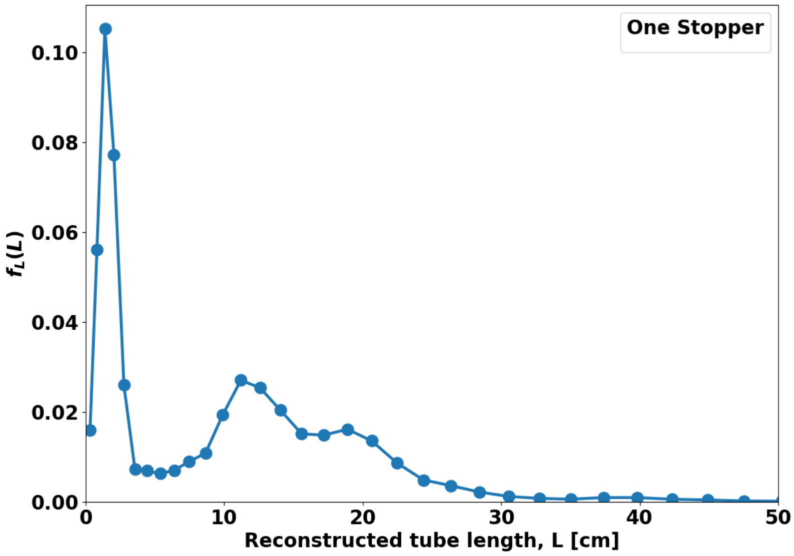

(b)

Fig 5.15: (a) Survival function $S(t)$ for a combined and smoothed data set of 132 + 144 + 144 films placed in tubes of three different lengths (3 cm, 10 cm, and 20 cm) closed with only one stopper (c.f. Fig. 5.14(a)). (b) Reconstruction of the distribution of tube lengths using the methodology described in the main text, Eq. 5.13, 5.14 and 5.15. The three discernible peaks at around 2 cm, 11 cm, and 19 cm correspond to the three different lengths of the tubes used in the experiments.

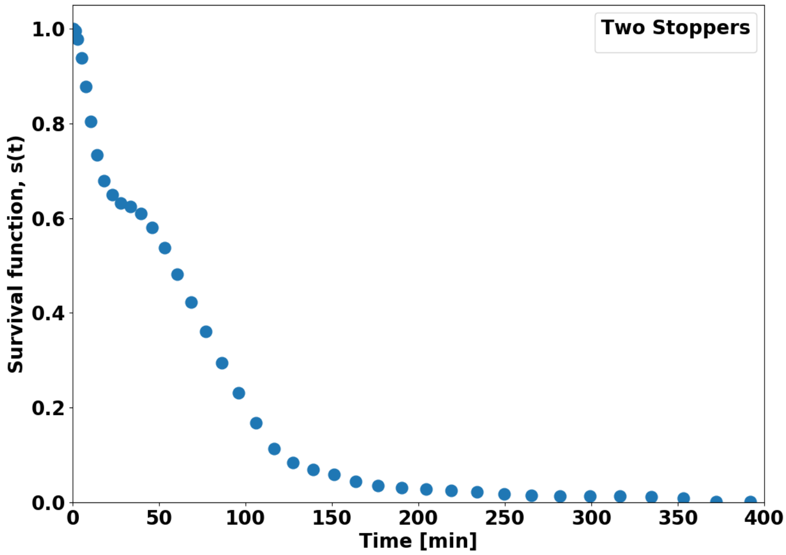

(a)

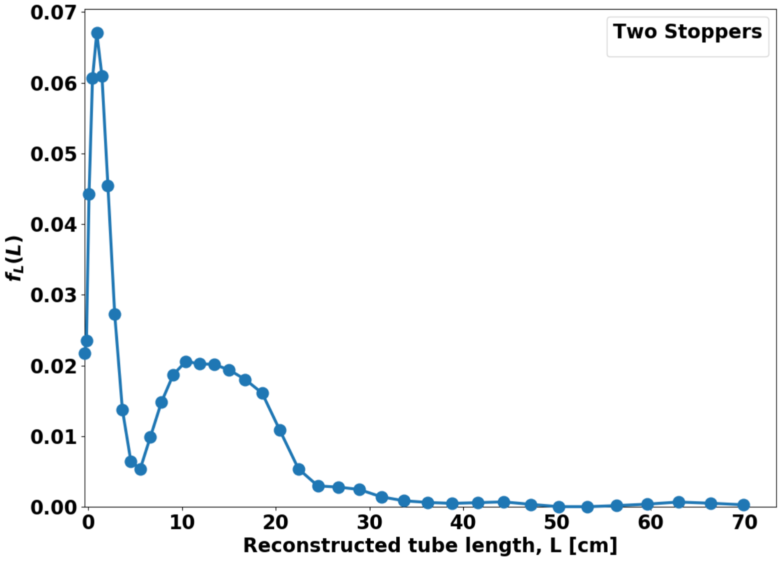

(b)

Fig 5.16: (a) Survival function $S(t)$ for a combined and smoothed data set of 3 × 144 films placed in tubes of three different lengths (3 cm, 10 cm, and 20 cm) sealed with two stoppers (c.f. Fig. 5.14(a)). (b) Reconstruction of the distribution of tube lengths using the methodology described in the main text, Eqs. 5.13, 5.14 and 5.15. There is a sharp peak at $L \simeq 2cm$ and a broad peak between about 8 and 22 cm. Our data for the two-stopper experiment is thus not of sufficient quality to differentiate between the 10- and 20-cm tubes used in the experiments. Here, the missing second peak originated in the intercept of Fig. 5.14.

$$f_L(L) \simeq c f_T(T) \tag{5.15}$$

where the constant c is determined by linear regression; see Fig. 5.12.

The results of applying Eq. 5.14 and 5.15 are shown in Figs. 5.15(b) and 5.16(b), which display the computed distributions $f_L(L)$ for respectively one- and two-stopper data. Conversion of the time axis into a length axis is via $L = \frac{<T> - T_0}{c}$ (from Eq. 5.13).

In the case of our one-stopper experiment, the distribution $f_L(L)$ clearly indicates the presence of three dominant tube lengths of about 2 cm, 11 cm, and 19 cm (which might serve as a further justification of Eq. 5.14). For the two-stopper experiment, only two peaks can be identified, one of which is very broad; the inherent noisiness of the data makes it impossible to resolve film ruptures in the 10 cm tube from ruptures in the 20 cm tube. Figure 5.14(b) shows that this is due to the time interval from about 75 to 90 min where both film populations suffer from increased rupturing.

Let us note that our data sets are quite limited in size; our sets of 144 films for each experiment type are much smaller than what was used in previous studies which involved collections of film in tubes [101, 102]. Presumably, a larger number of films would reduce noise, resulting in a smaller coefficient of variation than what we obtained here($C_V \simeq 0.6$ in the case of two-stopper data; $C_V \simeq 0.4$ in the case of one-stopper data).

Despite these current limitations, our analysis presented in Figs. 5.15 and 5.16 has demonstrated that it is possible to deduce a distribution of tube lengths, $f_L(L)$, from statistical lifetime data, $f_T(T) = -\frac{dS(t)}{dt}$. The necessary requirement for this is a relationship between average lifetime and tube length, i.e., the relationship shown in Fig. 5.12. We have had similar success also for our analysis of vertical films, confined in horizontally placed tubes (to be presented elsewhere).

Lifetime data for biological systems is generally presented in terms of a

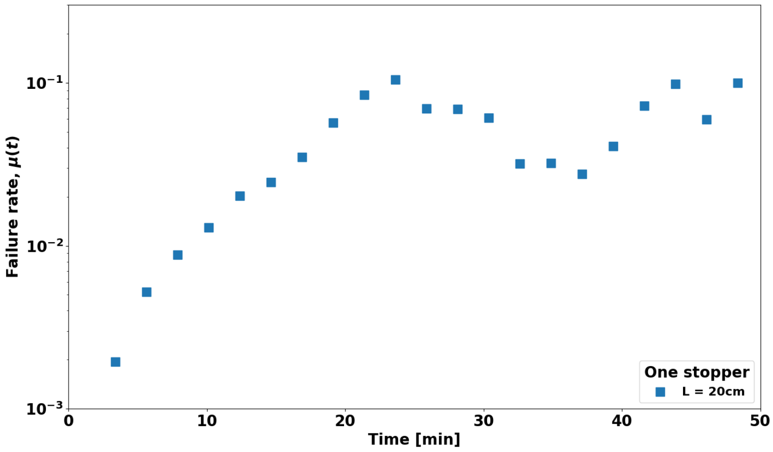

Fig 5.17: Time-dependent failure rate/hazard function $\mu(t)$, Eq. 5.4, for films contained in tubes of 20 cm length, closed with only one stopper. Up to about 25 min, the failure rate increases roughly exponentially, before fluctuating around a constant level. The size of the fluctuations reflects the very small number of remaining films, cf. the corresponding survival function $S(t)$ shown in Fig. 5.14(a)

death rate (failure rate), $\mu(t)$, as was introduced in Section 5.1, Eq. 5.4.

Figure 5.17 shows $\mu(t)$ as computed from the one-stopper data in the case of the 20- cm-long tube shown in Fig 5.14(a). An initial roughly exponential increase of $\mu(t)$ levels off after about 20 min and gives way to fluctuations about a roughly constant value. We find qualitatively similar behavior also for our other data sets, not shown here. Again there is an exponential increase in the failure rate, i.e., the form associated with the Gompertz law for human mortality [115] or a type I survival function in ecology (see Section 5.1). This is similar to the findings by [102] for the case where multiple films were confined in tubes.

In Fig. 5.18, we show the failure rate computed for the combined data sets for tubes with only one stopper (cf. Fig 5.14(a)). In the same figure, we also plot the percentages of the films contained in the 3-cm-, 10-cm-, and 20-cm-long tubes, respectively.

The initial sharp rise in the failure rate $\mu(t)$ corresponds to the rupturing of the films contained in the 3-cm-long tubes. These have the shortest lifetimes and have all vanished after about 3 min (c.f. Fig 5.14(a)). As their presence in the combined film population decreases, the failure rate steadily decreases. It only begins to rise again after about 6 min, when the first films in the 10-cm-long tubes begin to rupture. As the rate of these rupturing events slows down at about 12 min, the failure rate is seen to decrease once more. However, there is now increased film rupturing also of films in the 20-cm-long tubes, making this second minimum in the failure rate at about 17 min much shallower than the first one. The failure rate data for the combined data set for tubes with two stoppers (Fig 5.14(b)) is similar, but does not feature the second minimum.

Figure 5.18 thus illustrates what is called the bath-tub curve of failure rate, known for example from data for technical devices as discussed in Section 5.1 and shown in Fig. 5.1. *Defective samples* (in our case represented by films that are confined in short tubes) lead to an initially high failure rate, which begins to decrease once the samples have stopped working (i.e., the corresponding films in the short 3-cm tubes have ruptured). In Fig. 5.18, we also see a second, shallower "bath-tub"; as we have remarked in Section 5.1, information about the defect distribution can be inferred from lifetime data.

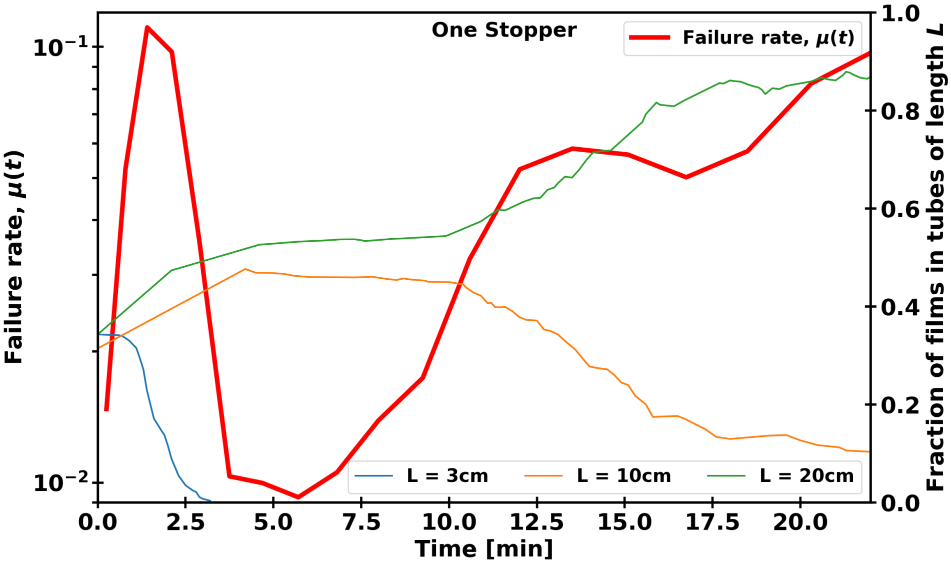

Fig 5.18: Failure rate $\mu(t)$, Eq. 5.4 and fraction of films in tubes of length 3 cm, 10 cm, and 20 cm, as a function of time. $\mu(t)$ was computed from the combined survival functions $S(t)$ for films confined in tubes with one stopper; see Fig. 5.15. The "double bath-tub shape" is due to the different average lifetimes of films contained in tubes of three different lengths. To avoid large fluctuations when computing $\mu(t)$, we only show data for the first 22 min. At this stage, 86% of the initially 320 films have ruptured.

5.7 Conclusions

In summary, in this Chapter, we have investigated the use of soap films as a simple and accessible physical system for studying mortality and failure, which provided a controlled and reproducible environment to study mortality or failure. Our examination of soap film lifetime statistics has yielded valuable insights and showed that individual soap films displayed a common pattern of mortality/failure called the bath-tub curve.

We have introduced the concepts of mortality and failure, including the life table, survival function, mortality rate, and the Gompertz law of mortality in this chapter. Our study has shown how these concepts can be applied to the soap film data as a simple model.

Furthermore, our experiments using soap films not only advanced our scientific knowledge but also provided a tangible and accessible way to demonstrate complex concepts in a classroom setting. The lifetime study carried out here using soap films offers a hands-on approach for students to explore these concepts while demonstrating the application of statistical methods in real-world problems.

Our study utilized Perspex tubes of varying lengths to create individual soap films and examine their mortality and failure. We also presented survival functions and mortality rates for the soap film data, with a focus on early-stage (infant) mortality using the failure mechanism. Our methodology linked the failure rate to the geometry of the system, specifically the length of the tube containing the films.

Our investigation of the relationship between defect size distribution and lifetime distribution is also relevant to the manufacturing of electronic devices. It can be used to determine optimal burn-in parameters, ensuring that the products leaving the factory have long lifetimes.

Finally, we suggest that environmental shocks may impact mortality, and further exploration of this effect using soap films could be illustrative. However, much less is known about the impact of atmospheric pollution, novel medication, and vaping. Meaningful data in these areas may require considerable time to collect, similar to the studies of the effect of smoking on health which took many decades of painstaking effort.

5.8 DIY Science: Hands-on Experiments

5.8.1 Interference colours of soap bubble

The formation of iridescent colors resembling a rainbow results from light interacting with soap bubbles on both surfaces (See Fig. 5.9). The interferences between the reflected light waves lead to an amplification of light, resulting in the emergence of vibrant colors. The hues observed depend on several factors, including the thickness of the soap film, the viewing direction, and the angle of observation. These variables cause the colors to change and create distinct patterns that are often visible in soap bubbles. To see interference colours of soap bubble:

Accessibility	Cost	Duration
★★★	💵	⌛

Materials:

✓A container

✓One litre water

✓Dish soap (Fairy Liquid)

✓A perspex tube

✓White light

✓A camera

To begin, add a few droplets of Fairy Liquid to a container of water and stir the mixture slowly until the dish soap has been fully incorporated.

The experimental procedure involves submerging a tube halfway into a solution-filled container and sealing the top end with a hand or stopper. Once the tube has been removed from the container and the hand/stopper has been taken off, a two-dimensional soap film will emerge within the tube. A white light should then be directed at the soap film to generate the interference colors. The orientation of the tube can be either horizontal or vertical, and this may influence the resulting observations (See Fig. 5.9).

Chapter 6

Summary and Suggestions for Future Research

> ” **Physics is the universe’s operating system.**
>
> — **Steven R Garman**

This thesis described a range of experiments using hard spheres, soap film/bubbles, and hydrogels. The experiments have in common that as well as being of interest in their own right, they also provide illustrations of features found in the areas of physics, such as symmetry breaking, buckling, and failure.

Furthermore, we have provided descriptions of variations of our experiments, of use at both school and undergraduate university levels.

Chapter 1 introduced some examples of using hard/soft spheres and soap bubbles/films to demonstrate science, such as using soap films to visualize the sound waves.

Chapter 2 is dedicated to the behavior of a chain of hard spheres, confined in a transverse harmonic potential, and subject to compression. The resulting phenomenon of buckling is shown to be reproducible from a numerical model.

In Chapter 3 we have extended these buckling experiments to chains of soap bubbles. The key findings carry on, but buckling occurs only for a finite compression due to the deformability of the bubbles.

In the fourth Chapter, we presented various experimental arrangements utilizing hydrogel spheres that illustrate the buckling and dense packing of deformable spheres which can be grown (via water absorption) into different geometric confinement. The configurations closely resemble those found in foams, emulsions, and other related structures. The experiments are straightforward to carry out and provide a valuable addition to the body of research on packing problems, which have yet to be thoroughly explored using this convenient system.

In Chapter 5 we presented experiments using soap films as a simplified physical system to model the complex phenomena of ageing and failure. These experiments provide a controlled and reproducible environment to observe and analyze the process of ageing and failure, which can be difficult to study in real-life materials. The results from examining the lifetime statistics of soap films provide valuable insights into the underlying dynamics of these processes. The findings from these experiments can be applied to the development of new methods for predicting the lifetime of materials, and for designing materials with improved durability and performance.

In the following, we will discuss suggestions for future research in the areas of experiments with hard or soft spheres and shock experiments with soap films.

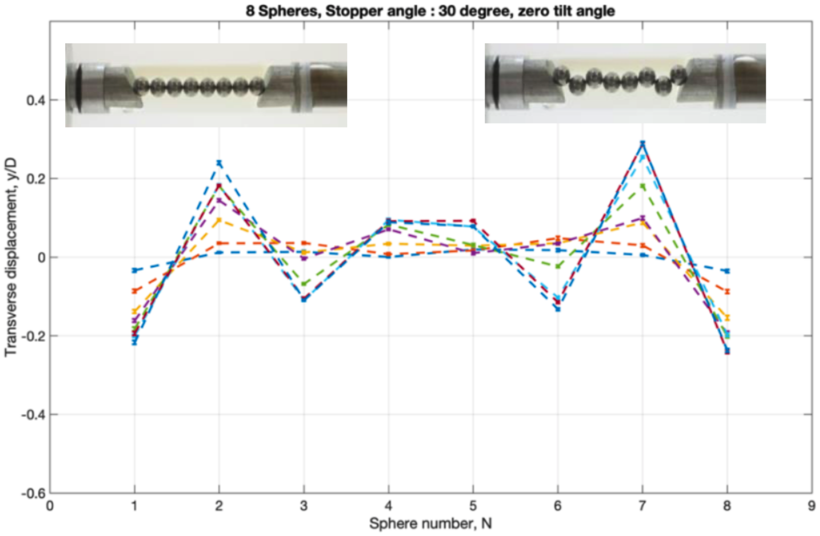

Fig 6.1: Transverse displacement profile of 8 spheres confined in a cylindrical tube with ends closed using two opposite slants stoppers, starting from a linear chain (top left image) and end up with a non-uniform zig-zag structure (top right image).

6.1 Further Experiments with Hard Spheres

Previously, we examined the characteristics of a linear chain of hard or soft spheres that were subject to tilt or compression, and which were confined within a cylindrical tube restricted with *flat* stoppers perpendicular to the tube axis. The use of slanted stoppers, which lead to different boundary conditions at both ends of the chain, results in different buckled structures.

Here, we present limited experimental data that employ these slanted walls. Additional research is required in order to gain a deeper understanding of their characteristics and produce corresponding numerical solutions.

Experimental procedures employing slanted stoppers were conducted with both parallel and opposite slants. Initially, we will present an example utilizing opposite slants and subsequently provide additional data concerning parallel slants. Specifically, a slant angle of 30 degrees was implemented for each stopper.

6.1.1 Experiment 1: N = 8 spheres, compression = 0 to 0.50

Following the arrangement of slant stoppers in an opposing fashion, a series of over twenty experiments were conducted, resulting in a consistent structural pattern being observed in the majority of cases. The result is a double-peak structure as shown in Fig. 6.1, which corresponds to experiments with low compression values.

6.1.2 Experiment 2: N = 8 spheres, compression = 0 to 2.50

A total of approximately 20 experiments were carried out utilizing parallel slant stoppers, resulting in the formation of a doublet structure near the hard walls in approximately 40% of the experiments, while in the remaining cases (roughly 60%), the doublet structure was observed at the center of the chain. Similar experiments should be performed using bubbles, to avoid friction.

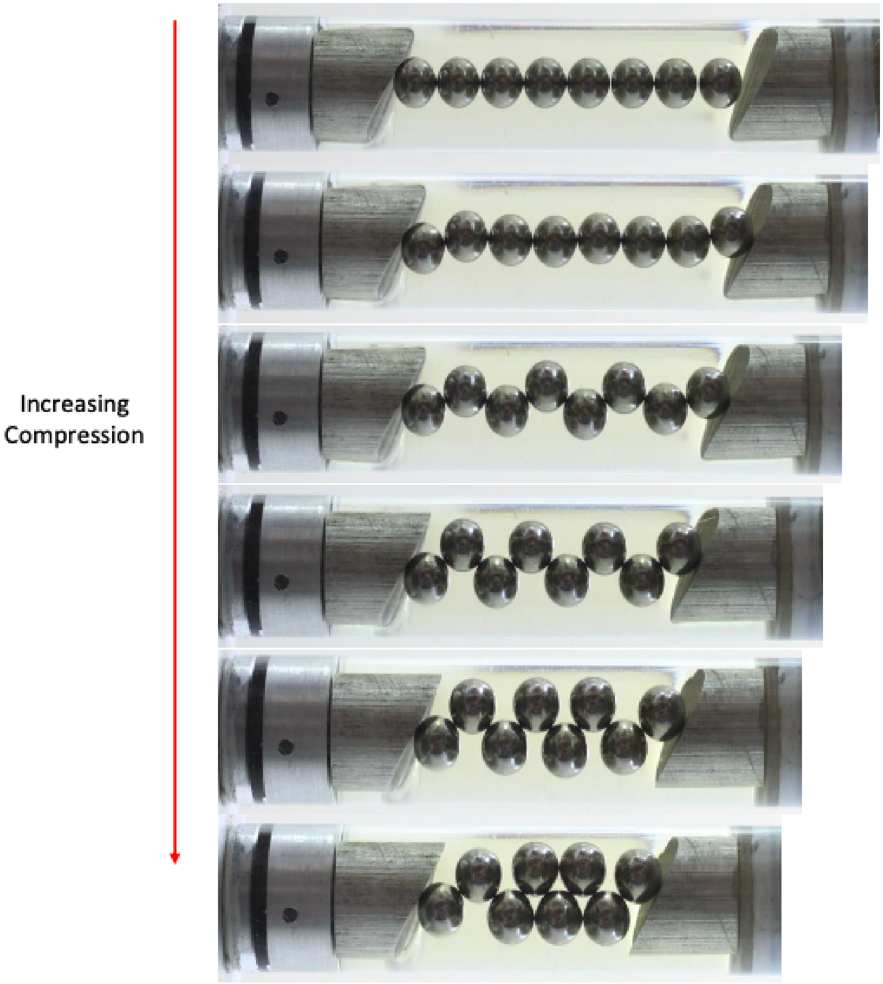

Fig 6.2: Image sequences of a linear chain of 8 spheres under compression which is confined between two parallel slant stoppers. Instead of a localized buckling at high compression, a very nice uniform zigzag structure is observed! Starting from a linear chain, followed by a nice uniform zigzag structure, and ending with a doublet roughly in the middle.

6.2 Shock Experiments with Soap Films

As discussed in chapter 4, environmental shocks might be expected to affect mortality, here is some suggestion for further exploration using soap films that could illustrate this clearly.

Here, three types of experiments with liquid films made from SDS solution (concentration 3 CMC which is high enough to ensure soap film stability) in cylinders were conducted in parallel, to guarantee identical environmental conditions (humidity, temperature, etc.).

In each experiment, one soap film was captured in a perspex cylinder tube of inner diameter 1.6 cm and length 20 cm. The film was placed horizontally in the middle of the vertical cylinder.

Experiment A**:** The cylinder was sealed with two stoppers at the top and bottom ends.

Experiment B**:** The cylinder was sealed with one stopper at the bottom end.

Experiment C**:** The cylinder was sealed with two stoppers for 20 minutes, then the top stopper was removed so there was only the bottom stopper left, as in Exp B.

One experimental run involved taking data for films in 10 tubes of each type, A, B, and C. 25 such runs were conducted, resulting in a dataset for a total of 25 x 10 x 3 x 1 = 750 films.

We determined when an individual film ruptured. We then combined all data for the A, B, and C type experiments. In Fig. 6.3 we plot the survival function for the three types of experiments. This is defined as

$$S(t) = \frac{N(t)}{N(0)} \tag{6.1}$$

where $N(t)$ is the number of films at time t and $N(0) = 250$.

Exp B (one stopper) shows the strongest decay of $S(t)$, with $S_B(t) = 0.2$

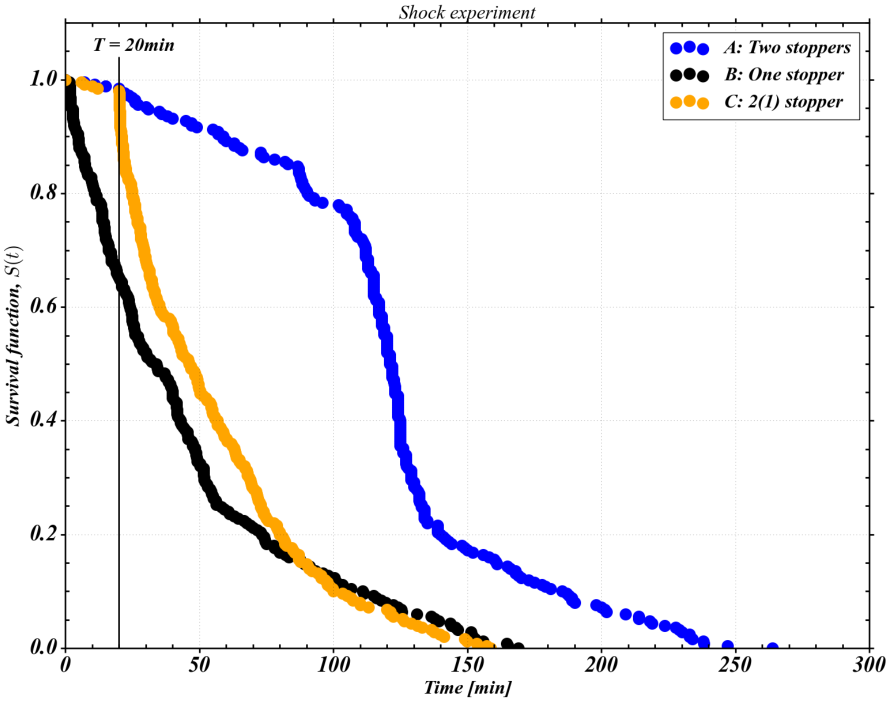

Fig 6.3: Survival function, $S_A(t)$, $S_B(t)$, and $S_C(t)$ for the three types of experiments. A (two stoppers), B (one stopper), and C (two stoppers for 20 mins then one stopper).

after about 75 minutes. In Exp A (two stoppers) the decay is much reduced, with $S_A(t) = 0.2$ after about 140 mins.

The variation of $S(t)$ in Exp C follows that of Exp A for the first 20 minutes, as expected: both experiments are for two-stopper tubes in this time interval. As the second stopper is removed at 20 mins, there is a sharp decay in $S_C(t)$.

The last films rupture at: $t_A^* = 264$ minutes (Expt A), $t_B^* = 169$ minutes (Expt B), $t_C^* = 159$ minutes (Expt C). Average lifetime 121 minutes (Expt A), 45 minutes (Expt B), 55 minutes (Expt C).

We have in the following analysis refrained from computing mortality rates since this requires the computation of numerical derivatives. This would be

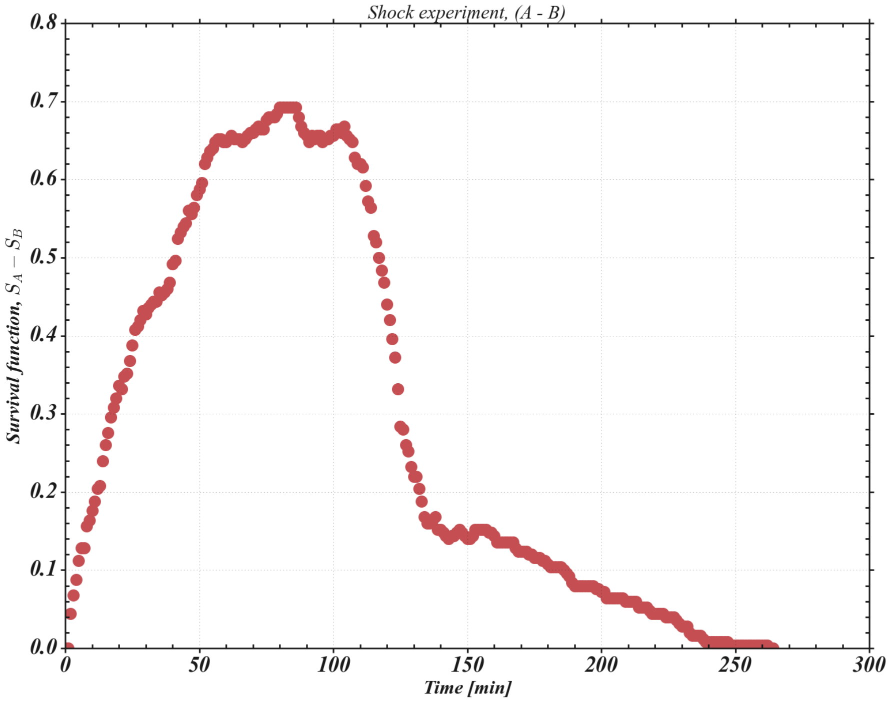

Fig 6.4: Difference in survival function, $S_A(t) - S_B(t)$. The survival function for Exp. A (two stoppers) always exceeds that of Exp. B.

very noisy for our data sets. We thus only compare the differences of $S(t)$ (or $N(t)$) in the following. This only involves the subtraction of data.

At any time we can compute the difference in the number of films in Expt. A compared to Expt. B, $N_{A-B} = N_A(t) - N_B(t)$. This number starts from zero at time $t = 0$, and also its endpoint (the rupture of the last surviving film at $t = t^*_A = 263$ minutes) is given by $N_{A-B}(t^*) = 0$. The maximal difference is reached at about $t_{max} = 70$ minutes.

In Fig. 6.4 we plot the difference in the corresponding survival functions $S_{A-B} = S_A(t) - S_B(t)$ (division by $N = 250$).

In Fig. 6.5 we plot $S_{A-C} = S_A(t) - S_C(t)$. As before this is zero for $t = 0$, however, $S_A(t) - S_C(t)$ remains close to zero (with small fluctuations, always

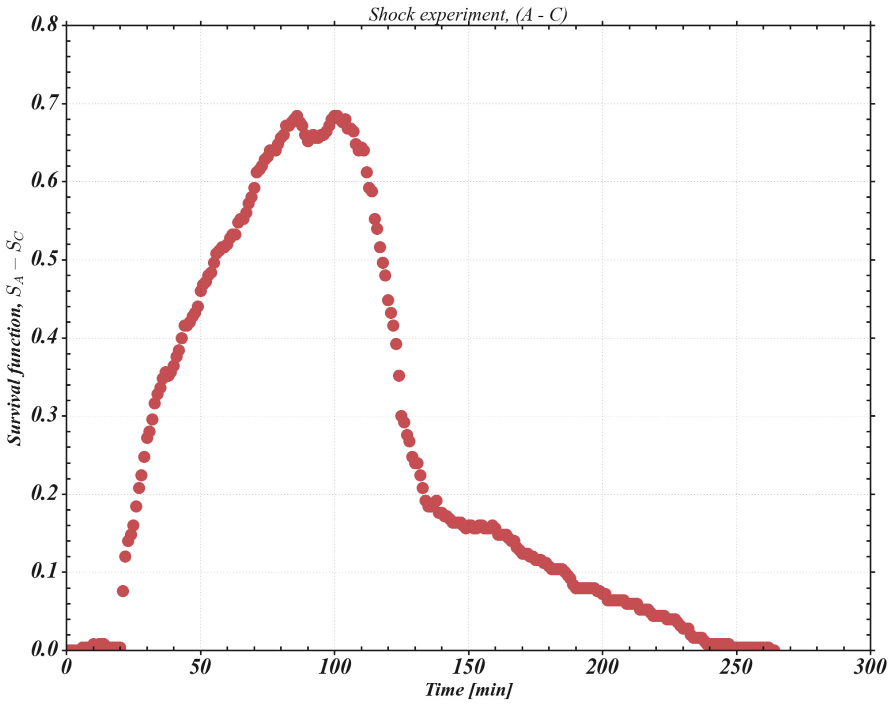

Fig 6.5: Difference in survival function, $S_A(t) - S_C(t)$. The survival function for Exp. A (two stoppers) is essentially identical to the Exp. B for the first 20 mins where both correspond to tubes with two stoppers.

positive in our data) for $t < 20$ $mins$, as in this range both data sets are equivalent (both experiments have two stoppers). A maximum is reached at about 100 minutes. $S_{A-C} = 0$ at $t = t_A^* = 263$ minutes.

In Fig. 6.6 we plot $S_{C-B}(t) = S_C(t) - S_B(t)$. Again $S_{C-B}(0) = 0$, and then increases, up to a maximum after about 20 minutes (when one stopper is removed), when it starts decaying again. However, very oddly after about 90 minutes $S_{C-B}(t)$ takes on negative values and remains negative up to $t_B^* = 169$ minutes when all films have ruptured.

Why is this odd? The films in Expt C spent their first 20 minutes in a double-sealed tube (just like A), and they have thus a more sheltered sur-

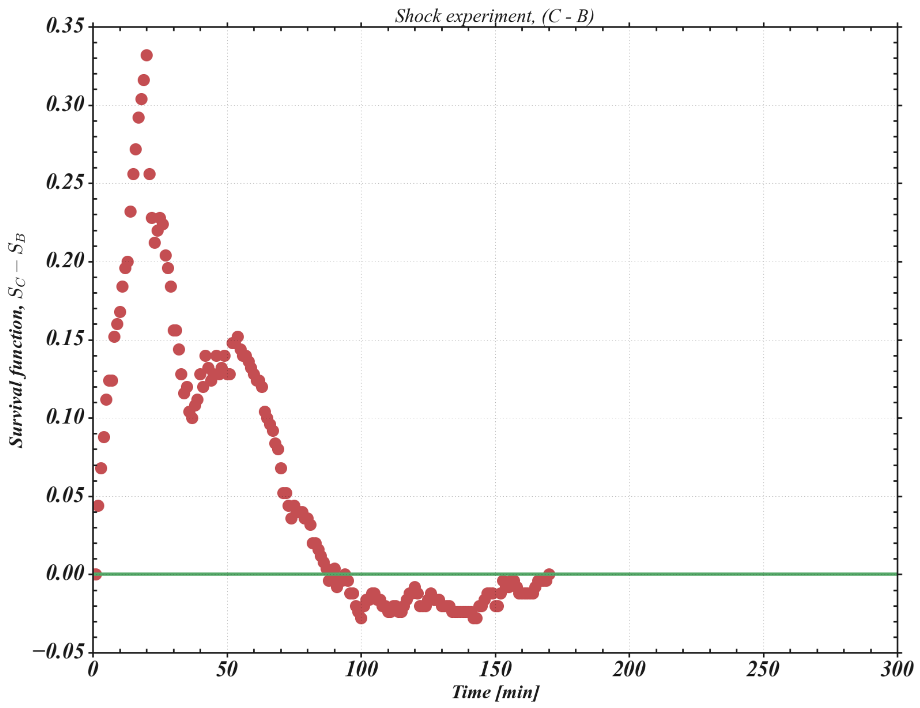

Fig 6.6: Difference in survival function, $S_C(t) - S_B(t)$. Surprisingly the survival function that where initially in the two stoppers tube is smaller than the one with a one-stopper tube after about 90 mins.

rounding than those in Expt B. One might expect that their value of $S_C(t)$ always exceeds that of $S_B(t)$, whose decay had time "to make a head-start".

However, this is not the case. There is a well-defined time interval where $S_B > S_C$. How can this be (if one can rule out any purely statistical fluctuation)?

Could this be the after-effect of a shock that the films experienced as the second stopper was removed after 20 minutes? This would be a shock that only has an effect in the very late life of the films. Is this plausible?

Would there be analogies in human mortality data? Purely speculating here: how do mortality curves look like for people that always lived under poor conditions, compared to those of people who had a sheltered upbringing that stopped after 20 years, leading to poor conditions in the following years. They might not be suited to this life-style?

In terms of shock experiments with soap films, future research could focus on computing mortality rates and investigating the effects of different parameters on the aging and failure of the films. For example, the effect of soap concentration, surfactant type, and film thickness on aging and failure could be studied in more detail.

Another potential avenue for future research is to investigate the effects of external factors on the aging and failure of soap films, such as temperature and humidity. The use of advanced imaging techniques, such as fluorescence microscopy, could be employed to visualize the processes of aging and failure in greater detail.

Overall, further research in the areas of buckling experiments with hard spheres and shock experiments with soap films has the potential to provide valuable insights into the properties and behavior of materials and can lead to the development of new materials with tailored properties for use in a wide range of applications.

Appendix A

A.1 A simple heuristic model for buckling of hard sphere under tilt

In Chapter 2, we discussed the behavior of a line of hard spheres confined in a cylindrical tube under tilt. As already discussed, if one tilts such a system, no instability is found until $\tau \gg \tau_c$. The instability occurs where the local compressive force is largest, i.e. towards the bottom of the chain. To analyze the buckled state, let us consider the second-to-last sphere as the only sphere that can move, resulting in only one variable (f, the displacement of the sphere, or θ, the angle between the line connecting the centers of the second-to-last and the last sphere and the wall). The compressive force on sphere $N-1$ is due to the weight of the chain. At the onset of buckling, the transverse component, which is the sum of the forces due to the contacts with spheres $N-2$ and N $(\tau(N-2)+\tau(N-1))sin\theta)$, overcomes the restoring force ($f = sin\theta$). Using this, the estimate of $\tau > (2N-3)^{-1}$ is obtained for buckling, which provides a rough but reasonably accurate prediction of τ_c.

A modified version of the model permits a simultaneous and equal displacement of both spheres $N-1$ and $N-2$. Such a modification captures the effect of localized buckling more accurately and depicts the behavior of the structure as it approaches the doublet. By considering the equal and opposite displacement of the two spheres, we can more precisely estimate the critical value of the tilt, τ_c, at which the unstable solution vanishes. The model suggests that the tilting of the spheres results from the transverse component of the forces acting on sphere $N-1$. By introducing the modification to the model, we can capture more of the buckling behavior and evaluate the force required to buckle the chain more accurately. As a result, the new model provides a more realistic estimate for τ_c and enhances our understanding of the complex behavior of the chain. This modified version of the model may help us design structures that can better resist the destabilizing effects of compression or buckling.

$$\tau_c = [3(N-2)]^{-1} \tag{A.1}$$

Appendix B

B.1 The Morse–Witten model for deformable spheres

In Chapter 3 we discussed our experiments using one, two, and three-bubble systems. The Morse-Witten model can be used to interpret the data presented in Section 3.3. In the following, we introduce the Morse-Witten model for deformable spheres such as bubbles or droplets.

The Morse-Witten theory illustrates the configuration of a deformed bubble under the influence of a point force and an equivalent counterbalancing body force, such as gravity or buoyancy. Figure B.1 exhibits the three-dimensional (a) and two-dimensional (b) representations of this deformed bubble using the Morse-Witten theory.

Höhler *et al.* reviewed simulations derived from this theory [62]. One potential application of this theory involves characterizing the stable configuration of a solitary bubble that is pushed against a horizontal plate by an external body force (as shown in Fig. B.1(a)). In this scenario, the contact force between the plate and the bubble is considered to be a point force f. To approximate the shape of the bubble, the Morse-Witten theory employs a linearization technique on the interface's curvature C within the Laplace-Young equation

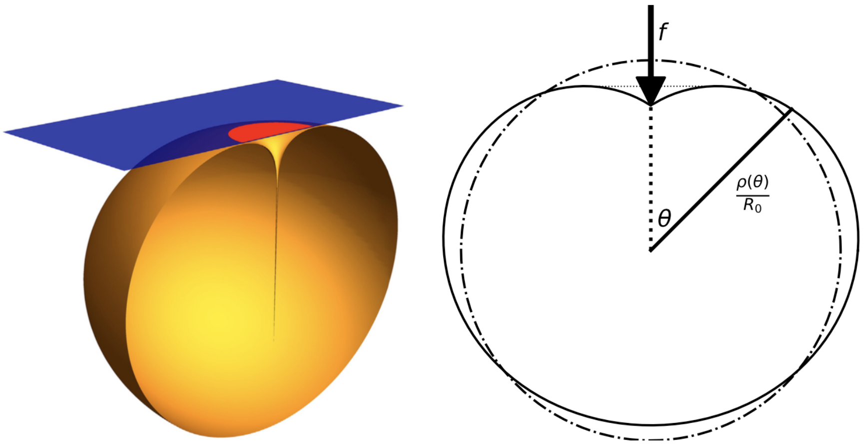

(a) **(b)**

Fig B.1: The Morse-Witten theory is a useful tool for estimating the shape of deformed bubbles in two and three dimensions. (a) demonstrates the shape of a three-dimensional bubble that is pushed against a horizontal plate by buoyancy, with the red disk at the top of the bubble representing the point of contact with the plate. In this case, the yellow region beneath the red disk is negligible and thus is disregarded [62]. (b) depicts the shape of a two-dimensional bubble that is deformed by a point force and an equal compensating body force, which can be calculated using the Morse-Witten theory. The profile of the undeformed bubble, a disk with a radius of R_0, is indicated by a dashed circle, while the portion below the faint horizontal dashed line is not taken into account [132].

$$\gamma C = \Delta p. \tag{B.1}$$

The surface tension of the bubble interface is represented by γ, and the pressure differential across the interface is denoted as Δp. In three dimensions, utilizing this assumption and approximation produces a divergence in the shape at the point of contact (as depicted by the yellow portion below the red disc in Fig. B.1(a)). Nevertheless, because the corrective volume is of second order in the force f, it can be disregarded.

The shape of a two-dimensional bubble can be estimated using a similar approach (as shown in Fig. B.1(b)), with the exception that no divergence arises at $\theta = 0$. The difference between the dashed circle and the bubble's shape in Fig. B.1(b) highlights the impact of deformation on soft spheres like bubbles. The Morse-Witten theory presents a framework for a non-pairwise interaction between bubbles that incorporates deformation.

Appendix C

C.1 Film lifetime data for different experimental set-Ups

We have determined film lifetimes for 16 different experimental set-ups, involving a total of 2916 films. Table C.1. lists the number of stoppers, the film position (horizontal in a vertical tube or vertical in a horizontal tube), tube length and width, the number of experimental runs and the total number of films in these runs. Only the data sets for horizontal films in tubes of 1.6 cm diameter, corresponding to notations $(., H, ., 1.6)$, have been analyzed in this thesis.

(N, O, L, D)	N_r	N_f	T $[min]$	σ $[min]$	C_V
(2, H, 3, 1.6)	12	144	10.4	5.8	0.6
(2, H, 10, 1.6)	12	144	73.3	41.8	0.6
(2, H, 10, 3.4)	12	144	42.1	17.8	0.4
(2, H, 20, 1.6)	12	144	107.7	63.6	0.6
(2, V, 3, 1.6)	12	144	6.97	6.01	0.86
(2, V, 10, 1.6)	12	144	23.3	9.9	0.4
(2, V, 10, 3.4)	12	144	14.2	4	0.3
(2, V, 20, 1.6)	12	144	40.9	15.1	0.4
(1, H, 3, 1.6)	12	144	1.7	0.6	0.3
(1, H, 10, 1.6)	11	132	13.1	4.7	0.4
(1, H, 10, 3.4)	16	192	3.8	1.6	0.4
(1, H, 20, 1.6)	12	144	20.4	8.9	0.4
(1, V, 3, 1.6)	12	144	3.3	0.9	0.3
(1, V, 10, 1.6)	12	144	10.4	3.8	0.4
(1, V, 10, 3.4)	12	144	7.3	1.9	0.3
(1, V, 20, 1.6)	12	144	25.7	10.6	0.4
(0, V, 3, 1.6)	12	144	2.5	0.9	0.4
(0, V, 10, 1.6)	12	144	8.5	2.5	0.3
(0, V, 10, 3.4)	12	144	5.1	1.5	0.3
(0, V, 20, 1.6)	12	144	22.7	10.3	0.5

Table C.1: Summary of all experimental data: N lists the number of stoppers, O the film orientation in the tube (H for horizontally placed films in vertical tubes, and V for vertically placed films in horizontal tubes), L and D are tube length and inner tube diameter, respectively (both measured in centimetres). N_r is the number of experimental runs for a particular set-up, and N_f is the total number of soap films involved. T is the average soap film lifetime and σ is the standard deviation (both measured in minutes). C_V is the coefficient of variation. (Note that horizontal films require at least one stopper to be held in place.)

C.2 Histogram of Film Lifetime Experiments

Histograms of the life-time distributions for some of experiments are shown in C.1.

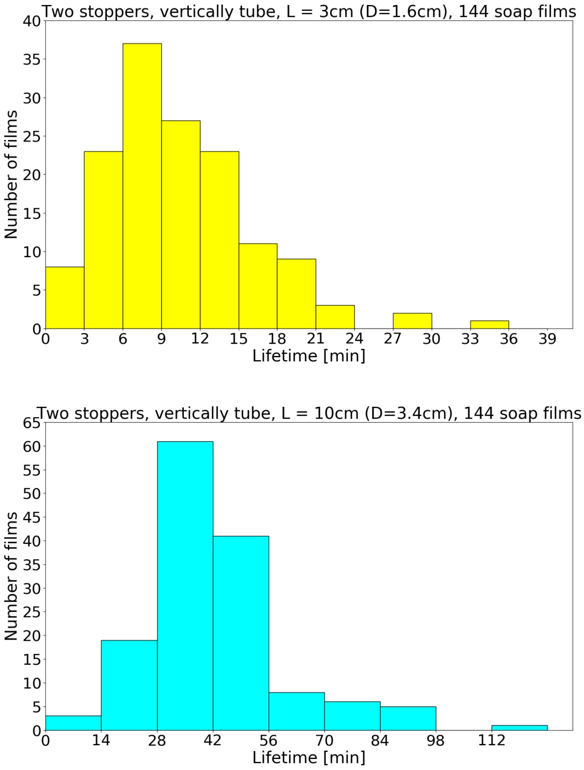

Two stoppers, vertically tube, L = 3cm (D=1.6cm), 144 soap films

Two stoppers, vertically tube, L = 10cm (D=3.4cm), 144 soap films

Fig C.1: Histograms for vertical tube experiments, both ends sealed.

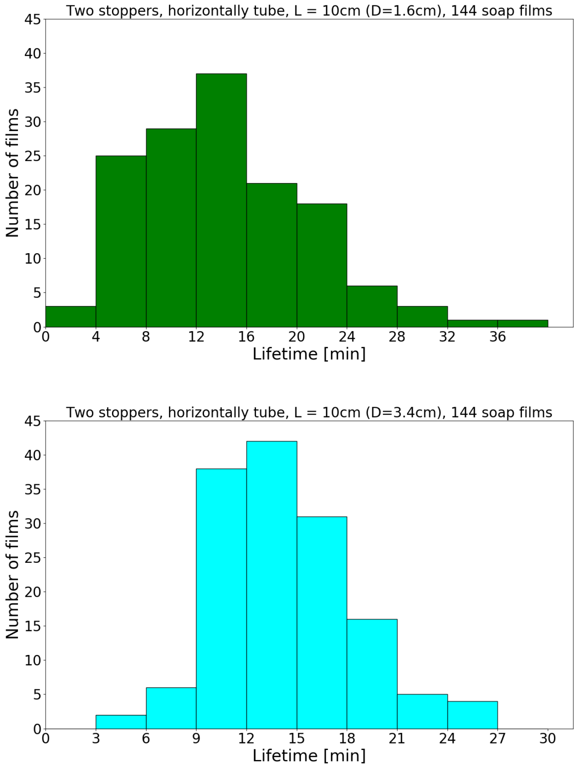

Fig C.2: Histograms for horizontal tube experiments, both ends sealed.

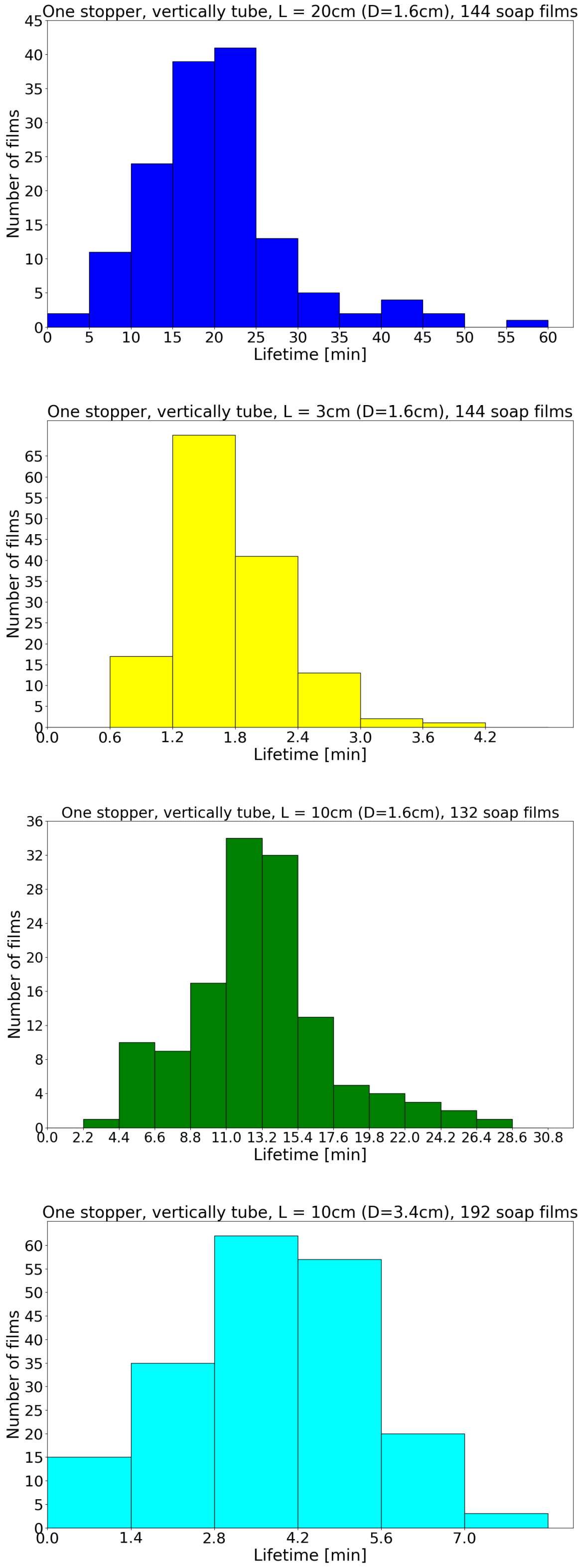

Fig C.3: Histograms for vertical tube experiments, one end sealed.

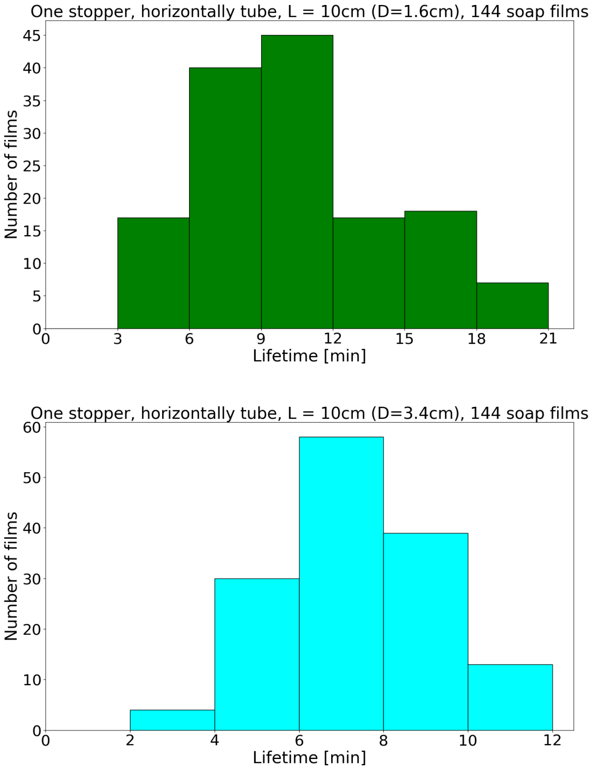

Fig C.4: Histograms for horizontal tube experiments, one end sealed.

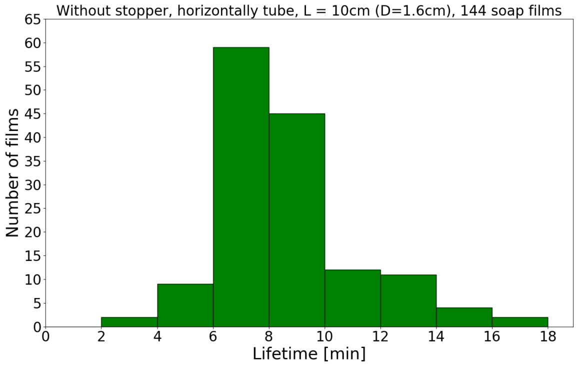

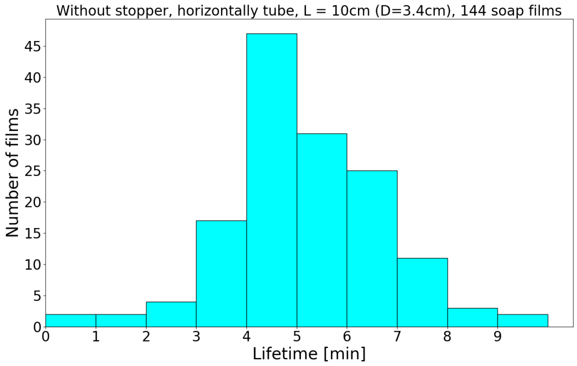

Fig C.5: Histograms for horizontal tube experiments, open tubes.

Bibliography

[1] D. Weaire, A. Irannezhad, A. Mughal, and S. Hutzler, *A simple experimental system to illustrate the nonlinear properties of a linear chain under compression*, American Journal of Physics **88**, 347–352 (2020).

[2] A. Bois, E. M. Garcıa-Roger, E. Hong, S. Hutzler, A. Irannezhad, A. Mannioui, P. Richmond, B. M. Roehner, and S. Tronche, *Physical models of infant mortality: implications for defects in biological systems*, Journal of Biological Physics **46**, 371–394 (2020).

[3] S. Hutzler, A. Mughal, J. Ryan-Purcell, A. Irannezhad, and D. Weaire, *Buckling of a linear chain of hard spheres in a harmonic confining potential: numerical and analytical results for low and high compression*, Physical Review E **102**, 022905 (2020).

[4] P. Richmond, B. M. Roehner, A. Irannezhad, and S. Hutzler, *Mortality: a physics perspective*, Physica A: Statistical Mechanics and its Applications **566**, 125660 (2021).

[5] D. Weaire, S. Hutzler, A. Irannezhad, and K. Cox, “Physics in a small bedroom”, in *Imagine math 8*, edited by M. Emmer and M. Abate (Springer, 2022), pp. 333–343.

[6] A. Irannezhad, D. Weaire, A. Mughal, J. Ryan-Purcell, and S. Hutzler, *Buckling of a tilted line of confined hard spheres*, Philosophical Magazine **102**, 2506–2524 (2022).

[7] A. Irannezhad, A. Baragry, D. Weaire, A. Mughal, and S. Hutzler, *Packing soft spheres: experimental demonstrations with hydrogels*, (Submitted) (2023).

[8] A. Rogava, *Tennis-ball towers*, Physics World **32**, 25–25 (2019).

[9] C. Vafa, *Puzzles to unravel the universe* (Amazon Italy, 2020).

[10] P. M. Chaikin, T. C. Lubensky, and T. A. Witten, *Principles of condensed matter physics*, Vol. 10 (Cambridge university press Cambridge, 1995).

[11] A. Mughal, D. Weaire, and S. Hutzler, *Peierls-Nabarro potential for a confined chain of hard spheres under compression*, EPL (Europhysics Letters) **135**, 26002 (2021).

[12] R. S. Westfall, *The Life of Isaac Newton* (Cambridge University Press, 1994).

[13] E. Hinch and S. Saint–Jean, *The fragmentation of a line of balls by an impact*, Proceedings of the Royal Society of London. Series A: Mathematical, Physical and Engineering Sciences **455**, 3201–3220 (1999).

[14] S. Hutzler, G. Delaney, D. Weaire, and F. MacLeod, *Rocking Newton's cradle*, American Journal of Physics **72**, 1508–1516 (2004).

[15] R. Cross, *The effect of very small ball gaps in newton's cradle*, European Journal of Physics **42**, 025004 (2021).

[16] M. Emmer, *Bolle di sapone: tra arte e matematica* (Bollati Boringhieri, 2009).

[17] C. Isenberg, *The science of soap films and soap bubbles* (Courier Dover Publications, 1992).

[18] D. Weaire and T. Aste, *The pursuit of perfect packing* (CRC Press, 2008).

[19] M. Doi, *Soft matter physics* (oxford university press, 2013).

[20] G. Rämme, *Soap bubbles in art and education* (Science Culture Technology Publishing, Singapore, 1998).

[21] T. Meuel, Y. L. Xiong, P. Fischer, C.-H. Bruneau, M. Bessafi, and H. Kellay, *Intensity of vortices: from soap bubbles to hurricanes*, Scientific reports **3**, 3455 (2013).

[22] P. Ball, *Beijing bubbles*, Nature **448**, 256–256 (2007).

[23] D. Weaire and R. Phelan, *A counter-example to Kelvin's conjecture on minimal surfaces*, Philosophical Magazine Letters **69**, 107–110 (1994).

[24] P. Gómez-Gálvez, P. Vicente-Munuera, A. Tagua, C. Forja, A. M. Castro, M. Letrán, A. Valencia-Expósito, C. Grima, M. Bermúdez-Gallardo, Ó. Serrano-Pérez-Higueras, et al., *Scutoids are a geometrical solution to three-dimensional packing of epithelia*, Nature communications **9**, 1–14 (2018).

[25] A. Mughal, S. Cox, D. Weaire, S. Burke, and S. Hutzler, *Demonstration and interpretation of "scutoid" cells formed in a quasi-2d soap froth*, Philosophical Magazine Letters **98**, 358–364 (2018).

[26] F. Elias, S. Hutzler, and M. Ferreira, *Visualization of sound waves using regularly spaced soap films*, European journal of physics **28**, 755 (2007).

[27] P. Tecilla, R. P. Dixon, G. Slobodkin, D. S. Alavi, D. H. Waldeck, and A. D. Hamilton, *Hydrogen-bonding self-assembly of multichromophore structures*, Journal of the American Chemical Society **112**, 9408–9410 (1990).

[28] C. C. Ng, Y.-L. Cheng, and P. S. Pennefather, *Properties of a self-assembled phospholipid membrane supported on lipobeads*, Biophysical Journal **87**, 323–331 (2004).

[29] L. Nasalean, S. Baudrey, N. B. Leontis, and L. Jaeger, *Controlling rna self-assembly to form filaments*, Nucleic acids research **34**, 1381–1392 (2006).

[30] J. Won, S. K. Chae, J. H. Kim, H. H. Park, Y. S. Kang, and H. S. Kim, *Self-assembled dna composite membranes*, Journal of membrane science **249**, 113–117 (2005).

[31] R. Soto and R. Golestanian, *Self-assembly of catalytically active colloidal molecules: tailoring activity through surface chemistry*, Physical review letters **112**, 068301 (2014).

[32] K. Yasuda, R. Okamoto, and S. Komura, *A three-sphere microswimmer in a structured fluid*, EPL (Europhysics Letters) **123**, 34002 (2018).

[33] E. Britannica et al., *Encyclopædia britannica*, 1993.

[34] A.-I. Bunea and R. Taboryski, *Recent advances in microswimmers for biomedical applications*, Micromachines **11**, 1048 (2020).

[35] S. De Oliveira, E. E. Rosowski, and A. Huttenlocher, *Neutrophil migration in infection and wound repair: going forward in reverse*, Nature Reviews Immunology **16**, 378–391 (2016).

[36] E. Lauga, T. N. Dang, and T. Ishikawa, *Zigzag instability of biased pusher swimmers*, Europhysics Letters **133**, 44002 (2021).

[37] Y. Ding and F. T. Chong, *Quantum computer systems: research for noisy intermediate-scale quantum computers*, Synthesis Lectures on Computer Architecture **15**, 1–227 (2020).

[38] J. I. Cirac and P. Zoller, *Quantum computations with cold trapped ions*, Physical review letters **74**, 4091 (1995).

[39] P. W. Shor, “Algorithms for quantum computation: discrete logarithms and factoring”, in Proceedings 35th annual symposium on foundations of computer science (Ieee, 1994), pp. 124–134.

[40] E. Shimshoni, G. Morigi, and S. Fishman, *Quantum zigzag transition in ion chains*, Physical review letters **106**, 010401 (2011).

[41] L. Yan, W. Wan, L. Chen, F. Zhou, S. Gong, X. Tong, and M. Feng, *Exploring structural phase transitions of ion crystals*, Scientific reports **6**, 21547 (2016).

[42] J. Winkelmann, A. Mughal, D. Weaire, and S. Hutzler, *Equilibrium configurations of hard spheres in a cylindrical harmonic potential*, Europhysics Letters **127**, 44002 (2019).

[43] T. Lee, K. Gizynski, and B. A. Grzybowski, *Non-equilibrium self-assembly of monocomponent and multicomponent tubular structures in rotating fluids*, Advanced Materials **29**, 1704274 (2017).

[44] A. Rogava, *Tennis-ball towers*, Physics World **32**, 25 (2019).

[45] M. Calkin and R. March, *The dynamics of a falling chain: i*, American Journal of Physics **57**, 154–157 (1989).

[46] E. Hamm and J.-C. Géminard, *The weight of a falling chain, revisited*, American Journal of Physics **78**, 828–833 (2010).

[47] J.-C. Géminard and L. Vanel, *The motion of a freely falling chain tip: force measurements*, American Journal of Physics **76**, 541–545 (2008).

[48] F. Herrmann and M. Seitz, *How does the ball-chain work?*, American Journal of Physics **50**, 977–981 (1982).

[49] P. Gnädig, G. Honyek, and K. F. Riley, *200 puzzling physics problems: with hints and solutions* (Cambridge University Press, 2001).

[50] J. D. Louck, *Exact normal modes of oscillation of a linear chain of identical particles*, American Journal of Physics **30**, 585–590 (1962).

[51] M. Reinsch, *Dispersion-free linear chains*, American Journal of Physics **62**, 271–278 (1994).

[52] H. Landa, B. Reznik, J. Brox, M. Mielenz, and T. Schätz, *Structure, dynamics and bifurcations of discrete solitons in trapped ion crystals*, New Journal of Physics **15**, 093003 (2013).

[53] M. Mielenz, J. Brox, S. Kahra, G. Leschhorn, M. Albert, T. Schätz, H. Landa, and B. Reznik, *Trapping of topological-structural defects in coulomb crystals*, Physical review letters **110**, 133004 (2013).

[54] R. K. Pal, F. Bonetto, L. Dieci, and M. Ruzzene, *A study of deformation localization in nonlinear elastic square lattices under compression*, Philosophical Transactions of the Royal Society A: Mathematical, Physical and Engineering Sciences **376**, 20170140 (2018).

[55] S. Gonzalez and R. Soto, *Active colloidal chains with cilia-and flagella-like motion*, New Journal of Physics **20**, 053014 (2018).

[56] B. R. Heazlewood, *Cold ion chemistry within coulomb crystals*, Molecular Physics **117**, 1934–1941 (2019).

[57] D. J. Durian, *Foam mechanics at the bubble scale*, Physical Review Letters **75**, 4780 (1995).

[58] D. J. Durian, *Bubble-scale model of foam mechanics: mmelting, nonlinear behavior, and avalanches*, Physical Review E **55**, 1739 (1997).

[59] D. Weaire and S. Hutzler, *The Physics of Foams: Oxford University Press*, New York (1999).

[60] I. Cantat, S. Cohen-Addad, F. Elias, F. Graner, R. Höhler, O. Pitois, F. Rouyer, and A. Saint-Jalmes, *Foams: structure and dynamics* (OUP Oxford, 2013).

[61] D. Morse and T. Witten, *Droplet elasticity in weakly compressed emulsions*, Europhysics Letters **22**, 549 (1993).

[62] R. Höhler and D. Weaire, *Can liquid foams and emulsions be modeled as packings of soft elastic particles?*, Advances in colloid and interface science **263**, 19–37 (2019).

[63] O. Wichterle and D. Lim, *Hydrophilic gels for biological use*, Nature **185**, 117–118 (1960).

[64] R. Orbach, L. Adler-Abramovich, S. Zigerson, I. Mironi-Harpaz, D. Seliktar, and E. Gazit, *Self-assembled fmoc-peptides as a platform for the formation of nanostructures and hydrogels*, Biomacromolecules **10**, 2646–2651 (2009).

[65] E. Caló and V. V. Khutoryanskiy, *Biomedical applications of hydrogels: a review of patents and commercial products*, European Polymer Journal **65**, 252–267 (2015).

[66] M. Bahram, N. Mohseni, and M. Moghtader, "An introduction to hydrogels and some recent applications", in *Emerging concepts in analysis and applications of hydrogels* (IntechOpen, 2016).

[67] F. Ullah, M. B. H. Othman, F. Javed, Z. Ahmad, and H. M. Akil, *Classification, processing and application of hydrogels: a review*, Materials Science and Engineering: C **57**, 414–433 (2015).

[68] T. Bertrand, J. Peixinho, S. Mukhopadhyay, and C. W. MacMinn, *Dynamics of swelling and drying in a spherical gel*, Physical Review Applied **6**, 064010 (2016).

[69] W. E. Hennink and C. F. van Nostrum, *Novel crosslinking methods to design hydrogels*, Advanced drug delivery reviews **64**, 223–236 (2012).

[70] H. H. Hooper, J. P. Baker, H. W. Blanch, and J. M. Prausnitz, *Swelling equilibria for positively ionized polyacrylamide hydrogels*, Macromolecules **23**, 1096–1104 (1990).

[71] S. Koosehgol, M. Ebrahimian-Hosseinabadi, M. Alizadeh, and A. Zamanian, *Preparation and characterization of in situ chitosan/polyethylene glycol fumarate/thymol hydrogel as an effective wound dressing*, Materials Science and Engineering: C **79**, 66–75 (2017).

[72] D. Weaire, A. Mughal, J. Ryan-Purcell, and S. Hutzler, *Description of the buckling of a chain of hard spheres in terms of jacobi functions*, Physica D: Nonlinear Phenomena **433**, 133177 (2022).

[73] J. Kepler, *The Six-Cornered Snowflake, edited by Colin Hardie* (The Clarendon Press, Oxford, 1966).

[74] D. Weaire, *A short history of packing problems*, FORMA-TOKYO- **14**, 279–285 (1999).

[75] T. C. Hales, *An overview of the Kepler conjecture*, arXiv preprint math/9811071 (1998).

[76] S. Hales, *Vegetable staticks: or, an account of some statical experiments on the sap in vegetables: being an essay towards a natural history of vegetation. also, a specimen of an attempt to analyse the air, by a great variety of chymio-statical experiments; which were read at several meetings before the royal society....* Vol. 1 (W. and J. Innys, at the West End of St. Paul's, 1727).

[77] J. Wisniak, *Stephen Hales*, Revista CENIC Ciencias Biológicas **43** (2012).

[78] D. W. Thompson, *On growth and form*, Vol. 2 volumes (Cambridge University Press, 1942).

[79] W. Thomson, *Lxiii. on the division of space with minimum partitional area*, The London, Edinburgh, and Dublin Philosophical Magazine and Journal of Science **24**, 503–514 (1887).

[80] D. Weaire, ed., *The Kelvin Problem* (Taylor & Francis, 1996).

[81] J. D. Bernal, *A geometrical approach to the structure of liquids*, Nature **183**, 141–147 (1959).

[82] A. Donev, I. Cisse, D. Sachs, E. A. Variano, F. H. Stillinger, R. Connelly, S. Torquato, and P. M. Chaikin, *Improving the density of jammed disordered packings using ellipsoids*, Science **303**, 990–993 (2004).

[83] G. Delaney, D. Weaire, S. Hutzler, and S. Murphy, *Random packing of elliptical disks*, Philosophical Magazine Letters **85**, 89–96 (2005).

[84] A. Mughal, H. Chan, D. Weaire, and S. Hutzler, *Dense packings of spheres in cylinders: simulations*, Physical Review E **85**, 051305 (2012).

[85] S. Williams and A. Philipse, *Random packings of spheres and spherocylinders simulated by mechanical contraction*, Physical Review E **67**, 051301 (2003).

[86] G. W. Delaney and P. W. Cleary, *The packing properties of superellipsoids*, EPL (Europhysics Letters) **89**, 34002 (2010).

[87] T. Aste, M. Saadatfar, and T. J. Senden, *Geometrical structure of disordered sphere packings*, Phys. Rev. E **71**, 061302 (2005).

[88] G. W. Delaney, T. Di Matteo, and T. Aste, *Combining tomographic imaging and dem simulations to investigate the structure of experimental sphere packings*, Soft Matter **6**, 2992–3006 (2010).

[89] F. M. Schaller, M. Neudecker, M. Saadatfar, G. Delaney, K. Mecke, G. E. Schröder-Turk, and M. Schröter, “Tomographic analysis of jammed ellipsoid packings”, in Aip conference proceedings, Vol. 1542, 1 (American Institute of Physics, 2013), pp. 377–380.

[90] A. Meagher, F. Garcıa-Moreno, J. Banhart, A. Mughal, and S. Hutzler, *An experimental study of columnar crystals using monodisperse microbubbles*, Colloids and Surfaces A: Physicochemical and Engineering Aspects **473**, 55–59 (2015).

[91] A. J. Meagher, D. Whyte, J. Banhart, S. Hutzler, D. Weaire, and F. Garcıa-Moreno, *Slow crystallisation of a monodisperse foam stabilised against coarsening*, Soft Matter **11**, 4710–4716 (2015).

[92] T. Bertrand, J. Peixinho, S. Mukhopadhyay, and C. W. MacMinn, *Dynamics of swelling and drying in a spherical gel*, Physical Review Applied **6**, 064010 (2016).

[93] W. L. Bragg and J. F. Nye, *A dynamical model of a crystal structure*, Proceedings of the Royal Society of London. Series A. Mathematical and Physical Sciences **190**, 474–481 (1947).

[94] E. Specht, *Packomania, 2022*, URL: http://www.packomania.com.

[95] G. T. Pickett, M. Gross, and H. Okuyama, *Spontaneous chirality in simple systems*, Physical Review Letters **85**, 3652 (2000).

[96] L. Fu, W. Steinhardt, H. Zhao, J. E. Socolar, and P. Charbonneau, *Hard sphere packings within cylinders*, Soft Matter **12**, 2505–2514 (2016).

[97] R. V. Jean, *Phyllotaxis: a systemic study in plant morphogenesis*, Vol. 574 (Cambridge University Press Cambridge, 1994).

[98] A. Waters, F. Blanchette, and A. D. Kim, *Modeling huddling penguins*, PLoS one **7**, e50277 (2012).

[99] A. Mughal, J. Winkelmann, D. Weaire, and S. Hutzler, *Columnar structures of soft spheres: metastability and hysteresis*, Physical Review E **98**, 043303 (2018).

[100] S. Tobin, J. Barry, A. Meagher, B. Bulfin, C. O'Rathaille, and S. Hutzler, *Ordered polyhedral foams in tubes with circular, triangular and square cross-section*, Colloids and Surfaces A: Physicochemical and Engineering Aspects **382**, 24–31 (2011).

[101] S. Tobin, A. Meagher, B. Bulfin, M. Möbius, and S. Hutzler, *A public study of the lifetime distribution of soap films*, American Journal of Physics **79**, 819–824 (2011).

[102] B. Haffner, J. Lalieu, P. Richmond, and S. Hutzler, *Can soap films be used as models for mortality studies?*, Physica A: Statistical Mechanics and its Applications **508**, 461–470 (2018).

[103] L. A. Gavrilov and N. S. Gavrilova, *A quantitative approach*, The Biology of Life Span. Harwood Academic, New York (1991).

[104] I. Bazovsky, *Reliability theory and practice* (Courier Corporation, 2004).

[105] D. KECECIOGLU, *Reliability and life testing handbook volume*,

[106] G.-A. Klutke, P. C. Kiessler, and M. A. Wortman, *A critical look at the bathtub curve*, IEEE Transactions on reliability **52**, 125–129 (2003).

[107] L. A. Gavrilov and N. S. Gavrilova, *Reliability theory of aging and longevity*, Handbook of the Biology of Aging, 3–42 (2005).

[108] J. Graunt, *Natural and political observations made upon the bills of mortality*, 2 (Johns Hopkins Press, 1939).

[109] S. Hin, *The demography of roman italy: population dynamics in an ancient conquest society 201 bce–14 ce* (Cambridge University Press, 2013).

[110] S. Nee, *Survival and weak chaos*, Royal Society open science **5**, 172181 (2018).

[111] L. Hayflick, *Biological aging is no longer an unsolved problem*, Annals of the New York academy of Sciences **1100**, 1–13 (2007).

[112] B. Gompertz, *Xxiv. on the nature of the function expressive of the law of human mortality, and on a new mode of determining the value of life contingencies. in a letter to francis baily, esq. frs &c*, Philosophical transactions of the Royal Society of London, 513–583 (1825).

[113] B. Strihler, *Times, cells, and aging* (Elsevier, 2012).

[114] R. E. Ricklefs and A. Scheuerlein, *Biological implications of the weibull and gompertz models of aging*, The Journals of Gerontology Series A: Biological Sciences and Medical Sciences **57**, B69–B76 (2002).

[115] P. Richmond and B. M. Roehner, *Predictive implications of gompertz's law*, Physica A: Statistical Mechanics and its Applications **447**, 446–454 (2016).

[116] J. G. Ruby, M. Smith, and R. Buffenstein, *Naked mole-rat mortality rates defy gompertzian laws by not increasing with age*, elife **7**, e31157 (2018).

[117] S. Berrut, V. Pouillard, P. Richmond, and B. M. Roehner, *Deciphering infant mortality*, Physica A: Statistical Mechanics and its Applications **463**, 400–426 (2016).

[118] F. E. Linder and R. Grove, *Vital statistics rates in the united states*, Washington, DC (1947).

[119] F. E. Linder and R. D. Grove, *Vital statistics rates in the united states, 1900-1940* (US Government Printing Office, 1943).

[120] H. Wang, A. A. Abajobir, K. H. Abate, C. Abbafati, K. M. Abbas, F. Abd-Allah, S. F. Abera, H. N. Abraha, L. J. Abu-Raddad, N. M. Abu-Rmeileh, et al., *Global, regional, and national under-5 mortality, adult mortality, age-specific mortality, and life expectancy, 1970–2016: a systematic analysis for the global burden of disease study 2016*, The Lancet **390**, 1084–1150 (2017).

[121] R. J. Pugh, *Bubble and foam chemistry* (Cambridge University Press, 2016).

[122] J. Miguet, F. Rouyer, and E. Rio, *The life of a surface bubble*, Molecules **26**, 1317 (2021).

[123] E. Rio and A.-L. Biance, *Thermodynamic and mechanical timescales involved in foam film rupture and liquid foam coalescence*, ChemPhysChem **15**, 3692–3707 (2014).

[124] C. A. Hamlett, D. N. Boniface, A. Salonen, E. Rio, C. Perkins, A. Clark, S. Nyugen, and D. J. Fairhurst, *Blowing big bubbles*, Soft Matter **17**, 2404–2409 (2021).

[125] D. Langevin, *On the rupture of thin films made from aqueous surfactant solutions*, Advances in Colloid and Interface Science **275**, 102075 (2020).

[126] L. Champougny, J. Miguet, R. Henaff, F. Restagno, F. Boulogne, and E. Rio, *Influence of evaporation on soap film rupture*, Langmuir **34**, 3221–3227 (2018).

[127] S. Mariot, M. Pasquet, V. Klein, F. Restagno, and E. Rio, *A new setup for giant soap films characterization*, The European Physical Journal E **44**, 1–8 (2021).

[128] J. Miguet, M. Pasquet, F. Rouyer, Y. Fang, and E. Rio, *Stability of big surface bubbles: impact of evaporation and bubble size*, Soft Matter **16**, 1082–1090 (2020).

[129] G. Ginot, R. Höhler, S. Mariot, A. Kraynik, and W. Drenckhan, *Juggling bubbles in square capillaries: an experimental proof of non-pairwise bubble interactions*, Soft Matter **15**, 4570–4582 (2019).

[130] L. Champougny, M. Roché, W. Drenckhan, and E. Rio, *Life and death of not so "bare" bubbles*, Soft Matter **12**, 5276–5284 (2016).

[131] D. Kumar and B. Klefsjö, *Proportional hazards model: a review*, Reliability Engineering & System Safety **44**, 177–188 (1994).

[132] F. F. Dunne, J. Winkelmann, D. Weaire, and S. Hutzler, *Implementation of morse–witten theory for a polydisperse wet 2d foam simulation*, Philosophical Magazine (2019).